UC San Diego
UC San Diego Electronic Theses and Dissertations

Title

Synthesis and Densification of Nanocrystalline Al2O3 and AlN Ceramics with Improved Optical Transparency for Thermally Robust Photonic Applications

Permalink

https://escholarship.org/uc/item/0zm2w52c

Author

Wu, Xingzhong

Publication Date

2022

Peer reviewed|Thesis/dissertation

eScholarship.org
Powered by the California Digital Library
University of California

UNIVERSITY OF CALIFORNIA SAN DIEGO

Synthesis and Densification of Nanocrystalline Al_2O_3 and AlN Ceramics with Improved Optical Transparency for Thermally Robust Photonic Applications

A Dissertation submitted in partial satisfaction of the requirements
for the degree
Doctor of Philosophy

in

Material Science and Engineering

by

Xingzhong Wu

Committee in charge:

Professor Javier E. Garay, Chair
Professor Prabhakar Bandaru
Professor Farhat Beg
Professor Yasuhiro Kodera
Professor Jian Luo
Professor Vitali Nesterenko

2022

Copyright

Xingzhong Wu, 2022

All rights reserved

The Dissertation of Xingzhong Wu is approved, and it is acceptable in quality and form for publication on microfilm and electronically.

University of California San Diego

2022

DEDICATION

This work is dedicated to Sunan and my parents. To Sunan, thank you for being by my side for the last nine years! I could not get here without your companionship and support. To my parents, thank you for providing me with the best and making this possible.

This work is also dedicated to those who have helped me so much along this journey. Thank you to my grad school lab mates and colleagues Andy Zhao, Darren Dewitt, Meir Shachar, Matthew Duarte, Gottlieb Uahengo, Kyle Chan, Chad Warren, Wenbo Zhou, Ross Turner, Everbrook Zhou, Rashi Jagannatha, Otis Statham, AMPers, Keisuke Matsushita, Audrey Hogan, Isaac Cabrera. It is a pleasure to work with you and benefit from your talent, passion, and inspiration over these years.

Finally, to my advisors and mentors, Dr. Javier Garay and Dr. Yasuhiro Kodera, thank you for your knowledge, experience and guidance. I am so grateful for this opportunity to explore and this vibrant lab environment you provided.

EPIGRAPH

“*When you are studying any matter, or considering any philosophy, ask yourself only: what are the facts, and what is the truth that the facts bear out. Never let yourself be diverted either by what you wish to believe, or by what you think would have beneficent social effects if it were believed. But look only, and solely, at what are the facts.*”

— Bertrand Russell

TABLE OF CONTENTS

LIST OF FIGURES

LIST OF TABLES

ACKNOWLEDGEMENTS

I would like to acknowledge the inspiring discussion that I have benefited from with my AMPS lab colleagues. The invaluable contributions and guidance from Dr. Javier Garay and Dr. Yasuhiro Kodera made these works possible.

Chapter 1, in part, is co-authored with L. Tang, Dr. C. L. Hardin, Dr. C. Dames, Dr. Y. Kodera and Dr. J. E. Garay, and is published in Journal of Applied Physics 2022, 131, 020902. The dissertation author was the primary investigator and author of this paper.

Chapter 2, in full, is co-authored with Dr. Y. Kodera and Dr. J. E. Garay, and is currently in preparation for submission to publish. The dissertation author was the primary investigator and author of this paper.

Chapter 3, in full, is co-authored with Dr. Y. Kodera and Dr. J. E. Garay, and has been submitted for publication of the material as it may appear in Materials and Design. The dissertation author was the primary investigator and author of this paper.

VITA

2016	Bachelor of Science in Physics, Peking University
2018	Master of Science in Material Science and Engineering, University of California San Diego
2022	Doctor of Philosophy in Material Science and Engineering, University of California San Diego

PUBLICATIONS

X. Wu, L. Tang, C. L. Hardin, C. Dames, Y. Kodera, and J. E. Garay. "Thermal conductivity and management in laser gain materials: A nano/microstructural perspective", *J. Appl. Phys.* 131 (2022) 020902.

X. Wu, Y. Kodera, and J. E. Garay. "Improved light transmission in nanocrystalline aluminum nitride (AlN)—enabling a lightweight, thermal shock resistant transparent ceramic" *Submitted.*

X. Wu, Y. Kodera, and J. E. Garay. "Fabrication of highly transparent Thulium-doped Al2O3 nanocrystalline ceramics" *Submitted.*

FIELD OF STUDY

Major Field: Engineering

Studies in Material Science and Engineering
Professor Javier E. Garay

ABSTRACT OF THE DISSERTATION

Synthesis and Densification of Nanocrystalline Al_2O_3 and AlN Ceramics with Improved Optical Transparency for Thermally Robust Photonic Applications

by

Xingzhong Wu

Doctor of Philosophy in Material Science and Engineering

University of California San Diego, 2022

Professor Javier E. Garay, Chair

Optical ceramics have attracted increasing interest because of their superior mechanical toughness, better homogeneity, and potential for scaling and microstructural design compared to state-of-the-art single crystals. Optical transparency in ceramics were traditionally only achievable using optically isotropic materials because of the birefringent scattering loss in optically anisotropic materials. However, commonly used optically isotropic materials have limited thermal conductivities that fundamentally restrain heat extraction in high power applications. Excessive temperature gradient caused by low thermal conductivity affects the light transmitting properties of these materials and can eventually lead to thermomechanical failure. One solution for this challenge is to use optically anisotropic materials such as aluminum oxide (alumina, Al_2O_3) and aluminum nitride (AlN) that have better thermal conductivity and superior mechanical toughness. By reducing the grain size of these optically anisotropic materials, scattering loss caused by birefringence can be minimized, thus recover the material transparency.

Here, transparent nanocrystalline thulium doped Al_2O_3 ceramic is produced and characterized, with the highest in-line transparency among rare earth doped Al_2O_3 ceramics reported. Nanocrystalline AlN powder is synthesized and densified using current-activated, pressure-assisted densification (CAPAD). The resulting AlN nanocrystalline ceramic is the finest-grained fully dense AlN ceramic reported and showed significant transparency improvement compared to transparent AlN ceramics reported. Finally, thulium dopant incorporation into lab synthesized nanocrystalline AlN is studied.

These results show the potential of nanocrystalline microstructure in enabling the use of optically anisotropic materials in transparent ceramic applications. The use of nanocrystalline Al_2O_3 and AlN ceramics may enable thermally and mechanically more robust light transmitting/emitting devices under challenging conditions. The significant improvement in transparency of nanocrystalline AlN ceramic by reducing its grain size to sub-micrometer range also broadens the material selection range for optical ceramics.

1. THERMAL CONDUCTIVITY AND MANAGEMENT IN LASER GAIN MATERIALS

1.1 Introduction and Motivation

Thermal management is one of the most important considerations when designing a solid-state laser system because a portion of the optical pump power is converted to waste heat rather than optical laser power. Thermal gradients in the gain media cause thermal lensing (reducing beam quality) and ultimately thermal stress fracture. Management strategies at the system level include water cooling of laser crystals and the use of highly thermally conductive heat sinks. Regardless of the pumping/cooling scheme, the maximum deliverable laser power scales directly with thermal conductivity, *k* of the gain media, so that a 10-fold increase in *k* translates to a 10 times more powerful laser. Thus, the thermal conductivity of the gain media itself plays a crucial role in the overall performance of the laser.

Since Maiman's first demonstration of the ruby laser in 1960,[1] numerous material systems have been investigated as candidates for solid-state laser gain media. Among them, the most widely used host materials include yttrium aluminum garnet (YAG), glass, sapphire, and many more.[2] With the development in laser technology, the desire to increase laser power has attracted increasing attention. As mentioned previously, the fundamental power limits are given by the thermal conductivity (controlling thermal gradients) and mechanical properties (controlling fracture) leading to the identification and development of host materials with fundamentally superior thermal/mechanical properties.

Figure 1.1 shows an overview of the room temperature thermal conductivity and Young's modulus of a variety of optical materials, as measures of intrinsic heat transport capability and mechanical robustness. The k values shown are for single crystals or large grained ceramic in order to highlight the highest and, therefore, most promising values. Young's modulus is a key indicator of intrinsic mechanical properties because it is relatively independent of the microstructure unlike fracture toughness and hardness that are highly dependent on material processing. As high thermal conductivity materials such as diamond and AlN are considered for laser applications,[3–7] microstructural engineering on the polycrystalline form of currently used materials is also explored to improve their thermal and mechanical properties. Microstructure is important because some of the highest k materials (Al_2O_3 and AlN) have anisotropic optical properties (birefringence), making light transmission a strong function of grain size. For polycrystalline materials whose grain sizes are comparable to or smaller than relevant light wavelengths, reducing the grain size minimizes light scattering as discussed in **Sec. 1.2.1**. However, larger grain sizes are beneficial for heat conduction since boundaries scatter phonons as discussed in **Sec. 1.2.2**.

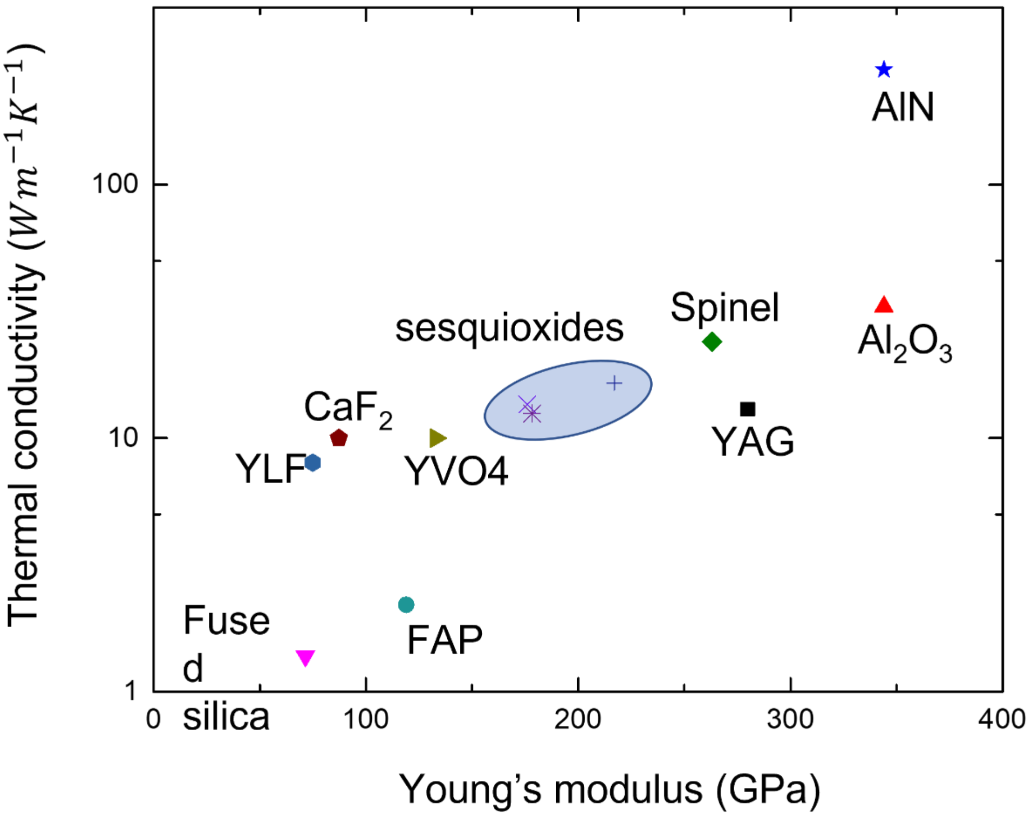

Figure 1.1 Room temperature thermal conductivity (log scale) and Young's modulus of commonly used and potential laser host materials. Data from L. Mezeix and D. J. Green, Int. J. Appl. Ceram. Technol. 3, 166–176 (2006). Copyright 2006 The American Institute of Physics; P. Klein and W. Croft, J. Appl. Phys. 53, 1689 (1967). Copyright 1967 The American Institute of Physics Shackelford et al., CRC Materials Science and Engineering Handbook. Copyright 2016 CRC Press LLC Powell et al., Thermal Conductivity of Selected Materials, Part 2. Copyright 1966 National Bureau of Standards Slack et al., J. Phys. Chem. Solids 48, 641–647 (1987). Copyright 1987 Pergamon Journals Ltd. Dahmani et al., J. Mater. Sci. 33, 4677–4685 (1998). Copyright 1998 Kluwer Academic Publishers Combis et al., Appl. Phys. Lett. 101, 211908 (2012). Copyright 2012 American Institute of Physics G. A. Slack, Phys. Rev. 126, 427–441 (1962). Copyright 1962 American Physical Society Yeheskel et al., J. Eur. Ceram. Soc. 31, 1703–1712 (2011). Copyright 2011 Elsevier Ltd. Peters et al., J. Cryst. Growth 237–239, 879–883 (2002). Copyright 2002 Elsevier Science B.V. Albayrak et al., J. Am. Ceram. Soc. 93, 2028 (2010). Copyright 2010 The American Ceramic Society Kaminskii et al., Laser Phys. Lett. 5, 300–303 (2008). Copyright 2008 Astro Ltd. Akchurin et al., Opt. Mater. 35, 444–450 (2013). Copyright 2013 Elsevier B.V. Popov et al., Dokl. Phys. 52, 7–9 (2007). Copyright 2007 Pleiades Publishing, Ltd. Ma et al., Opt. Commun. 275, 179–185 (2007). Copyright 2007 Elsevier B.V. Y. Sato and T. Taira, in Optics InfoBase Conference Paper. Copyright 2007 Optical Society of America Payne et al., IEEE J. Quantum Electron. 30, 170–179 (1994). Copyright 1994 IEEE Pollak et al., IEEE J. Quantum Electron. 18, 159–163 (1982). Copyright 1982 IEEE Faure et al., Opt. Mater. 6, 293–303 (1996). Copyright 1996 Elsevier Science B.V. (Refs. 8–26).

1.2 Background

1.2.1 Fundamentals of microstructural effects on optical properties

Traditionally, single crystals were the state-of-the-art material for laser applications, thanks to the high optical transparency of high-quality single crystals. While single crystal manufacturing is relatively mature after decades of technological advances, certain challenges such as dopant inhomogeneity and optical inhomogeneity caused by facets and cores from a conventional melt-growth method still exist.[27,28] In addition, microstructural defects such as twinning and inclusions can scatter light. On the other hand, polycrystalline optical ceramics provide alternatives to conventional single crystals, but it is not until recently that some polycrystalline ceramic materials were shown to rival their single crystal counterparts in terms of optical transparency.[29] With developments in ceramic sintering and densification technologies, novel powder densification approaches allow the fabrication of optical ceramics that are comparable to single crystals,[29] outperform single crystals,[30] or can be much more easily made as polycrystalline ceramics than single crystals.[31,32]

Loss mechanisms in single crystals involve mainly absorption caused by dopants or impurities. Although scattering loss from optical inhomogeneity still exists in single crystals made from conventional melt-growth approach, the loss coefficient can be reduced to a level as low as 1 dB/m for common optical single crystals such as sapphire and YAG.[33,34] On the other hand, light propagation in polycrystalline ceramics suffers from more scattering losses caused by (1) *Pores*, (2) *Secondary phases*, and (3) *Birefringence*, as detailed next.

Most conventional polycrystalline ceramics are opaque or translucent because of residual porosity after processing. Pores are gas (or vacuum) pockets with refractive index, n close to 1, while most ceramics considered for optical applications have refractive indices larger than 1.5.

The huge refractive index mismatch ($\Delta n>0.5$) between solid and pores causes intense light reflection and refraction. Therefore, conventional ceramics and porcelains often appear white because of the diffusely reflected environmental light.

The second scattering source is secondary phases. As most ceramic fabrication approaches involve densification/sintering of powder, the powder purity and homogeneity become vital for the uniformity of the densified ceramic. If the powder has more dopants/impurities than are soluble in the material lattice (or if the powder has unwanted phases), precipitation and segregation of secondary phases can happen during the densification process. For many materials such as ZrO_2 that go through phase transitions below or near the sintering temperature, secondary phase precipitation also causes inhomogeneity within the polycrystalline ceramic.[35,36] As light transmits across the grain boundary between two different phases, the refractive index mismatch (on the order of $\Delta n\sim 0.1$) again causes refraction and scattering of the propagating light.

It is worth noting that for optically isotropic materials, grain boundaries between the same phase do not cause scattering since refractive indices on either side of boundary are the same, regardless of the grain orientations. It has been reported that intergranular films can exist at grain boundaries for many materials[37] because of impurities or lattice distortion near the grain boundary, but the thickness of these layers is typically on the order of 1 nm, which is too thin to have significant interaction with electromagnetic waves with much longer wavelengths (on the order of $1\,\mu$m for many laser applications). With developments in ceramic densification and sintering technologies, transparency has been achieved for many cubic ceramic materials such as $Y_3Al_5O_{12}$ (YAG), $MgAl_2O_4$ (spinel), CaF_2, sesquioxides, and more,[20,29,30,32,38,39] showing that clean grain boundaries have no negative effect on optical transparency.

With a combination of optically isotropic material and low porosity, the effects of the first two scattering loss mechanisms discussed above can be minimized. However, for optically anisotropic materials with non-cubic crystal structures, birefringence scattering poses a great challenge to the optical application of the non-cubic material in the polycrystalline form. Because of the structural asymmetry in non-cubic materials, the refractive index of the material depends on the crystallographic orientation. A polycrystalline ceramic with an anisotropic structure and randomly oriented grains has discontinuities in refractive indices in the light propagation direction. This small Δn causes Rayleigh–Gans–Debye (RGD) type scattering loss, which reduces transparency in non-cubic ceramics such as polycrystalline Al_2O_3.[40]

The in-line transmission of materials with losses from light reflection, scattering, and absorption can be described using contributions of the individual loss mechanisms as[41]

$$T = T_R T_S T_A \, , \tag{1}$$

where T_R, T_S, and T_A are the transmission after reflection, scattering, and absorption losses, respectively. To decrease scattering losses and broaden material options for optical ceramics, significant efforts have been made to produce ceramics with sub-micrometer grains.[42] Apetz and van Bruggen used nanocrystalline Al_2O_3 ceramics as an example to study the grain size dependence of non-cubic ceramic in-line transmission, which showed that high in-line transparency can be achieved by reducing the grain size of Al_2O_3 ceramics.[42] As the ceramic grain size gets well below the wavelength of electromagnetic waves of interest, RGD-type scattering becomes much less efficient, therefore recovering the transparency of the ceramics, as indicated by

$$RIT = (1 - R_s)\exp\left(-\frac{3\pi^2 r \Delta n^2 d}{\lambda^2}\right) , \tag{2}$$

where RIT is real in-line transmission, R_s is reflection loss, r is grain size of the ceramic, d is thickness of the ceramic, and λ is the wavelength of light. In this model, only the reflection loss and the scattering loss are considered while the absorption loss is neglected. **Eq. (2)** proposed by Apetz and van Bruggen for alumina clearly shows that reducing the grain size r in non-cubic ceramics improves the in-line transparency.

This idea of grain size engineering on non-cubic ceramics has been further developed and highly transparent, optically active Al_2O_3 ceramics have been made for potential lasing and lighting applications.[43–46] Similar investigation on higher Δn materials such as AlN has also been made and translucency as well as photoluminescence have been achieved.[47] It has been shown that in both Al_2O_3 and AlN ceramics, fine grain size and grain boundary abundancy allow higher-than-equilibrium rare earth incorporation compared to single crystals.[44,46,48]

An important consideration for rare earth incorporation into host materials is the luminescence lifetime. It is well known that different host lattices and different doping concentrations can result in different luminescence lifetimes, since they change the local environment of dopant ions. Shortened lifetime at high dopant concentrations (known as concentration quenching) is due to dopant agglomeration. In polycrystalline ceramics, dopant segregation can also occur at the grain boundaries shortening the luminescence lifetime. However, it has been reported that it is possible to minimize this effect by optimizing the processing condition and reducing the grain size.[46] In a polycrystalline ceramic with smaller grain size, grain boundaries have larger volumes and increase the inter-ionic distance between dopants segregated at the grain boundaries, therefore reducing the segregation effect on luminescence lifetime.

Besides the scattering loss mechanisms discussed above, the effect of the microstructure on optical absorption line shape also brings unique properties to optical ceramics compared with single crystals. As Shachar and co-workers discussed, absorption broadening mechanisms in solid optical materials mainly involve Doppler broadening, natural broadening, collision broadening, and inhomogeneous broadening.[41] Doppler broadening originates from the relative velocity between an absorber and the light source, which causes an absorption frequency shift that is commonly known as the blue shift or red shift. In most cases for optical crystals, thermally induced velocities dominate the absorbers' movement relative to the light source. As thermally induced velocities of absorbers have random spatial directions, the net effect of random shifts is Gaussian broadening centered at the transition frequency.

The other two broadening mechanisms, natural broadening and collision broadening, are caused by the fundamental quantum mechanical time-energy uncertainty. As the excited state in a transition has a finite lifetime, the time-energy uncertainty brings an uncertainty to transition energy. The uncertainty propagates linearly to transition frequency and is referred to as natural broadening. Collision broadening has the same origin as natural broadening but with excited state lifetime shortened due to collisions in solids. With a shorter lifetime that translates to a larger energy uncertainty, collision broadening often dominates over natural broadening between these two Lorentzian-shaped broadening mechanisms.

Finally, inhomogeneous broadening originates from the variation of local environment of absorbers. This is especially significant for optical ceramics because they have grain boundaries near which energy levels for absorber transitions can be different from those in an undistorted lattice. Similar to how emission from amorphous optical glasses is broader than more ordered single crystals, polycrystalline optical ceramics can also have more significant inhomogeneous broadening than single crystals. This effect has been demonstrated in polycrystalline Al_2O_3 and makes optical ceramics attractive candidates for certain applications where absorption/emission width is of interest.[46]

1.2.2 Fundamentals of microstructural effects on thermal conductivity

Doped polycrystalline ceramics are increasing in popularity as gain media in solid-state lasers. When analyzing the thermal conductivity of such materials, it is important to consider the underlying microstructure. Accordingly, in this section, we will present a model consisting of different scattering mechanisms, including grain boundaries and dopants that cause mass defect scattering, and use it to briefly discuss the underlying physics of the microstructural effects on the thermal conductivity of those laser gain materials.

Since typical polycrystalline laser gain media are dielectrics with large bandgaps, phonons are the dominant heat carriers. Therefore, the thermal conductivity of those materials can be calculated using kinetic theory,[49,50]

$$k = \frac{1}{3} \sum_{pol} \int C_\omega v_\omega \Lambda_\omega d\omega \,, \tag{3}$$

where C_ω, v_ω, and Λ_ω are, respectively, the spectral heat capacity, group velocity, and mean free path of the phonons, ω is the angular frequency, and the summation accounts for the three acoustic phonon polarizations. C_ω and v_ω are determined entirely by the phonon dispersion relation and as such are relatively straightforward to understand and model as compared to Λ_ω. For simplicity, here we are approximating the dispersion relation as isotropic. In addition, we focus on fully dense homogenous materials, such that the effects of the pores and phase inclusions on the thermal conductivity are negligible.

For this idealization of RE-doped polycrystalline laser gain materials, the dominant phonon scattering mechanisms include both intrinsic and extrinsic phenomena. Here *intrinsic* refers to those scattering physics present in even a high-quality single crystal, namely phonon-phonon (also known as umklapp) scattering and phonon-impurity scattering; for the latter, the "intrinsic" impurities mean the natural isotopic variations of the constituent atoms. *Extrinsic* scattering refers to phonon scattering at grain boundaries and at mass defects like rare earth (RE) or transition metal dopants. As such, the overall effective mean free path to be used in **Eq. (3)** can be calculated by combining all relevant scattering mechanisms in parallel using Matthiessen's rule,

$$\Lambda_{eff,\omega}^{-1} = \Lambda_{umk,\omega}^{-1} + \Lambda_{imp,\omega}^{-1} + \Lambda_{gb,\omega}^{-1} + \Lambda_{md,\omega}^{-1} \,, \tag{4}$$

where $\Lambda_{umk,\omega}$, $\Lambda_{imp,\omega}$, $\Lambda_{gb,\omega}$, and $\Lambda_{md,\omega}$ are the frequency-dependent mean free paths (MFPs), respectively, due to umklapp, impurity, grain boundary, and mass defect scattering due to the RE dopants.

For undoped single crystal materials, the dominant scattering mechanisms are umklapp and impurity scattering, and the MFPs associated with these scatterings can be determined by fitting simple MFP models to literature k vs temperature (T) data for high-quality single crystals. As an example of this, **Figure 1.2** shows experimental data[51] for $k(T)$ of single crystal YAG (black filled circles, Yagi 2007), in which $k(T)$ first increases to reach a peak of ∼800 W/m K at ∼25 K and then starts to fall steeply with temperature, up to and beyond room temperature.

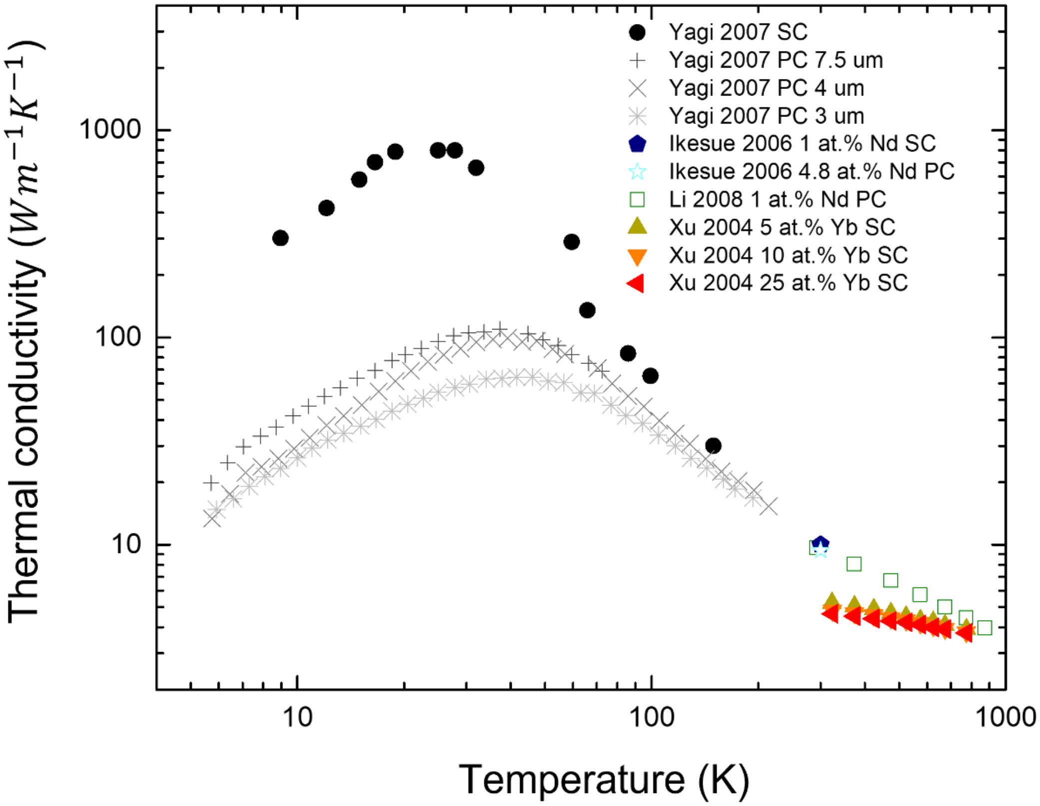

Figure 1.2 Effects of doping and grain size on the temperature-dependent thermal conductivity of YAG. Data from Li *et al.*, Opt. Mater. **31**, 6–17 (2008). Copyright 2008 Elsevier B.V. Yagi *et al.*, Ceram. Int. **33**, 711–714 (2007). Copyright 2007 Elsevier Ltd and Techna Group S.r.l. Xu *et al.*, Solid State Commun. **130**, 529–532 (2004). Copyright 2004 Elsevier Ltd. Ikesue *et al.*, Annu. Rev. Mater. Res. **36**, 397–429 (2006). Copyright 2006 Annual Reviews (Refs. 28, 51, 60, and 61). For doped samples, the doping species and concentration are specified in the legend. SC and PC, respectively, denote single crystal and polycrystalline YAG. For selected polycrystalline ceramics, the grain size is specified in μm.

The scattering mechanisms dominating these increasing and decreasing $k(T)$ trends, respectively, at low and high temperatures are well understood.[50,52] In the low-temperature limit of single-crystal YAG, phonon-phonon and phonon-impurity scattering both “freeze out” so that $\Lambda_{umk,\omega}$ and $\Lambda_{imp,\omega}$ both can be approximated as ∞ for practical purposes. In this case, the only remaining phonon scattering is at the physical boundaries of the sample, which classically corresponds to a $k(T)$ power law of T^3 due to the Debye heat capacity.[53] This physical boundary scattering effect could easily be added to the model of **Eq. (4)** as another MFP term, Λ_{bdy}, as is routinely done in other communities.[49,50,54,55] However, this is unimportant for k of polycrystalline laser gain materials for two reasons. First, the grain sizes in these polycrystalline materials are much finer than the overall sample sizes, so that physical boundary scattering is much weaker than grain boundary scattering of phonons. Second, here we are focused on lasing in the more common and practical cases in which the operating temperatures are near or above room temperature, such that the phonon-phonon scattering also dominates the physical boundary scattering.

Now focusing on the high-temperature regime of undoped single-crystal YAG in **Figure 1.2**, the primary scattering mechanism is phonon-phonon (umklapp) scattering, which classically leads to $k(T) \propto T^{-1}$ for $T \gtrsim \frac{1}{3}\theta_D$, where θ_D is the Debye temperature. Intrinsic impurity scattering will also play a role near the peak in $k(T)$. As such, one can obtain $\Lambda_{umk,\omega}$ and $\Lambda_{imp,\omega}$ by fitting the single crystal $k(T)$ data to the theoretical model of **Eqs. (1) and (2)**. Yet, it should be noted that two modifications need to be made for **Eq. (4)** for such fitting process. First, the $\Lambda_{gb,\omega}$ and $\Lambda_{md,\omega}$ terms should be ignored, since the MFPs associated with the scatterings from grain boundaries and mass defects like dopants do not exist in the pure single crystals. Second, the additional MFP related to the physical boundary scattering, Λ_{bdy}, should be added to **Eq. (4)** since it is important for the low-temperature regime [below the peak in $k(T)$] as mentioned in the previous paragraph. Thus, fitting the full $k(T)$ range for undoped single-crystal YAG will determine $\Lambda_{umk,\omega}$, $\Lambda_{imp,\omega}$, and Λ_{bdy}.

For doped polycrystalline materials, the *extrinsic* mean free paths $\Lambda_{gb,\omega}$ and $\Lambda_{md,\omega}$ also play major roles in further limiting the heat transport and can be combined with $\Lambda_{umk,\omega}$ and $\Lambda_{imp,\omega}$ already determined from the undoped single-crystal. Hence, understanding how grain boundary and mass defect scattering due to dopants affect the thermal conductivity are essential for developing high-power lasers with high k.

In general, polycrystalline materials have smaller thermal conductivities compared to their single crystal counterparts due to phonon scattering by grain boundaries. The magnitude of this k reduction depends on many factors such as the sizes, orientation, and quality of the grain boundaries. Here, for simplicity, we focus on the effects of the average grain size, D. Generally speaking, k decreases with decreasing grain size since $\Lambda_{gb,\omega}$ also becomes shorter, typically following $\Lambda_{gb,\omega} \propto D$.[56] To give an example, note from **Figure 1.2** that the measured k values of all the polycrystalline samples[51] are smaller than that of the single crystal, and indeed, k increases monotonically with D due to the phonon scattering by grain boundaries. Furthermore, the maximum thermal conductivities are 64, 99, and 110 W/m K for the polycrystalline YAG with 3, 4, and 7.5 μm grain size at temperatures of 46, 39, and 37 K, respectively.

Similarly, Watari *et al.*[57] fabricated two polycrystalline AlN samples with different grain sizes and found that the maximum thermal conductivity increases from 260 to 655 W/m K at a temperature of $\sim$175 and 90 K, when grain size increases from 5 to 8 μm, respectively. These samples were not intended to be gain materials but serve well for discussion purposes; AlN is discussed in more detail in **Sec. 1.3.2.4**. Note that these polycrystalline AlN samples have much higher thermal conductivities than the polycrystalline YAG due in part to the much larger intrinsic single crystal k value in AlN (e.g., $\sim$319 W/m K for single-crystal AlN,[12] compared to $\sim$13 W/m K for single-crystal YAG,[9] in both cases referring to undoped samples at 300 K). Therefore, ceramic materials with large single crystal thermal conductivities and coarse grain sizes are preferred for developing high-k polycrystalline laser gain media. Note that this is in tension with the material synthesis and optical criteria, which favor fine grain sizes for easier nonequilibrium RE doping and reduced photon scattering (discussed in **Sec. 1.3.2.2**).

Besides phonon scattering by grain boundaries, RE dopants also play an important role in the thermal conductivity of polycrystalline laser gain materials. **Figure 1.3** shows the thermal conductivity of YAG as a function of Nd doping, obtained from Sato *et al*.[58] The thermal conductivity decreases with increasing doping concentration, and the k of 5.4 at. % Nd-doped polycrystalline YAG is about 10%–15% smaller than that of the undoped sample for all temperatures shown in **Figure 1.3**. This is because the increased Nd concentrations increase the rate of mass defect scattering, which reduces $\Lambda_{md,\omega}$ and thus k. Therefore, maximizing k requires minimizing the RE doping concentrations, which again is in conflict with the requirements for lasing.

Finally, it is worth noting that $\Lambda_{gb,\omega}$ may depend on the phonon transport direction if the material has a highly anisotropic microstructure, for example, needle-like rather than equiaxed grains. In that case, the grain boundary scattering MFPs need to be calculated separately for each different direction of the microstructure.[59] This anisotropic concept will be briefly explored further in **Sec. 1.4**.

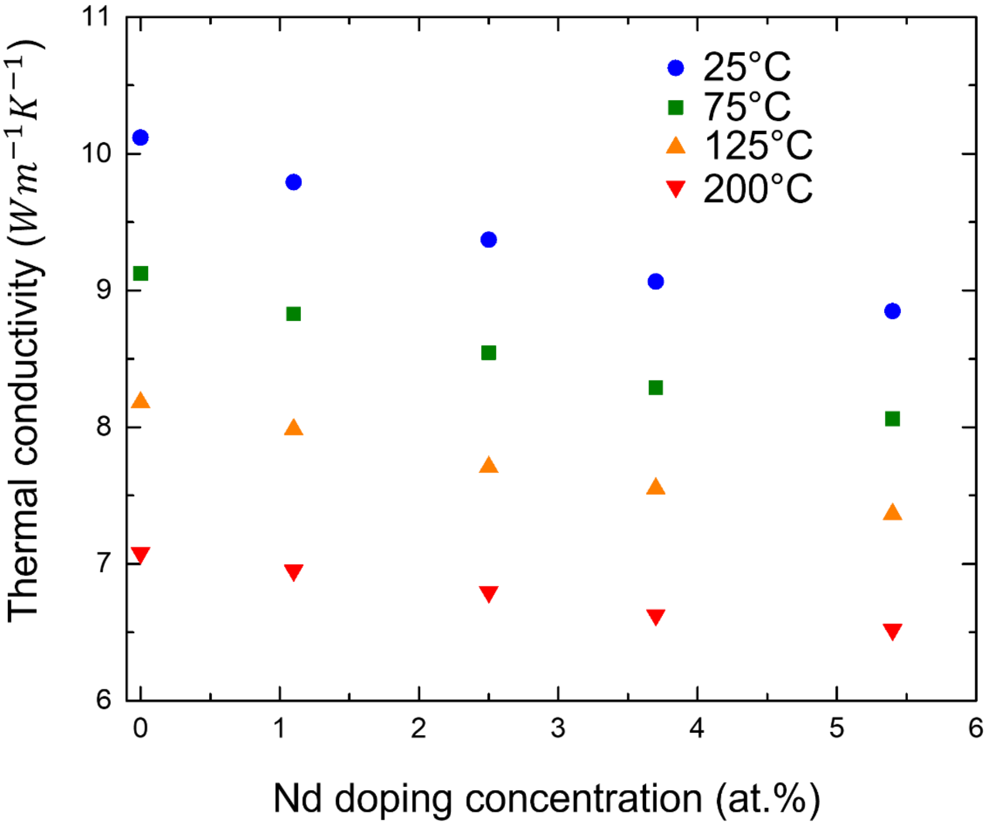

Figure 1.3 Thermal conductivity of Nd-doped polycrystalline YAG at four different temperatures from Ref. 58. The average grain sizes of the samples were ∼60 μm, which is so large as to have no significant effect on the thermal conductivity, and similar *k* results were obtained for single-crystal samples with the same doping levels. Here, the doping reduces the thermal conductivity by ∼10%–15%. In materials with higher single-crystal *k*, such as AlN (not shown), the deleterious effects of doping are stronger.

1.3 Previous Work on Thermal Conductivity in Gain Media

In this section, we will discuss the thermal and mechanical properties of a variety of crystalline material systems, either in single crystal or in polycrystal form. Some like YAG are workhorse gain materials while others like the sesquioxides and AlN have the potential to be important in future high-power laser designs because of their high thermal conductivities.

1.3.1 Optically isotropic materials

Crystalline materials with cubic crystal structures have the same refractive indices along different crystallographic directions and are therefore optically isotropic. As discussed in **Sec. 1.2.1**, optically isotropic materials do not have birefringence, simplifying orientational considerations in single crystal scenarios. When made in the polycrystalline form, assuming there are no other phases at the grain boundaries, optically isotropic materials do not have discontinuities in refractive index between grains, which makes it easier to achieve optical transparency.

1. Yttrium aluminum garnet

The most used crystalline laser gain medium for solid state lasers is yttrium aluminum garnet $Y_3Al_5O_{12}$ (YAG) single crystal. Because of the unique combination of cations (Y^{3+} and Al^{3+}), the YAG lattice provides two different cation sites for optically active ion substitution. Therefore, the YAG single crystal can be doped with a variety of RE elements such as Nd^{3+}, Er^{3+}, Tm^{3+}, Ho^{3+}, which substitutes Y^{3+} in the lattice, and transition metal elements such as Cr^{3+} that substitute Al^{3+}, providing a wide selection of emission wavelengths. Because of its relatively good thermal conductivity and mechanical properties compared with many other laser materials such as YVO_4 and glass hosts,[46,62] YAG single crystal remains the material of choice for many high-power laser applications.

With recent developments in ceramic sintering and densification technologies, polycrystalline YAG ceramics attracted much interest because of superior doping capability, dopant homogeneity, and mechanical properties, while still maintaining comparable thermal conductivity as single-crystal YAG.[28,62,63] It has been reported that the polycrystalline/nanocrystalline microstructure of YAG ceramics improves the fracture toughness of the material.[28,64,65] Polycrystalline YAG ceramics were also shown to allow higher doping concentration while maintaining better dopant homogeneity than single crystals.[27,63] Lab-scale polycrystalline Nd:YAG ceramics have been demonstrated with excellent optical quality comparable to single crystals[28,29,66,67] while lasers based on commercial scale polycrystalline Nd:YAG ceramics showed capability of 67 kW (Ref. 68) and >100 kW (Ref. 69) power output.

Temperature-dependent thermal conductivities of undoped/doped single crystal and polycrystalline YAG have been thoroughly studied in the past several decades. **Figure 1.2** shows YAG thermal conductivities measured recently. Ikesue and co-workers found that their heavily doped vacuum sintered 4.8 at. % Nd:YAG polycrystalline ceramic had a room temperature thermal conductivity of 9.4 W m^{-1} K^{-1}, which is comparable to 10 W m^{-1} K^{-1} they measured for a 1 at. % Nd:YAG single crystal.[61] Thermal conductivity above room temperature is of great engineering importance since laser crystals always heat up in working conditions. Xu *et al*. grew Yb-doped YAG single crystals using the Czochralski method and measured their thermal conductivities up to 500 °C. The thermal conductivity decreased from 5.2 to 3.9 Wm^{-1} K^{-1} for 5 at. % Yb:YAG and from 4.6 to 3.8 Wm^{-1} K^{-1} for 25 at. % Yb:YAG as temperature increased from room temperature to 500 °C. Heavy doping and high temperature reduce the thermal conductivity as expected (see **Sec. 1.2.2**).[60] Li and co-workers measured the thermal conductivity of 1 at. % Nd:YAG polycrystal fabricated through vacuum sintering from room temperature up to 600 °C. The thermal conductivity decreases from 9.7 to 4.0 Wm^{-1} K^{-1} as temperature increases.[28]

Yagi and co-workers studied the cryogenic temperature thermal conductivity of pure (not intentionally doped) YAG. While single crystal YAG reaches a maximum thermal conductivity of 800 Wm^{-1} K^{-1} around 25 K, the polycrystalline YAG samples they fabricated through vacuum sintering peaked at around 40 K with thermal conductivities between 64 and 110 Wm^{-1} K^{-1}, depending on the grain size.[51] They showed that YAG with smaller grain size has lower thermal conductivity, especially at low temperatures, which they attributed to grain boundary scattering that reduces the phonon mean free path. In general, YAG polycrystalline ceramics are as thermally conductive as YAG single crystals at and above room temperature. However, at low temperatures, especially when lower than 200 K, YAG polycrystals suffer from grain boundary scattering of phonons, which lead to a lower thermal conductivity compared with single crystals. From a laser design standpoint, the lower k caused by polycrystallinity could be problematic for cryogenically cooled lasers but less so for traditionally cooled designs.

Table 1.1 shows a compilation of selected thermal/mechanical studies on YAG single crystals and polycrystalline ceramics. Kaminskii and co-workers vacuum sintered YAG ceramic and showed a nearly fivefold improvement to fracture toughness when compared with a single crystal YAG sample.[64] Mezeix and Green showed that commercial polycrystalline 1 wt. % Nd:YAG with an average grain size of 2.22 μm has Young's modulus of 287 GPa, which is comparable to the 280 GPa value they measured for a 1 wt. % Nd:YAG single crystal along the <111> direction.[8] They also measured other elastic constants including shear modulus, bulk modulus, and Poisson's ratio that are comparable between single crystal and polycrystal samples, with fracture toughness 7% higher for the polycrystal.

Table 1.1 Selected thermal and mechanical properties of YAG single crystals and polycrystalline ceramics.

	YAG SC	YAG ceramic	Grain size	Preparation method	Reference
Young's modulus (GPa)	279.9<1 1 1> (1 wt% Nd doped)	283.6 (1 wt% Nd doped)	2.22 μm		L. Mezeix, D. Green [8]
		221 (1 at.% Nd doped)	15 μm	Vacuum sintering	J. Li et al. [28]
	285	285	186 nm - 26 μm	High pressure SPS	M. Sokol et al. [65]
Fracture toughness, K_{IC} (MPa m$^{1/2}$)	1.8 (undoped)	8.7 (undoped) 5.2 (Nd doped)		Vacuum sintering Vacuum sintering	A. Kaminskii, et al. [64]
	2.2 (1 at.% Nd doped)	1.5 (1 at.% Nd doped)	15 μm		T.I. Mah, et al. [151]
	1.64	2.18			G.J. Quarles. [152]
	1.04	1.41			R. Gentilman, [153]
	1.48 (1 wt% Nd doped)	1.59 (1 wt% Nd doped)	2.22 μm		L. Mezeix, D.J. Green [8]
	2.06	2.21(1 at.% Nd doped)	15 μm	Vacuum sintering	J. Li et al. [28]
Thermal conductivity, *k* (Wm^{-1}K^{-1})	13 (300K, undoped) 15 (300K, 1.4×10^{20}/cm^3 Nd) 11 (300K, 4.2×10^{19}/cm^3 Nd)				P. Klein, W. Croft [9]
	4.6-5.2 (5-25 at.% Yb doped)				X. Xu et al. [60]
	10.0 (1 at.% Nd doped)	9.8 (4.8 at.% Nd doped)			A. Ikesue et al. [61]
	290 (60K, undoped)	60-82 (60K, undoped)	3-7.5 μm	Vacuum sintering	H. Yagi et al. [51]
		9.7 (300K, 1 at.% Nd doped)	15 μm	Vacuum sintering	J. Li et al. [28]
	10.1-9.6 (300K, 0-1.3 at.% Nd doped)	10.1-8.8 (300K, 0-5.4 at.% Nd doped)	3-60 μm		Y Sato et al. [58]
		10-7 (300K, 1-20 at.% Yb doped)			B. Garrec et al. [78]

Subsequent studies also support the possibility of improving fracture toughness of YAG ceramics by reducing the grain size. Li and co-workers showed that their vacuum-sintered Nd:YAG ceramic with 15 μm grain size has 7% higher fracture toughness compared to a single-crystal Nd:YAG sample.[28] Sokol and co-workers fabricated a 1 at. % Nd:YAG polycrystal through high-pressure current-activated pressure-assisted densification (CAPAD)[70] (also referred to as high-pressure spark plasma sintering, HPSPS) and compared with a commercial 1.1 at. % Nd:YAG single crystal and a free sintered 1 at. % Nd:YAG polycrystal with grain size of 26 μm.[65] They found that the 1 at. % Nd:YAG ceramics they fabricated with grain sizes from 186 nm to 26 μm have comparable Young's modulus and shear modulus when compared with the single crystal, while the 186 nm sample from high-pressure CAPAD showed 22% improvement in Vicker's hardness and 155% improvement in bending strength and thermal shock resistance when compared to the single crystal. The thermal shock enhancement could be especially beneficial for high-power applications since thermal shock is the ultimate failure caused by over pumping of gain media. This would require successful doping of fine grained YAG; although this has not yet been demonstrated, one would not expect doping to reduce fracture toughness.

2. Sesquioxides

The sesquioxides Sc_2O_3, Y_2O_3, and Lu_2O_3 have gained increasing interest recently, mainly because of their somewhat higher thermal conductivity compared with state-of-the-art crystalline laser host YAG[31] as well as their doping compatibility with rare earth elements. These properties combined with their good mechanical properties make sesquioxides great materials for laser host material especially suitable for RE doping.[32] Although the improvements of thermal and mechanical properties of sesquioxides over YAG are not remarkably significant compared to

Al_2O_3 (discussed in **Sec. 1.3.2.2**), sesquioxides have superior thermal and mechanical properties compared to glass, making them excellent candidates for heavy RE doping applications. However, high-quality sesquioxide single crystals are technologically challenging to synthesize through conventional melt-growth methods due to the high melting temperatures above 2400 °C and requirements for special crucibles.[71] For example, high-quality single crystal Y_2O_3 is especially difficult to grow because its phase transition temperature is below the melting temperature, generating light scattering sources that impair the single crystal optical quality.[32] Therefore, great efforts have been made to achieve high-quality sesquioxide polycrystalline ceramics.[32,63,72]

Figure 1.4 shows selected thermal conductivity measurements on sesquioxide single crystals and polycrystalline ceramics. As expected (see **Sec. 1.2.2**), the thermal conductivity of sesquioxides highly depends on dopant concentration since they are often heavily doped. For most compositions, above 90 K, the thermal conductivity of sesquioxides decreases as temperature increases. **Table 1.2** shows a compilation of recent thermal/mechanical measurements on sesquioxide single crystals and polycrystalline ceramics. More details are discussed in the **Secs. 1.3.1.2 a–1.3.1.2 c** for each sesquioxide.

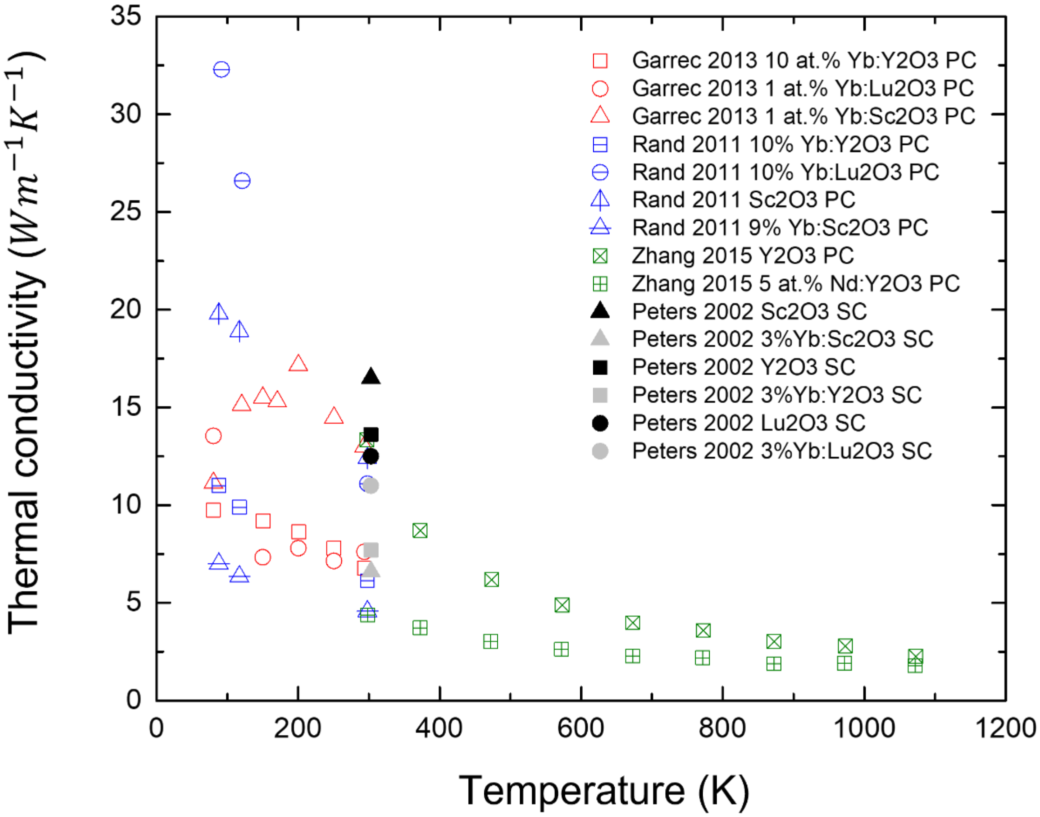

Figure 1.4 Temperature-dependent thermal conductivity of various sesquioxides: Sc_2O_3 (triangles), Y_2O_3 (squares), and Lu_2O_3 (circles). For doped samples, the doping species and concentration are specified in the legend. SC and PC, respectively, denote single crystal and polycrystalline sesquioxide samples. Data from Refs. 17, 39, 78, and 79.

Table 1.2 Selected thermal and mechanical properties of sesquioxides single crystals and polycrystalline ceramics.

	Sesquioxide SC	Sesquioxide ceramic	Grain size	Preparation method	Reference
Fracture toughness K_{IC} (MPa $m^{1/2}$)	1.0 (undoped Y_2O_3)				
		2.5 (undoped Y_2O_3)	1-2 μm		A. Kaminskii et al. [85]
		1.49 (Undoped Sc_2O_3)			G. Gogotsi [80]
		4.1 (undoped Lu_2O_3)		Vacuum sintering	A. Kaminskii et al. [19]
		1.5 (undoped Y_2O_3)	0.76 μm	HIP	I. Albayrak et al. [18]
		1.35 (Undoped Sc_2O_3)	1-3 μm		O. Yeheskel et al. [16]
		1.0 (0.5-5 at.% Nd:Y_2O_3, 298K)	7.9-11.5 μm	Vacuum sintering	L. Zhang, W. Pan [39]
Thermal conductivity, *k* ($Wm^{-1}K^{-1}$)	16.5-6.6(0-3% Yb:Sc_2O_3, 303K) 13.6-7.7(0-3% Yb:Y_2O_3, 303K) 12.5-11.0(0-3% Yb:Lu_2O_3, 303K)				V. Peters et al. [17]
	15.94-5.35 (0-15 at.% Yb:Y_2O_3, 298K)				Ji Hun Mun et al. [83]
		13.0 (undoped Y_2O_3, 298K)			T. Y. Fan et al, [84]
		12.4-4.57 (0-9% Yb:Sc_2O_3, 298K) 6.12 (10 at.% Yb:Y_2O_3, 298K) 11.1 (10 at.% Yb:Lu_2O_3, 298K)			D. Rand et al. [79]
		13.0 (1 at.% Yb:Sc_2O_3, 293K) 6.8 (10 at.% Yb:Y_2O_3, 293K) 7.6 (1 at.% Yb:Lu_2O_3, 293K)			B. Garrec et al. [78]
		13.3-4.4 (0-5 at.% Nd:Y_2O_3, 298K)		Vacuum sintering	L. Zhang, W. Pan [39]

a. Scandia (Sc_2O_3)

Despite the technological difficulties in Sc_2O_3 single crystal growth, Czochralski growth of RE^{3+}-doped Sc_2O_3 has been accomplished and laser oscillation has been demonstrated in Yb:Sc_2O_3, Nd:Sc_2O_3, Tm:Sc_2O_3, and Er:Sc_2O_3.[73–76] However, the size of the grown single crystal was limited because of the problems discussed above.[76] The thermal conductivity of an undoped Sc_2O_3 single crystal at room temperature was measured to be 16.5 $W\,m^{-1}\,K^{-1}$, while 3% Yb:Sc_2O_3 single crystal had a thermal conductivity of 6.6 $W\,m^{-1}\,K^{-1}$.[17]

In 2005, Li and co-workers synthesized Sc_2O_3 powder via a precipitation method and fabricated transparent Sc_2O_3 ceramics using vacuum sintering.[77] Fully dense Sc_2O_3 ceramic was sintered at 1700 °C with a resulting grain size of 9 μm. Thermal conductivities of 1 at. % Yb:Sc_2O_3, undoped Sc_2O_3, and 9 at. % Yb:Sc_2O_3 ceramics were measured by Garrec *et al.*[78] and Rand *et al.*[79] to be 12.4, 13.2, and 4.57 $Wm^{-1}\,K^{-1}$, respectively. At cryogenic temperature, 1 at. % doped Sc_2O_3 ceramic thermal conductivity peaks around 200 K at 18 $Wm^{-1}\,K^{-1}$.[78]

Another key parameter for a robust laser host material is fracture toughness. Gogotsi measured a fracture toughness, K_{IC}, of 1.49 $MPa\,m^{1/2}$ for Sc_2O_3 ceramic.[80] Yeheskel and co-workers measured a comparable value of 1.35 $MPa\,m^{1/2}$ for a hot isostatic pressed (HIPed) Sc_2O_3 ceramic.[16]

b. Yttria (Y_2O_3)

Y_2O_3 is the most well-studied material among the sesquioxides. Like Sc_2O_3, single crystal Y_2O_3 was successfully grown using a Czochralski method and laser oscillation was achieved in Tm:Y_2O_3, Nd:Y_2O_3, and Yb:Y_2O_3.[75,81,82] Klein and Croft measured single crystal thermal conductivity of 27 $Wm^{-1}\,K^{-1}$ for undoped Y_2O_3 and 13 $Wm^{-1}\,K^{-1}$ for 1 at. % Nd-doped Y_2O_3 at

300 K.[9] A more recent study by Peters *et al.* measured 13.6 $\mathrm{Wm^{-1}\,K^{-1}}$ for undoped Y_2O_3 and 7.7 $\mathrm{Wm^{-1}\,K^{-1}}$ for 3% Yb:Y_2O_3.[17] Mun and co-workers reported 16.0 $\mathrm{Wm^{-1}\,K^{-1}}$ for undoped Y_2O_3 single crystal and 5.4 $\mathrm{Wm^{-1}\,K^{-1}}$ for 15 at. % Yb:Y_2O_3 at room temperature.[83] In all cases, Y_2O_3 shows comparable or slightly higher thermal conductivity compared with YAG, making it an attractive material for RE-doped laser applications.

Room temperature k of undoped Y_2O_3 polycrystalline ceramic was measured by Fan *et al.* to be 13 $\mathrm{Wm^{-1}\,K^{-1}}$.[84] For 10 at. % doped Yb:Y_2O_3 heavily doped ceramics, Garrec *et al.* and Rand *et al.* reported $k = 7$ $\mathrm{Wm^{-1}\,K^{-1}}$ (Ref. 78) and $k = 6.1$ $\mathrm{Wm^{-1}\,K^{-1}}$ (Ref. 79), respectively, at room temperature. Cryogenic temperature measurements were also conducted in these studies and the thermal conductivity of Y_2O_3 increased by 50%–80% as temperature decreased to 77 K. The thermal conductivities of Nd^{3+}-doped Y_2O_3 ceramics at different doping concentrations from room temperature to 800 °C were measured by Zhang *et al.*[39] From room temperature to 800 °C, undoped Y_2O_3 ceramic thermal conductivity dropped from 13.3 to 3 $\mathrm{Wm^{-1}\,K^{-1}}$, while the thermal conductivities of Nd^{3+}-doped Y_2O_3 ceramics dropped from 4–6 to 2–3 $\mathrm{Wm^{-1}\,K^{-1}}$, depending on the doping concentrations.

Kaminskii *et al.* reported the fracture toughness K_{1C} value for Y_2O_3 single crystal to be 1.0 MPa $\mathrm{m^{1/2}}$, which is inferior to the YAG single crystal.[85] While polycrystalline ceramic Y_2O_3 is a great alternative to Y_2O_3 single crystals in terms of material processing, the mechanical properties of Y_2O_3 ceramic are also improved compared with single crystals. Fine-grained Y_2O_3 ceramics with grain sizes of 0.76–11.5 μm from vacuum sintering and HIPing are reported to have improved fracture toughness to 1.0–2.5 MPa $\mathrm{m^{1/2}}$, varying with different dopant concentrations and grain sizes.[18,39,85] Hardness of Y_2O_3 ceramic also showed 10%–30% improvement over single crystals.[39,85]

c. Lutetia (Lu_2O_3)

Lu_2O_3 has the heaviest cation among all the sesquioxides, making the thermal conductivity of undoped Lu_2O_3 lowest among the three. Mix reported room temperature thermal conductivity of Lu_2O_3 single crystal to be 12.2 $Wm^{-1} K^{-1}$,[86] which is lower than that for Sc_2O_3, Y_2O_3, and YAG. However, since the atomic mass of Lu is very close to that of RE dopant elements, Lu_2O_3 thermal conductivity is not much affected by heavy RE doping.[32] Measurement by Peters *et al.* showed that the undoped Lu_2O_3 single crystal has a thermal conductivity of 12.5 $Wm^{-1} K^{-1}$, while 3% Yb doping only reduced it to 11.0 $Wm^{-1} K^{-1}$, which is much higher than the other two sesquioxides with similar doping concentrations.[17]

Like Sc_2O_3 and Y_2O_3, polycrystalline Lu_2O_3 ceramics are great fabrication alternative to single crystals. Garrec reported 8 $Wm^{-1} K^{-1}$ for thermal conductivity of 1 at. % Yb:Lu_2O_3 polycrystalline ceramic[78] while Rand reported 11.1 $Wm^{-1} K^{-1}$ for 10 at. % Yb:Lu_2O_3,[79] which is more heavily doped. The discrepancy may be attributed to different grain sizes[78] and possibly different impurity levels and sample preparation. Nevertheless, these thermal conductivity values are comparable and even higher at certain temperatures compared with RE-doped Sc_2O_3 and Y_2O_3.

Single crystal Lu_2O_3 samples were successfully synthesized through a micropulling-down method,[87,88] laser heated pedestal growth,[87] and hydrothermal technique.[89] A laser experiment on a Yb:Lu_2O_3 single crystal has been demonstrated.[90] But reports on mechanical testing on Lu_2O_3 single crystals are lacking. Kaminskii and co-workers reported micro-hardness and fracture toughness of polycrystalline Lu_2O_3 ceramic H = 12.5 GPa and K_{1C} = 4.1 MPa $m^{1/2}$.[19]

3. CaF$_2$

Only 4 years after Maiman's first demonstration of the laser using SC ruby in 1960, the first polycrystalline ceramic laser was shown by Hatch and co-workers using hot pressed Dy:CaF$_2$.[91] CaF$_2$ is a well-known optical material with a wide transparency window from 0.15 to 9 μm, and growth of large size single crystals is relatively easy.[92] Thanks to the relatively large ionic radius of Ca^{2+} and the relatively open fluorite structure, CaF$_2$ can readily accommodate rare earth dopants making it a good laser host material. In recent years, incorporation of various rare earth elements into CaF$_2$ crystals have been shown for lasing applications, including Tm, Y:CaF$_2$,[93] Tm:CaF$_2$,[92] Na, Yb:CaF$_2$,[94] Nd, Y:CaF$_2$,[95–97] and Er, Pr:CaF$_2$.[98] Meanwhile, a great research effort has been made to fabricate polycrystalline rare earth-doped CaF$_2$ ceramic as a simpler approach compared with single crystal growth. Some drivers are a wide transparency window, a lower melting point (compared to oxides), and a low refractive index (∼1.4). Growing interest in RE:CaF$_2$ was seen in the past decade and Nd:CaF$_2$,[99] Nd, Y:CaF$_2$,[100] Yb:CaF$_2$,[20,101] Yb,Y:CaF$_2$,[102] Yb, Er:CaF$_2$,[103] Er:CaF$_2$,[104,105] Tm:CaF$_2$,[106] Ho:CaF$_2$,[107] and Eu:CaF$_2$ (Ref. 108) have all been demonstrated for laser applications.

Figure 1.5 shows the temperature-dependent thermal conductivity of CaF$_2$ single crystals and polycrystalline ceramics. Popov and co-workers used a stationary thermal flux method and showed that both naturally existing polycrystalline CaF$_2$ ceramics and artificially synthesized polycrystalline CaF$_2$ ceramics have comparable thermal conductivities compared to CaF$_2$ single crystals, with a room temperature value of around 10.3 Wm^{-1} K^{-1}.[21] 3ω3ω thermal conductivity measurements from Sarthou *et al*. support this room temperature result with a 10 Wm^{-1} K^{-1} value on an undoped CaF$_2$ polycrystal.[109] However, as temperature decreases, Popov *et al*. showed that the thermal conductivity increases up to 245 $Wm^{-1} K^{-1}$ at 50 K, while Sarthou *et al*. measured 73 $Wm^{-1} K^{-1}$ at 50 K. This discrepancy may be due to the grain size difference between these two studies. The CaF_2 polycrystals used in the former study have grain size around 100 μm, while in the latter study, the grain size of this specific sample was not reported, but other samples reported in the same study have grain sizes around 200 nm, which is much smaller than that in the former study.

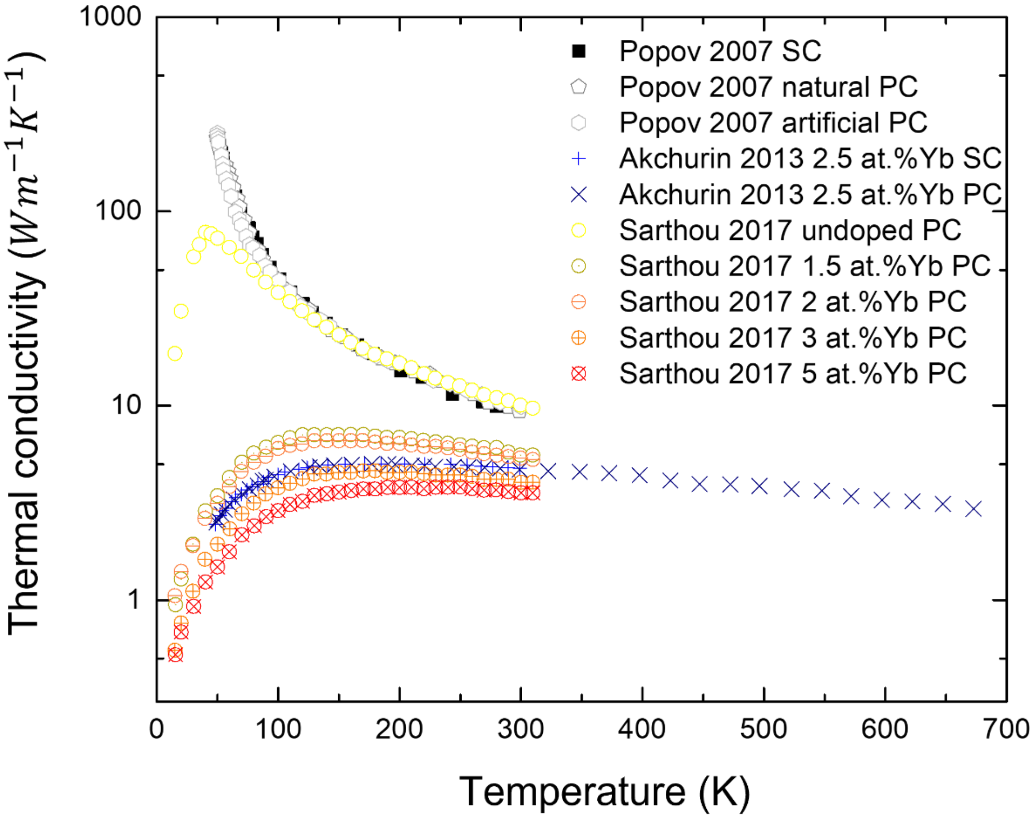

Figure 1.5 Temperature-dependent thermal conductivity of CaF_2. For doped samples, the doping species and concentration are specified in the legend. SC and PC, respectively, denote single crystal and polycrystalline CaF_2. Data from Refs. 20, 21, and 109.

For Yb-doped CaF_2, Akchurin and co-workers showed that a polycrystalline 2.5 at. % Yb:CaF_2 ceramic has comparable thermal conductivity as a single crystal sample with the same doping concentration, both with a room temperature value around 4.7 $Wm^{-1} K^{-1}$,[20] which is much lower than that of undoped CaF_2 samples mentioned above. Sarthou *et al.* showed similar result that 1.5–5 at. % Yb doping reduced the thermal conductivity of polycrystalline CaF_2 ceramic to 5.6–3.6 $Wm^{-1} K^{-1}$ compared to undoped samples.[109] In general, the thermal conductivity of CaF_2 is slightly lower that of YAG for both single crystals and polycrystalline ceramics.

Another weakness of CaF_2 compared with YAG is its inferior mechanical robustness. Akchurin and co-workers measured the fracture toughness K_{IC} of the CaF_2 single crystal and polycrystalline ceramics from different sintering approaches. They found out that the single crystal has a K_{IC} value of 0.45 MPa $m^{1/2}$, which is significantly lower than that of single crystal YAG, while CaF_2 ceramic prepared using hot-press showed nearly 50% improvement compared to the single crystal and other ceramics prepared using the hot forming method, with a K_{IC} value of 0.65 MPa $m^{1/2}$.[20] The lower thermal conductivity and fracture toughness of CaF_2 compared with YAG makes it more vulnerable to thermally induced fracture in HEL applications. However, with its lower melting point, wider transparency window, and wider absorption and emission spectra of dopant RE, CaF_2 is one of the best laser materials in certain aspects such as diode pumping and short pulse generation, that is also relatively easy to manufacture.

1.3.2 Optically anisotropic materials

Materials without cubic structural symmetry can have different refractive indices along different crystallographic directions and, therefore, are referred to as optically anisotropic materials. Common crystal structures like hexagonal and tetragonal have two different refractive indices and are referred to as birefringent materials. Unlike optically isotropic materials discussed above, birefringent materials require orientational considerations in single crystal applications. Also, when made as polycrystalline ceramics, birefringent scattering can cause transmission loss between adjacent grains (see **Sec. 1.2.1**), making it much more difficult to achieve high transparency. However, the excellent thermal and mechanical properties of some anisotropic materials, such as Al_2O_3 and AlN, promise such significant performance improvement over any currently used isotropic material that great research efforts are being made to overcome the aforementioned challenges.

1. YVO_4

One of the most widely used non-cubic rare earth laser host materials is yttrium orthovanadate (YVO_4). With its tetragonal structure, YVO_4 is birefringent and has a high $\Delta n > 0.2$ across the visible and infrared spectrum. Early in 1966, O'Conner showed in a spectroscopic study that Nd:YVO_4 could become an important laser system.[110] In 1977, Tucker and co-workers measured the stimulated emission cross section in Nd:YVO_4 and found out it is superior to Nd:YAG.[111] In 1987, Fields, Birnbaum, and Fincher demonstrated the first diode laser pumped Nd:YVO_4 laser and showed it has a lower lasing threshold and comparable slope efficiency compared with a similar Nd:YAG laser.[112]

Despite the superior absorption/stimulated emission cross section and gain of Nd:YVO_4 compared with Nd:YAG, it suffers from a lower thermal conductivity and mechanical toughness. Sato and Taira reported thermal conductivities of 9.0 and 12.0 $Wm^{-1} K^{-1}$ along the a-axis and c-axis, respectively, in the Nd:YVO_4 single crystal.[113] Lower values around 5.2 $Wm^{-1} K^{-1}$ have also been reported in numerous works.[114–116] A recent study on

$Nd:YVO_4$ amplifier crystals by Salem and co-workers showed that its fracture toughness is 0.48 MPa $m^{1/2}$, which makes it much more brittle than Nd:YAG.[117]

As discussed above, reducing the grain size in ceramics can improve their fracture toughness and, hence, potentially outperform their singe crystal counterparts. However, this approach is currently not suitable for YVO_4. The large Δn over 0.2 in YVO_4 can cause intense light refraction between adjacent grains in a YVO_4 polycrystalline ceramic, which will lead to a loss of transparency to the ceramic (see **Sec. 1.2.1**). Therefore, the use of YVO_4 in optical applications is currently limited to single crystals, which are more vulnerable to thermally induced failure compared to YAG single crystals and ceramics.

2. Alumina (Al_2O_3)

Single-crystal Al_2O_3 (sapphire) has a long history as the transition metal doped laser gain material, including the very first laser demonstrated, Cr-doped ruby.[1] Titanium-doped sapphire ($Ti:Al_2O_3$) is currently the most widely used tunable laser material[118] and has enabled numerous scientific and technological innovations. Al_2O_3 has a much higher thermal conductivity (30–35 $W m^{-1} K^{-1}$)[11] compared with YAG (10–14 $W m^{-1} K^{-1}$)[9] at room temperature, allowing more efficient heat extraction and lower temperature gradients in the laser crystal. Moreover, Al_2O_3 (alumina) is a well-known structural ceramic that has an impressive fracture stress of 3.5 MPa $m^{1/2}$.[119] The thermal shock resistance of Al_2O_3 is more than 20 times higher than that of YAG, making it a great host material for high-power applications.[46] Together with its high hardness and good chemical stability over a large temperature range, Al_2O_3 is one of the most robust candidates for the laser gain material.

Since its first demonstration in 1982 by Moulton,[120] titanium-doped sapphire has been the leading material for tunable lasers. The Ti:sapphire laser offers wavelength tunability over a wide wavelength range (700–1100 nm)[121] as well as capability of ultrafast femtosecond pulse generation. The importance of Ti:sapphire laser technology can be easily recognized with the crucial role it played in high-impact research such as femtochemistry (Zewail, Nobel Prize, 1999), the frequency comb technique (Hall and Hänsch, Nobel Prize, 2005), and chirped pulse amplification (Mourou and Strickland, Nobel Prize, 2018).

Despite the excellent thermal and mechanical properties of Al_2O_3 and scientific/commercial success of Ti:Al_2O_3 lasers, the doping of Al_2O_3 single crystal has been relatively limited to several transition metals such as Ti and Cr. Unlike the YAG lattice having large Y^{3+} sites to accommodate RE^{3+} dopants, the Al_2O_3 lattice only has smaller Al^{3+} sites that are energetically unfavorable for RE^{3+} to substitute. This leads to the low equilibrium solubility of RE^{3+} in Al_2O_3 single crystals ($\sim 10^{-3}$ at.%),[122] which makes it difficult, if not impossible, to produce RE^{3+} doped Al_2O_3 single crystals that contain enough RE^{3+} for practical laser applications.

Alternatives to Al_2O_3 single crystals include powders, thin films, and polycrystalline ceramics. Random lasing in RE-doped Al_2O_3 powders was achieved by Rand and co-workers.[123,124] RF-magnetron sputtering[125] and pulsed laser deposition (PLD)[126,127] showed success in RE incorporation into Al_2O_3 thin films with measurable photoluminescence (PL). Nd:sapphire thin films with Nd concentrations of 0.3–2 at. % were reported by Waeselmann and co-workers.[128–130] These achievements show the possibility of RE incorporation into Al_2O_3 structures through non-equilibrium approaches. However, with powders losing the thermal and mechanical advantages of Al_2O_3 and thin films hard to scale up, bulk RE-doped Al_2O_3 materials are still needed for potential higher power applications.

Polycrystalline Al_2O_3 ceramic, on the other hand, provides the possibility of RE incorporation and bulk material scalability, while maintaining the excellent thermal and mechanical properties at the same time.[119] In 2013, Sanamyan *et al.* reported synthesis and densification of Er^{3+}:Al_2O_3 ceramic showing PL from Er^{3+}.[43] In the same year, Penilla *et al.* reported visible wavelength PL in Tb^{3+}:Al_2O_3 ceramic with a preliminary thermal conductivity measurement of 30 $Wm^{-1}\,K^{-1}$.[44] In 2018, Penilla and co-workers conducted gain experiments on Nd:Al_2O_3 ceramic, marking the possibility of RE-doped Al_2O_3 ceramic being used as laser gain media.[46] In both works, the higher than equilibrium RE concentration was attributed to the non-equilibrium densification technique and the abundant grain boundaries in nanocrystalline ceramics. However, thermal and mechanical characterization were lacking in the RE:Al_2O_3 works mentioned above.

Figure 1.6 shows selected thermal conductivity measurements on Al_2O_3 single crystals and polycrystalline ceramics. Burghartz and Schulz measured 33 $Wm^{-1}\,K^{-1}$ at room temperature and 125 $Wm^{-1}\,K^{-1}$ at 100 K for single crystal sapphire.[131] Xie and co-workers measured the thermal conductivity of 99% and 92% dense alumina ceramics between 20 and 400 K and reported 15.3 and 12.5 $Wm^{-1}\,K^{-1}$, respectively, at room temperature, which is significantly lower than single crystal sapphire measurements.[132] However, Penilla and co-workers measured transparent 250 nm grain size Al_2O_3 fabricated though CAPAD and reported 30 $Wm^{-1}\,K^{-1}$ at room temperature, which is comparable to single crystals.[44]

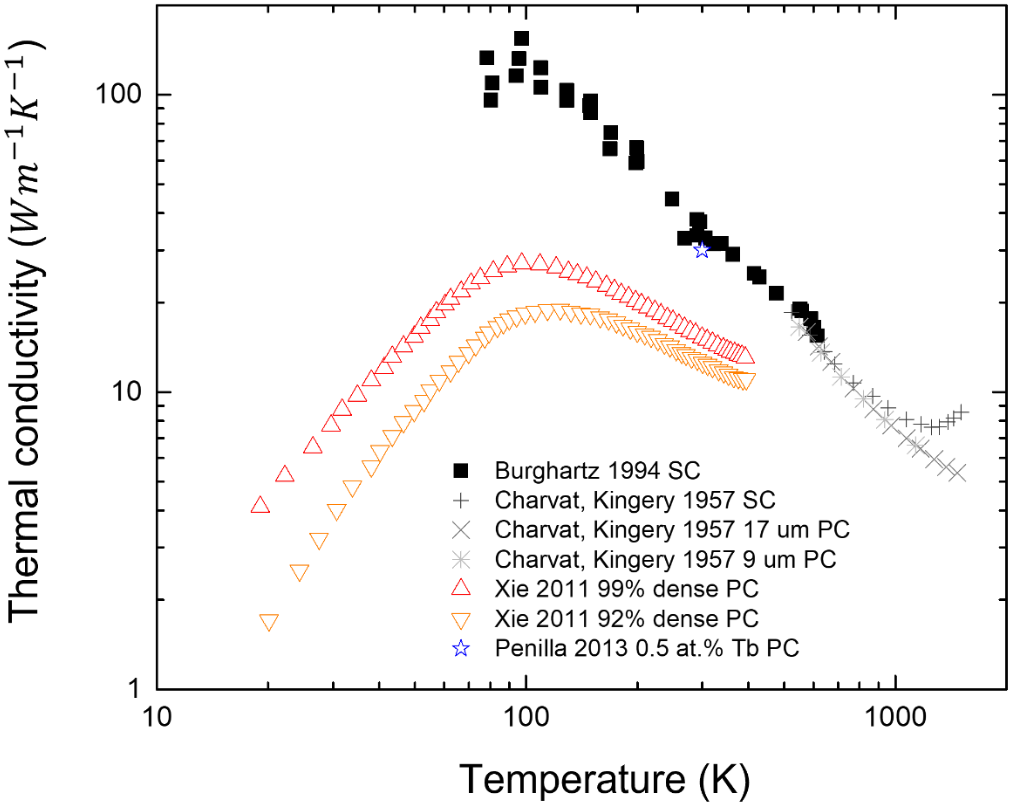

Figure 1.6 Temperature-dependent thermal conductivity of Al_2O_3. For doped samples, the doping species and concentration are specified in the legend. SC and PC, respectively, denote single crystal and polycrystalline Al_2O_3. Data from Refs. 44, 131, 132, and 155.

Table 1.3 shows more selected thermal/mechanical measurements on Al_2O_3 single crystals and polycrystalline ceramics. Smith *et al.* reported 25.9–32.8 $Wm^{-1}\,K^{-1}$ for free sintered Al_2O_3 ceramic with grain sizes between 1.5 and 20 μm,[133] showing that Al_2O_3 ceramics with the well-controlled impurity level and minimal porosity have comparable thermal conductivity as single crystal sapphire at room temperature. Tani and co-workers fabricated Al_2O_3 ceramics with grain sizes of 6.2–60.1 μm through hot press with subsequent HIP annealing and reported fracture toughness between 3.0 and 3.9 MPa m$^{1/2}$. Fracture toughness of free sintered Al_2O_3 ceramics was measured between 3.5 and 6.5 MPa m$^{1/2}$ for samples with a grain size of 0.2–60 μm.[134,135] The variation may depend on grain shape and processing conditions.[134,135] Yao and co-workers observed grain size independent fracture toughness of 3.4 MPa m$^{1/2}$ in vacuum-sintered Al_2O_3 with a grain size of 0.3–3 μm.[119] In all cases, Al_2O_3 is more mechanically robust and thermally conductive than YAG and sesquioxides.

Table 1.3 Selected thermal and mechanical properties of Al_2O_3 single crystals and polycrystalline ceramics. See also **Figure 1.6**.

	Al_2O_3 SC	Al_2O_3 ceramic	Grain size	Preparation method	Reference
Fracture toughness K_{IC} (MPa m$^{1/2}$)		3.0-3.9	6.2-60.1 μm	Hot press with HIP	Tani et al. [154]
		3.5-6.5	1-60 μm	Free sintering	T. Koyama et al. [134]
		4.6-5.6	0.2-41.2 μm	Free sintering	K. Maiti, A. Sil [135]
		3.26-3.57	0.3-3 μm	Vacuum sintering	W. Yao et al. [119]
Thermal conductivity, k (Wm^{-1}K^{-1})	18.5 (523K)	16.6(550K)	9-17 μm		F. Charvat, W. Kingery [155]
	33 (305K)				St. Burghartz, B. Schulz [131]
		25.9-32.8	1.5-20 μm	Free sintering	D. Smith et al. [133]
		15.3-12.5(99%-92% dense, 300K)			Z. Xie et al. [132]
		30 (300K)	250 nm	CAPAD	E. Penilla et al. [44]

3. Fluorapatite

Fluorapatite (FAP) is a naturally existing phosphate mineral with chemical formula $Ca_5(PO_4)_3F$ and hexagonal structural symmetry. Artificially grown fluorapatite was demonstrated as the laser host material early in the 1960s,[136] but it was not until the 1990s that it attracted more attention with the technological advances in laser diodes as the pumping source.[24,137] In the work of Zhang *et al.*, single-crystal Nd^{3+}:FAP was grown and exhibited excellent lasing parameters including low optical loss, high absorption/emission cross sections, and low lasing threshold.[137] In the same year, Payne and co-workers demonstrated lab-grown Yb^{3+}:FAP single crystal that has high emission and absorption cross sections as well as high slope efficiency.[24]

As a laser host material, fluorapatite does not have the best thermal and mechanical properties compared to other crystalline hosts. Faure and co-workers grew FAP single crystals using the Czochralski technique and measured the optical and thermal properties.[26] They showed that $Ca_5(PO_4)_3F$ single crystals have a thermal conductivity of 2–2.4 $Wm^{-1}\,K^{-1}$ depending on the crystallographic orientation. The birefringence Δn was 0.003. This result is comparable to Payne and co-workers' measurement on Yb:FAP, where they measured a thermal conductivity of 1.9–2.1 $Wm^{-1}\,K^{-1}$ and a Δn of 0.002.[24] Payne *et al.* also reported the fracture toughness K_{1C} of the Yb:FAP single crystal to be 0.48 MPa $m^{1/2}$. The thermal conductivity and mechanical toughness of fluorapatite are significantly lower than that of YAG, making it a less viable option for high power applications.

Despite the inferior thermal and mechanical properties of fluorapatite, it has attracted growing research attention in the past decade. With its hexagonal structure and a smaller Δn than Al_2O_3, FAP is a perfect material to demonstrate highly transparent ceramics from an optically anisotropic material by controlling the orientation or the size of the grains in the ceramic. In 2010, Akiyama, Sato, and Taira fabricated highly transparent Nd:FAP and Yb:FAP ceramics by magnetic alignment with subsequent free sintering followed by hot isostatic pressing.[138] In the next year, they successfully demonstrated lasing using the Nd:FAP ceramic.[139] In 2014, the same group demonstrated a laser experiment with the Yb:FAP ceramic they fabricated using the same approach.[140]

In 2019, Furuse, Horiuchi, and Kim fabricated highly transparent Nd:FAP laser ceramic through CAPAD without any grain alignment step.[141] With a grain size as small as 140 nm, they were able to achieve a remarkable loss coefficient of 0.18 cm^{-1} at 1.06 μm. This work from Furuse *et al*. marks the first verification of lasing in randomly oriented ceramics made from optically anisotropic materials. The experimental verification of lasing in a non-cubic ceramic opens the possibility to other non-cubic materials that unlike FAP have great thermal and mechanical potential.

4. Aluminum nitride

Aluminum nitride (AlN) has long been known for its remarkably high thermal conductivity around 285 $\mathrm{Wm}^{-1}\,\mathrm{K}^{-1}$,[12] which is close to some of the most conductive metals such as silver and copper (~400 $\mathrm{Wm}^{-1}\,\mathrm{K}^{-1}$), and 1–2 orders of magnitude higher than the oxide/fluoride-based materials discussed above. Besides the impressive thermal conductivity, AlN is suitable for optical applications such as lighting and lasing because of its wide bandgap of 6.2 eV.[142] Given the bandgap and lattice phonon energy, the AlN single crystal allows light transmission over a wide optical range from 200 nm to 6 μm in wavelength, making it a promising material for window and lighting applications.

Photoluminescence, stimulated emission, and lasing in transition metal-doped AlN have also been reported recently.[5,6] But these works were based on AlN powders, AlN thin films, and AlN microfibers, which are not readily amenable for scaling up or high-energy applications. AlN also suffers from the similar challenges as Al_2O_3 that rare earth incorporation into the AlN lattice can be especially difficult because of the low equilibrium solubility of relatively large rare earth ions in the AlN lattice. Ishikawa *et al*. reported the synthesis of Ce-doped AlN single crystals, but the dopant concentration was relatively low (<0.1 at. %).[143]

Like the polycrystalline Al_2O_3 case, polycrystalline AlN ceramics have been widely studied as an alternative to single crystals. High thermal conductivity AlN ceramics have been obtained by Watari, Nakano, and co-workers.[57,144] The effect of Y_2O_3 additive for AlN ceramic sintering has been thoroughly discussed in order to improve the ceramic thermal conductivity.[57,145,146] Moreover, there is recent work on AlN for light emitting applications; incorporation of Ce, Nd, Tb, and Er into AlN ceramics has been achieved and photoluminescence studies presented.[3,4,48,147] Note that these studies report emission characteristic of RE^{3+} ions that are typically used in lasing. Similar to the polycrystalline Al_2O_3 ceramics discussed in **Sec. 1.3.2.2**, polycrystalline AlN ceramics showed potential for higher RE doping concentration. Wieg and co-workers demonstrated that it is possible to incorporate higher RE concentration into polycrystalline AlN ceramics compared to single crystals and the RE segregation at the grain boundaries can be minimized with proper dopant and host powder processing.[47,48]

Figure 1.7 shows selected temperature-dependent thermal conductivity results for AlN single crystals and polycrystalline ceramics. Slack measured 285 $Wm^{-1} K^{-1}$ at room temperature and above 2000 $Wm^{-1} K^{-1}$ near 40 K for a AlN single crystal and estimated an astonishing 60 000 $Wm^{-1} K^{-1}$ peak value near 30 K for hypothetically "pure" AlN with no oxygen impurity.[12] Watari and co-workers free sintered an AlN ceramic with a grain size of 8 μm and measured room temperature thermal conductivity of 272 $Wm^{-1} K^{-1}$.[57] However, the low-temperature thermal conductivity was significantly lower than that of a single crystal because of the point defect and grain boundary scattering of phonons. Wieg *et al*. fabricated 0.5 at. % Tb:AlN with a grain size of 4.3 μm through CAPAD and measured 94 $Wm^{-1} K^{-1}$ at room temperature.[47] The high thermal conductivity despite phonon scattering from grain boundaries and dopant atoms indicates the great potential of AlN ceramics for lighting and lasing applications.

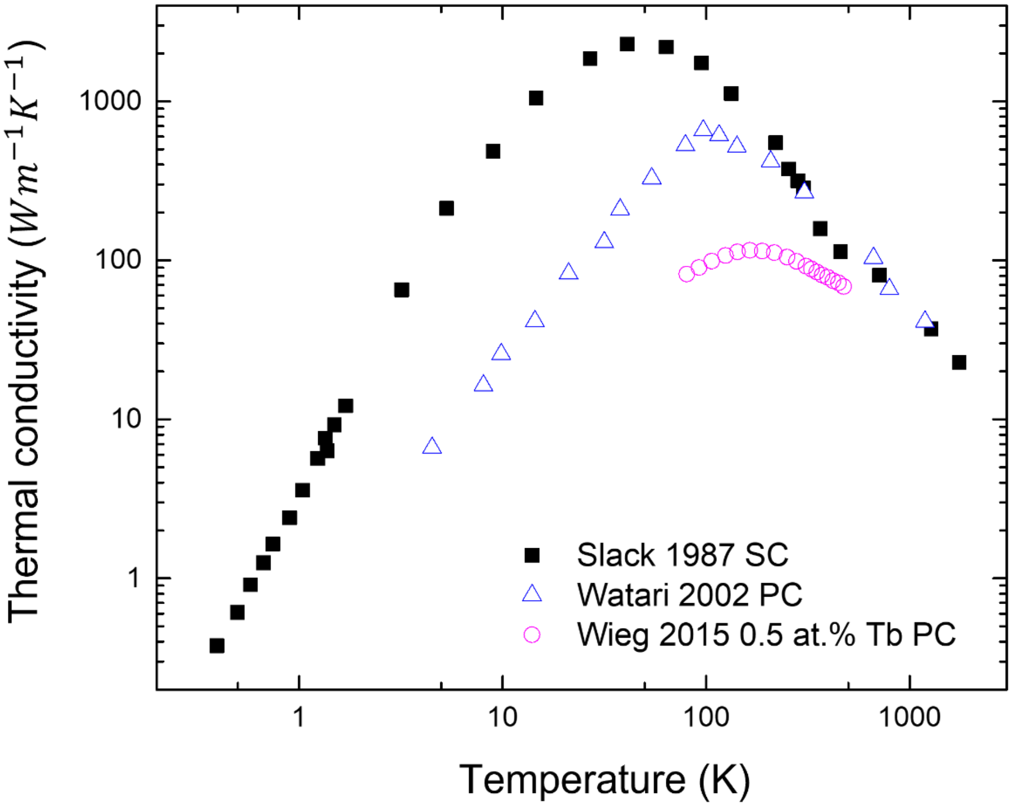

Figure 1.7 Temperature-dependent thermal conductivity of AlN. For doped samples, the doping species and concentration are specified in the legend. SC and PC, respectively, denote single crystal and polycrystalline AlN. Data from Refs. 12, 47, and 57.

Besides the excellent thermal conductivity, AlN also exhibits good mechanical properties. **Table 1.4** shows more thermal/mechanical measurements on AlN single crystals and polycrystalline ceramics. Yonenaga *et al*. reported the fracture toughness of single-crystal AlN as $K_{1C} = 0.5$ MPa $m^{1/2}$,[148] which is lower than that of YAG and Al_2O_3. However, more mechanical testing on free sintered polycrystalline AlN ceramics has been done and measured fracture toughness values were reported between 2.9 and 3.3 MPa $m^{1/2}$ (Refs. 146, 149, and 150) with varying sintering additives. Wieg and co-workers reported fracture toughness between 4.2 and 5.0 MPa$m^{1/2}$ for AlN ceramics densified using CAPAD with different Tb doping concentrations.[47] The high thermal conductivity combined with high fracture toughness of AlN ceramic gives it a thermal shock resistance R_s as high as $52000 \mathrm{Wm}^{-1}$, which is more than 60 times higher than that of Nd:YAG single crystals.[47]

Table 1.4 Selected thermal and mechanical properties of AlN single crystals and polycrystalline ceramics.

	AlN SC	AlN ceramic	Grain size	Preparation method	Reference
Fracture toughness K_{IC} (MPa $m^{1/2}$)	0.5 <0001>				Ichiro Yonenaga et al. [148]
		2.9-3.1 (5 wt% REO)	3.3-4.4 μm	Free sintering	R. Terao et al. [149]
		2.7-3.3		Vacuum hot press	Q. Li et al. [150]
		2.9-3.2	2.1-7.6 μm	Free sintering	T. Kusunose, T. Sekino [146]
Thermal conductivity, k ($Wm^{-1}K^{-1}$)	285 (300K)				G. Slack et al. [12]
		200-267 (300K)	5-8 μm	Free sintering	K. Watari et al. [57]
		61-99 (0-0.5 at.% Tb:AlN, 278K)	2.6-4.7 μm	CAPAD	A. Wieg et al. [47]
		134-168		Vacuum hot press	Q. Li et al. [150]
		136-180 (300K)	2.1-7.6 μm	Free sintering	T. Kusunose, T. Sekino [146]

1.4 Opportunities for higher thermal conductivity laser gain media

Single crystal and glass-based gain media have been the unrivaled standards for high-power solid-state lasers for decades. However, the flexibility offered by polycrystalline ceramics makes them ever more promising alternatives especially for high-power applications. Recognized advantages of ceramics include improved fracture toughness and flexibility in manufacturing. Less discussed are the enticing possibilities of intentionally designed gradient doping that could lead to more optimized thermal profiles.

As discussed in **Secs. 1.2.1** and **1.2.1**, one of the grand challenges in developing high-power laser media from polycrystalline ceramics is the competing thermal and optical effects. Al_2O_3 and AlN have excellent thermal conductivity, but the birefringent nature of the two materials requires small grain size (usually sub-μm) to achieve good optical transparency. However, smaller grain sizes reduce Λ_{gb}, therefore impairs the thermal conductivity of the material. To address this issue, anisotropic microstructure has been proposed[59] with one example shown in **Figure 1.8**. In this proposed laser design, the gain medium is in direct contact with two heat sinks. The large contact area between gain media and heat sinks allows for efficient heat dissipation and high overall laser power. The lasing axis and pumping axis have nanometric grain size which allows low birefringent scattering loss for lasing and pumping light, while the cooling axis has micrometer grain size which grants good thermal conductivity.

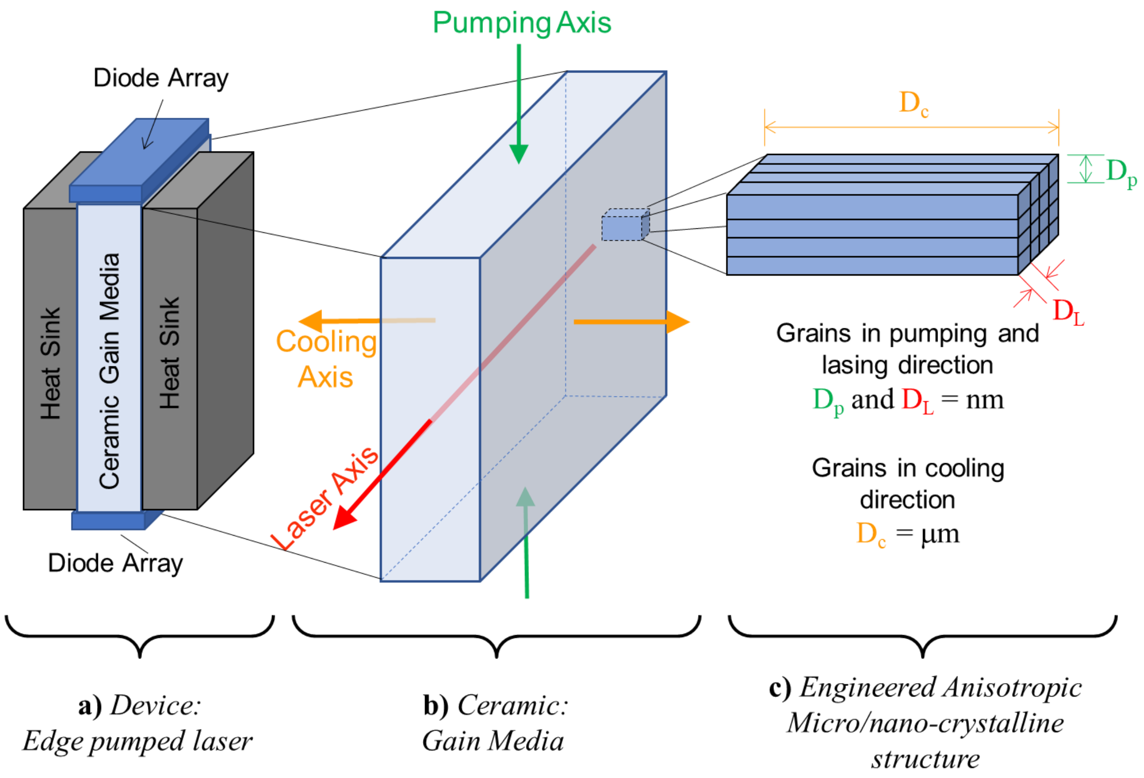

a) *Device: Edge pumped laser*

b) *Ceramic: Gain Media*

c) *Engineered Anisotropic Micro/nano-crystalline structure*

Figure 1.8 a) Schematic showing the integration of polycrystalline ceramic gain media into a diode pumped laser design **b)** Three axes for pumping, lasing, and cooling **c)** The ceramics have micrometer sizes in the cooling direction but nanometer sizes in the optical directions (both pumping and lasing), in order to provide both high thermal conductivity (minimal phonon scattering) and excellent beam quality (minimal birefringence scattering).

In a theoretical study, Mishra *et al.*[59] proposed to use anisotropic microstructured materials and investigated the possibility that thermal transport and light transmission could occur in independent directions from each other. Specifically, the authors explored these concepts by modeling 1 at. % Ti-doped polycrystalline AlN and Al_2O_3, with the anisotropic microstructures having two principal axes as shown in **Figure 1.8**. Considering the optical birefringent scattering discussed in **Sec. 1.2.1** and phonon scattering mechanisms discussed in **Sec. 1.2.2**, the authors calculated the thermal conductivity and light extinction coefficient (loss coefficient) along the proposed directions in this anisotropic microstructure. It was shown that the high intrinsic thermal conductivities of Al_2O_3 and AlN fundamentally improve the thermomechanical properties of laser gain media with the proposed anisotropic microstructure.

Comparison of the materials reviewed in **Sec. 1.3** show only modest improvements of thermal conductivity compared to YAG for optically isotropic ceramics (See **Figs. 1.1** and **1.4** and **Table 1.2**). However, the anisotropic materials, alumina and AlN, can have significant thermomechanical benefits. Despite the complications introduced by birefringence, the tremendous thermomechanical advantage, directly translating to increased power, of alumina and AlN makes them very promising for high-power applications. It is possible that with the concepts of leveraging judiciously designed anisotropic microstructures, high thermal conductivity of alumina and AlN could pave the way for promising materials to be used in future high-powered lasers.

1.5 Chapter 1 Summary and Conclusion

The effects of microstructure on transparency and thermal conductivity of polycrystalline ceramics were discussed to explore future laser gain materials with superior pumping capability. The thermal conductivity and fracture toughness of the most promising crystalline material candidates were reviewed. Since cubic laser materials such as YAG and sesquioxides exhibit limited thermal conductivity, the use of non-cubic materials with intrinsically much higher thermal conductivity and outstanding mechanical toughness, such as Al_2O_3 and AlN, can be a key to future high-power lasers. To achieve high optical transparency as well as high thermal conductivity, the microstructure with aligned high aspect ratio grains (rods or disks) can be especially beneficial. Meanwhile, the fracture toughness enhancement demonstrated by polycrystalline ceramics compared to single crystals could be especially beneficial for increasing laser power since thermal shock is the ultimate failure caused by over pumping of gain media.

In this dissertation, fabrication and characterization of the most transparent rare earth doped polycrystalline Al_2O_3 / the first thulium doped Al_2O_3 ceramic and the most transparent AlN polycrystalline ceramic as well as the first thulium doped AlN ceramic will be presented. The utilization of these two high thermal conductivity material and achievement of high optical transparency may lead to better laser gain media in the future.

Chapter 1, in part, is co-authored with L. Tang, Dr. C. L. Hardin, Dr. C. Dames, Dr. Y. Kodera and Dr. J. E. Garay, and is published in Journal of Applied Physics 2022, 131, 020902. The dissertation author was the primary investigator and author of this paper.

1.6 Chapter 1 References

1 T. H. Maiman, Nature 187, 493–494 (1960).

2 W. Koechner, Solid-State Laser Engineering, 6th ed. (Springer, 2014).

3 A. T. Wieg, M. J. Grossnickle, Y. Kodera, N. M. Gabor, and J. E. Garay, Appl. Phys. Lett. 109, 121901 (2016).

4 L. D. Merkle, A. C. Sutorik, T. Sanamyan, L. K. Hussey, G. Gilde, C. Cooper, and M. Dubinskii, Opt. Mater. Express 2, 78 (2012).

5 M. Maqbool, K. Main, and M. Kordesch, Opt. Lett. 35, 3637 (2010).

6 L. Jiang, S. Jin, W. Wang, S. Zuo, Z. Li, S. Wang, K. Zhu, Z. Wei, and X. Chen, Sci. Rep. 5, 17979 (2016).

7 S. C. Rand and L. G. DeShazer, Opt. Lett. 10, 481 (1985).

8 L. Mezeix and D. J. Green, Int. J. Appl. Ceram. Technol. 3, 166–176 (2006).

9 P. Klein and W. Croft, J. Appl. Phys. 38, 1603 (1967).

10 J. F. Shackelford, Y.-H. Han, S. Kim, and S.-H. Kwon, CRC Materials Science and Engineering Handbook (CRC Press, 2001).

11 R. W. Powell, C. Y. Ho, and P. E. Liley, Thermal Conductivity of Selected Materials, Part 2 (National Bureau of Standards, 1966).

12 G. A. Slack, R. A. Tanzilli, R. O. Pohl, and J. W. Vandersande, J. Phys. Chem. Solids 48, 641–647 (1987).

13 F. Dahmani, J. C. Lambropoulos, A. W. Schmid, S. J. Burns, and C. Pratt, J. Mater. Sci. 33, 4677–4685 (1998).

14 P. Combis, P. Cormont, L. Gallais, D. Hebert, L. Robin, and J.-L. Rullier, Appl. Phys. Lett. 101, 211908 (2012).

15 G. A. Slack, Phys. Rev. 126, 427–441 (1962).

16 O. Yeheskel, I. C. Albayrak, B. Anasori, and M. W. Barsoum, J. Eur. Ceram. Soc. 31, 1703–1712 (2011).

17 V. Peters, A. Bolz, K. Petermann, and G. Huber, J. Cryst. Growth 237–239, 879–883 (2002).

18 I. C. Albayrak, S. Basu, A. Sakulich, O. Yeheskel, and M. W. Barsoum, J. Am. Ceram. Soc. 93, 2028 (2010).

19 A. A. Kaminskii, M. S. Akchurin, P. Becker, K. Ueda, L. Bohatý, A. Shirakawa, M. Tokurakawa, K. Takaichi, H. Yagi, J. Dong, and T. Yanagitani, Laser Phys. Lett. 5, 300–303 (2008).

20 M. S. Akchurin, T. T. Basiev, A. A. Demidenko, M. E. Doroshenko, P. P. Fedorov, E. A. Garibin, P. E. Gusev, S. V. Kuznetsov, M. A. Krutov, I. A. Mironov, V. V. Osiko, and P. A. Popov, Opt. Mater. 35, 444–450 (2013).

21 P. A. Popov, K. V. Dukel’skiĭ, I. A. Mironov, A. N. Smirnov, P. L. Smolyanskiĭ, P. P. Fedorov, V. V. Osiko, and T. T. Basiev, Dokl. Phys. 52, 7–9 (2007).

22 Z. Ma, D. Li, J. Gao, N. Wu, and K. Du, Opt. Commun. 275, 179–185 (2007).

23 Y. Sato and T. Taira, in Optics InfoBase Conference Paper (Optical Society of America, 2007), p. 42.

24 S. A. Payne, L. K. Smith, L. D. Deloach, W. L. Kway, J. B. Tassano, and W. F. Krupke, IEEE J. Quantum Electron. 30, 170–179 (1994).

25 T. Pollak, W. Wing, R. Grasso, E. Chicklis, and H. Jenssen, IEEE J. Quantum Electron. 18, 159–163 (1982).

26 N. Faure, C. Borel, R. Templier, M. Couchaud, C. Calvat, and C. Wyon, Opt. Mater. 6, 293–303 (1996).

27 A. Ikesue and Y. L. Aung, Nat. Photonics 2, 721–727 (2008).

28 J. Li, Y. Wu, Y. Pan, W. Liu, L. Huang, and J. Guo, Opt. Mater. 31, 6–17 (2008).

29 A. Ikesue, T. Kinoshita, K. Kamata, and K. Yoshida, J. Am. Ceram. Soc. 78, 1033–1040 (1995).

30 A. Ikesue and Y. L. Aung, J. Eur. Ceram. Soc. 40, 2432–2438 (2020).

31 J. Li, Y. Pan, Y. Zeng, W. Liu, B. Jiang, and J. Guo, Int. J. Refract. Met. Hard Mater. 39, 44–52 (2013).

32 C. Kränkel, IEEE J. Sel. Top. Quantum Electron. 21, 250–262 (2015).

33 C. Nie, S. Bera, and J. Harrington, Advanced Photonics 2016, OSA Technical Digest (online), paper SoM3G.2 (2016).

34 R. K. Nubling and J. A. Harrington, Appl. Opt. 36, 5934 (1997).

35 G. Witz, V. Shklover, W. Streurer, S. Bachegowda, and H.-P. Bossmann, J. Am. Ceram. Soc. 90, 2935–2940 (2007).

36 K. Matsui, H. Horikoshi, N. Ohmichi, M. Ohgai, H. Yoshida, and Y. Ikuhara, J. Am. Ceram. Soc. 86, 1401–1408 (2003).

37 S. Dillon and M. Harmer, Acta Mater. 55, 5247–5254 (2007).

38 A. Krell, J. Klimke, and T. Hutzler, J. Eur. Ceram. Soc. 29, 275–281 (2009).

39 L. Zhang and W. Pan, J. Am. Ceram. Soc. 98, 3326–3331 (2015).

40 R. Coble, U.S. patent 3,026,210A (March 20, 1962).

41 M. Shachar, G. Uahengo, E. H. Penilla, Y. Kodera, and J. E. Garay, J. Appl. Phys. 128, 083103 (2020).

42 R. Apetz and M. P. B. van Bruggen, J. Am. Ceram. Soc. 86, 480–486 (2003).

43 T. Sanamyan, R. Pavlacka, G. Gilde, and M. Dubinskii, Opt. Mater. 35, 821–826 (2013).

44 E. H. Penilla, Y. Kodera, and J. E. Garay, Adv. Funct. Mater. 23, 6036–6043 (2013).

45 E. H. Penilla, C. L. Hardin, Y. Kodera, S. A. Basun, D. R. Evans, and J. E. Garay, J. Appl. Phys. 119, 023106 (2016).

46 E. H. Penilla, L. F. Devia-Cruz, M. A. Duarte, C. L. Hardin, Y. Kodera, and J. E. Garay, Light Sci. Appl. 7 (2018).

47 A. T. Wieg, Y. Kodera, Z. Wang, C. Dames, and J. E. Garay, Acta Mater. 86, 148–156 (2015).

48 A. T. Wieg, Y. Kodera, Z. Wang, T. Imai, C. Dames, and J. E. Garay, Appl. Phys. Lett. 101, 111903 (2012).

49 E. S. Toberer, L. L. Baranowski, and C. Dames, Annu. Rev. Mater. Res. 42, 179–209 (2012).

50 G. Chen, Nanoscale Energy Transport and Conversion a Parallel Treatment of Electrons, Molecules, Phonons, and Photons (Oxford University Press, 2005).

51 H. Yagi, T. Yanagitani, T. Numazawa, and K. Ueda, Ceram. Int. 33, 711–714 (2007).

52 G. P. Srivastava, “Lattice thermal conduction mechanism in solids,” in High Thermal Conductivity Materials (Springer, New York, 2006), pp. 1–35.

53 Purdue University, Thermophysical Properties Research Center (TPRC), in Thermophysical Properties of Matter, edited by Y. S. Touloukian (IFI/Plenum, New York, 1970).

54 J. M. Ziman, Electrons and Phonons: The Theory of Transport Phenomena in Solids (Oxford University Press, 2001).

55 Z. M. Zhang, Z. M. Zhang, and Luby, Nano/Microscale Heat Transfer (McGraw-Hill, New York, 2007), Vol. 410.

56 Z. Wang, J. E. Alaniz, W. Jang, J. E. Garay, and C. Dames, Nano Lett. 11, 2206–2213 (2011).

57 K. Watari, H. Nakano, K. Urabe, K. Ishizaki, S. Cao, and K. Mori, J. Mater. Res. 17, 2940–2944 (2002).

58 Y. Sato, J. Akiyama, and T. Taira, Opt. Mater. 31, 720–724 (2009).

59 V. Mishra, J. E. Garay, and C. Dames, Adv. Theory Simul. 3, 2000036 (2020).

60 X. Xu, Z. Zhao, J. Xu, and P. Deng, Solid State Commun. 130, 529–532 (2004).

61 A. Ikesue, Y. L. Aung, T. Taira, T. Kamimura, K. Yoshida, and G. L. Messing, Annu. Rev. Mater. Res. 36, 397–429 (2006).

62 I. Shoji, S. Kurimura, Y. Sato, T. Taira, A. Ikesue, and K. Yoshida, Appl. Phys. Lett. 77, 939 (2000).

63 J. Sanghera, W. Kim, G. Villalobos, B. Shaw, C. Baker, J. Frantz, B. Sadowski, and I. Aggarwal, Materials. 5, 258–277 (2012).

64 A. A. Kaminskiĭ, M. S. Akchurin, V. I. Alshits, K. Ueda, K. Takaichi, J. Lu, T. Uematsu, M. Musha, A. Shirikawa, V. Gabler, H. J. Eichler, H. Yagi, T. Yanagitani, S. N. Bagayev, J. Fernandez, and R. Balda, Crystallogr. Rep. 48, 515–519 (2003).

65 M. Sokol, S. Kalabukhov, V. Kasiyan, M. P. Dariel, and N. Frage, J. Am. Ceram. Soc. 99, 802–807 (2016).

66 J. Lu, M. Prabhu, J. Song, C. Li, J. Xu, K. Ueda, A. A. Kaminskii, H. Yagi, and T. Yanagitani, Appl. Phys. B: Lasers Opt. 71, 469–473 (2000).

67 A. Ikesue, Opt. Mater. 19, 183–187 (2002).

68 R. M. Yamamoto, B. S. Bhachu, K. P. Cutter, S. N. Fochs, S. A. Letts, C. W. Parks, M. D. Rotter, and T. F. Soules, Lawrence Livermore National Lab Report No. 352959, 2008.

69 B. Bishop, "Northrop Grumman scales new heights in electric laser power, achieves 100 kW from a solid-state laser" (Globe Newswire, 2009). See https:// news.northropgrumman.com/news/releases/photo-release-northrop-grummanscales-new-heights-in-electric-laser-power-achieves-100-kilowatts-from-a-solidstate-laser (Accessed Jan. 3 2022).

70 J. E. Garay, Annu. Rev. Mater. Res. 40, 445–468 (2010).

71 K. Petermann, G. Huber, L. Fornasiero, S. Kuch, E. Mix, V. Peters, and S. A. Basun, J. Lumin. 87–89, 973–975 (2000).

72 J. Sanghera, W. Kim, G. Villalobos, B. Shaw, C. Baker, J. Frantz, B. Sadowski, and I. Aggarwal, Opt. Mater. 35, 693–699 (2013).

73 L. Fornasiero, E. Mix, V. Peters, K. Petermann, and G. Huber, Cryst. Res. Technol. 34, 255–260 (1999).

74 L. Fornasiero, E. Mix, V. Peters, E. Heumann, K. Petermann, and G. Huber, in OSA TOPS Vol. 26 Advanced Solid-State Lasers (Optical Society of America, 1999), Vol. 249.

75 L. Fornasiero, N. Berner, E. Mix, V. Peters, K. Petermann, and G. Huber, in OSA TOPS Vol. 26 Advanced Solid-State Lasers (Optical Society of America, 1999), Vol. 26, p. 450.

76 L. Fornasiero, E. Mix, V. Peters, K. Petermann, and G. Huber, Ceram. Int. 26, 589–592 (2000).

77 J.-G. Li, T. Ikegami, and T. Mori, J. Am. Ceram. Soc. 88, 817–821 (2005).

78 B. Le Garrec, V. Cardinali, and G. Bourdet, in High-Power, High-Energy, High-Intensity Laser Technology. Research Using Extreme Light Entering New Frontiers with Petawatt-Class Lasers (Proceedings of SPIE, 2013), p. 87800E.

79 D. Rand, D. Miller, D. J. Ripin, and T. Y. Fan, Opt. Mater. Express 1, 434 (2011).

80 G. Gogotsi, Adv. Sci. Technol. 45, 95–100 (2006).

81 A. Diening, B. M. Dicks, E. Heumann, J. P. Meyn, K. Petermann, and G. Huber, in OSA Trends in Optics and Photonics, Vol. 10, Advanced Solid-State Lasers, edited by C. R. Pollock and W. R. Bosenberg (Optical Society of America, 1997), p. 194.

82 E. Mix, L. Fornasiero, A. Diening, K. Petermann, and G. Huber, Advanced Solid-State Lasers, Technical Digest (Optical Society of America, 1998).

83 J. H. Mun, A. Jouini, A. Novoselov, A. Yoshikawa, T. Kasamoto, H. Ohta, H. Shibata, M. Isshiki, Y. Waseda, G. Boulon, and T. Fukuda, Jpn. J. Appl. Phys. 45, 5885–5888 (2006).

84 T. Y. Fan, S. Member, D. J. Ripin, R. L. Aggarwal, J. R. Ochoa, B. Chann, M. Tilleman, and J. Spitzberg, IEEE J. Sel. Top. Quantum Electron. 13, 448–459 (2007).

85 A. A. Kaminski□ı, M. S. Akchurin, R. V. Ga□ınutdinov, K. Takaichi, A. Shirakava, H. Yagi, T. Yanagitani, and K. Ueda, Crystallogr. Rep. 50, 869–873 (2005).

86 E. Mix, Doctoral dissertation (Fachbereich Physik der Universität Hamburg, 1999).

87 M. Guzik, J. Pejchal, A. Yoshikawa, A. Ito, T. Goto, M. Siczek, T. Lis, and G. Boulon, Cryst. Growth Des. 14, 3327–3334 (2014).

88 A. Fukabori, V. Chani, K. Kamada, F. Moretti, and A. Yoshikawa, Cryst. Growth Des. 11, 2404–2411 (2011).

89 C. Mcmillen, D. Thompson, T. Tritt, and J. Kolis, Cryst. Growth Des. 11, 4386–4391 (2011).

90 R. Peters, C. Kränkel, K. Petermann, and G. Huber, J. Cryst. Growth 310, 1934–1938 (2008).

91 S. E. Hatch, W. F. Parsons, and R. J. Weagley, Appl. Phys. Lett. 5, 153–154 (1964).

92 P. Camy, J. L. Doualan, S. Renard, A. Braud, V. Ménard, and R. Moncorgé, Opt. Commun. 236, 395–402 (2004).

93 C. Zhang, J. Liu, X. Fan, Q. Peng, X. Guo, D. Jiang, X. Qian, and L. Su, Opt. Laser Technol. 103, 89–92 (2018).

94 J. Du, X. Liang, Y. Wang, L. Su, W. Feng, E. Dai, Z. Xu, and J. Xu, Opt. Express 13, 7970 (2005).

95 L. B. Su, Q. G. Wang, H. J. Li, G. Brasse, P. Camy, J. L. Doualan, A. Braud, R. Moncorgé, Y. Y. Zhan, L. H. Zheng, X. B. Qian, and J. Xu, Laser Phys. Lett. 10, 035804 (2013).

96 Z. P. Qin, G. Q. Xie, J. Ma, W. Y. Ge, P. Yuan, L. J. Qian, L. B. Su, D. P. Jiang, F. K. Ma, Q. Zhang, Y. X. Cao, and J. Xu, Opt. Lett. 39, 1737 (2014).

97 C. Li, M. Fan, J. Liu, L. Su, D. Jiang, X. Qian, and J. Xu, Opt. Laser Technol. 69, 140–143 (2015).

98 J. Liu, X. Fan, J. Liu, W. Ma, W. Jingya, and L. Su, Opt. Lett. 41, 4660 (2016).

99 G. Lu, B. Mei, J. Song, W. Li, and R. Xing, Mater. Lett. 115, 162–164 (2014).

100 Z. Sun, B. Mei, W. Li, X. Liu, and L. Su, Opt. Mater. 71, 35–40 (2017).

101 J. Sarthou, P. Aballéa, G. Patriarche, H. Serier-Brault, A. Suganuma, P. Gredin, and M. Mortier, J. Am. Ceram. Soc. 99, 1992–2000 (2016).

102 W. Li, H. Huang, B. Mei, C. Wang, J. Liu, S. Wang, D. Jiang, and L. Su, Ceram. Int. 46, 19530–19536 (2020).

103 Z. Liu, B. Mei, J. Song, and W. Li, J. Eur. Ceram. Soc. 34, 4389–4394 (2014).

104 Z. Liu, B. Mei, J. Song, D. Yuan, and Z. Wang, J. Alloys Compd. 646, 760–765 (2015).

105 Y. Yang, W. Li, B. Mei, J. Song, G. Yi, Z. Zhou, and J. Liu, J. Lumin. 213, 504–509 (2019).

106 A. A. Lyapin, P. P. Fedorov, E. A. Garibin, A. V. Malov, V. V. Osiko, P. A. Ryabochkina, and S. N. Ushakov, Opt. Mater. 35, 1859–1864 (2013).

107 W. Li, H. Huang, B. Mei, J. Song, G. Yi, and X. Guo, Mater. Lett. 207, 37–40 (2017).

108 F. Xiong, J. Song, W. Li, B. Mei, and L. Su, Mater. Res. Bull. 95, 138–145 (2017).

109 J. Sarthou, J.-Y. Duquesne, L. Becerra, P. Gredin, and M. Mortier, J. Appl. Phys. 121, 245108 (2017).

110 J. R. O'Connor, Appl. Phys. Lett. 9, 407–409 (1966).

111 A. W. Tucker, M. Birnbaum, C. L. Fincher, and J. W. Erler, J. Appl. Phys. 48, 4907–4911 (1977).

112 R. A. Fields, M. Birnbaum, and C. L. Fincher, Appl. Phys. Lett 1885, 4 (1987).

113 Y. Sato and T. Taira, Opt. Express 14, 10528 (2006).

114 Y.-F. Chen and H.-J. Kuo, Opt. Lett. 23, 846 (1998).

115 J. Morikawa, C. Leong, T. Hashimoto, T. Ogawa, Y. Urata, S. Wada, M. Higuchi, and J. Takahashi, J. Appl. Phys. 103, 063522 (2008).

116 A. Ahmadi, A. Avazpour, H. Nadgaran, and M. Mousavi, Laser Phys. 28, 105002 (2018).

117 J. A. Salem, C. C. He, N. W. Sawruk, and V. Litvinovich, J. Eur. Ceram. Soc. 40, 4939–4948 (2020).

118 P. W. Roth, D. Burns, and A. J. Kemp, Opt. Express 20, 20629 (2012).

119 W. Yao, J. Liu, T. B. Holland, L. Huang, Y. Xiong, J. M. Schoenung, and A. K. Mukherjee, Scr. Mater. 65, 143–146 (2011).

120 P. Moulton, Opt. News 8, 9 (1982).

121 P. F. Moulton, J. Opt. Soc. Am. B 3, 125 (1986).

122 M. D. Chambers and D. R. Clarke, Annu. Rev. Mater. Res. 39, 325–359 (2009).

123 G. R. Williams, S. B. Bayram, S. C. Rand, T. Hinklin, and R. M. Laine, Phys. Rev. A 65, 013807 (2001).

124 B. Li, G. Williams, S. C. Rand, T. Hinklin, and R. M. Laine, Opt. Lett. 27, 394 (2002).

125 Q. Song, C.-R. Li, J.-Y. Li, W.-Y. Ding, S.-F. Li, J. Xu, X.-L. Deng, and C.-L. Song, Opt. Mater. 28, 1344–1349 (2006).

126 B. Zhou, Z. Xiao, A. Huang, L. Yan, F. Zhu, J. Wang, P. Yin, and H. Wang, Prog. Nat. Sci. 18, 661–664 (2008).

127 R. Serna, S. Nuñez-Sanchez, F. Xu, and C. N. Afonso, Appl. Surf. Sci. 257, 5204–5207 (2011).

128 S. H. Waeselmann, S. Heinrich, C. Krankel, and G. Huber, in Advanced Solid State Lasers Conference (Optical Society of America, 2015).

129 S. H. Waeselmann, S. Heinrich, C. Kränkel, and G. Huber, Laser Photonics Rev. 10, 510–516 (2016).

130 S. H. Waeselmann, C. E. Ruter, D. Kip, C. Kränkel, and G. Huber, Opt. Mater. Express 7, 2361 (2017).

131 S. Burghartz and B. Schulz, J. Nucl. Mater. 212–215, 1065–1068 (1994).

132 Z. Xie, W. Xue, H. Chen, and Y. Huang, Ceram. Int. 37, 2165–2168 (2011).

133 D. S. Smith, S. Fayette, S. Grandjean, C. Martin, R. Telle, and T. Tonnessen, J. Am. Ceram. Soc. 86, 105–111 (2003).

134 T. Koyama, A. Nishiyama, and K. Niihara, J. Mater. Sci. 29, 3949–3954 (1994).

135 K. Maiti and A. Sil, Ceram. Int. 36, 2337–2344 (2010).

136 R. C. Ohlmann, K. B. Steinbruegge, and R. Mazelsky, Appl. Opt. 7, 905 (1968).

137 X. X. Zhang, G. B. Loutts, M. Bass, and B. H. T. Chai, Appl. Phys. Lett. 64, 10–12 (1994).

138 J. Akiyama, Y. Sato, and T. Taira, Opt. Lett. 35, 3598 (2010).

139 J. Akiyama, Y. Sato, and T. Taira, Appl. Phys. Express 4, 022703 (2011).

140 Y. Sato, J. Akiyama, and T. Taira, in Proceedings 2015 European Conference on Lasers Electro-Optics—European Quantum Electronics Conference CLEO/Europe-EQEC 2015 (Optical Society of America, 2015), p. 22703, 1050.

141 H. Furuse, N. Horiuchi, and B. Kim, Sci. Rep. 9, 10300 (2019).

142 W. M. Yim, E. J. Stofko, P. J. Zanzucchi, J. I. Pankove, M. Ettenberg, and S. L. Gilbert, J. Appl. Phys. 44, 292–296 (1973).

143 R. Ishikawa, A. R. Lupini, F. Oba, S. D. Findlay, N. Shibata, T. Taniguchi, K. Watanabe, H. Hayashi, T. Sakai, I. Tanaka, Y. Ikuhara, and S. J. Pennycook, Sci. Rep. 4, 3778 (2014).

144 H. Nakano, K. Watari, H. Hayashi, and K. Urabe, J. Am. Ceram. Soc. 85, 3093–3095 (2002).

145 D. Huang, Z. Tian, W. Cui, L. Gao, Z. Liu, X. Diao, and G. Liu, Ceram. Int. 44, 20556–20559 (2018).

146 T. Kusunose and T. Sekino, Ceram. Int. 42, 13183–13189 (2016).

147 A. T. Wieg, E. H. Penilla, C. L. Hardin, Y. Kodera, and J. E. Garay, APL Mater. 4, 126105 (2016).

148 I. Yonenaga, A. Nikolaev, Y. Melnik, and V. Dmitriev, in Materials Research Society Symposium Proceedings (Materials Research Society, 2002).

149 R. Terao, J. Tatami, T. Meguro, and K. Komeya, J. Eur. Ceram. Soc. 22, 1051–1059 (2002).

150 Q. Li, Z. Wang, C. Wu, and X. Cheng, J. Alloys Compd. 640, 275–279 (2015).

151 T. I. Mah, T. A. Parthasarathy, and D. L. Lee, J. Ceram. Proc. Res. 5(4) 369– 379(2004).

152 G.J. Quarles, in 46th Army Sagamore Materials Research Conference (Army Research Laboratory, 2005).

153 R. Gentilman, in 46th Army Sagamore Materials Research Conference (Army Research Laboratory, 2005).

154 T. Tani, Y. Miyamoto, M. Koizumi, and M. Shimada, Ceram. Int. 12, 33–37 (1986).

155 F. R. Charvat and W. D. Kingery, J. Am. Ceram. Soc. 40, 306–315 (1957).

2. FABRICATION OF HIGHLY TRANSPARENT THULIUM-DOPED Al_2O_3 NANOCRYSTALLINE CERAMICS

2.1 Introduction

Since the first demonstration of translucent alumina by Coble [1], great efforts have been made to develop optical ceramics for window [2], lasing [3], lighting [4,5], electro-optic [6], magneto-optic [7,8] and many more applications [9]. Among the most used optical materials, Al_2O_3 has attracted much interest because of its excellent thermal conductivity (30-35 $Wm^{-1}K^{-1}$ [10]) as well as mechanical toughness [11]. Power deliverable by a laser system scales with the thermal conductivity of the host media. The great potential of Al_2O_3 as a laser host material is easily appreciated through the scientific as well as commercial success of Cr:Al_2O_3 (ruby) and Ti:Al_2O_3 (titanium sapphire) which have enabled numerous technological breakthroughs [12, 13].

When compared with the most used rare earth (RE) laser host materials yttrium aluminum garnet (YAG) and silica glass, Al_2O_3 exhibits an over 2-fold and 20-fold improvement in thermal conductivity, respectively. However, incorporation of RE elements into single crystal sapphire has been challenging due to their low equilibrium solubility in Al_2O_3 lattice [14]. As alternatives, Al_2O_3 powders [15, 16], thin films [17, 18, 19], and ceramics [20, 21, 22, 23] have showed promising results in RE incorporation. Among these alternatives, Al_2O_3 ceramics show the greatest potential for size scaling, as the high thermal conductivity of Al_2O_3 is the most game-changing in bulk materials for laser power scaling [25]. Of particular interest with regard to laser development is the demonstration of optical gain in Nd: Al_2O_3 [22].

A major challenge facing the wider application of polycrystalline Al_2O_3 ceramics is its higher scattering loss compared with many other candidates such as YAG and silica glass. Since Al_2O_3 ceramics are almost always fabricated from powder densification/sintering approaches, residual porosity can be detrimental to the ceramics' transparency. Moreover, the hexagonal structural symmetry of Al_2O_3 produces different refractive indices along different crystallographic orientations, causing a Rayleigh-Gans-Debye (RGD) type scattering loss in polycrystals that is often referred to as birefringent scattering [24, 25]. One solution to minimize the birefringent scattering loss shown by R. Apetz and M. Van Bruggen is to reduce the Al_2O_3 grain size, so that it is much smaller than the light wavelength of interest [26]. Therefore, optimization of processing and densification techniques is crucial to minimize ceramic grain size while reaching full density in order to achieve high optical transparency.

With recent development in ceramic densification and sintering technologies, Nd^{3+} [22, 27], Er^{3+} [21], Tb^{3+} [20], Yb^{3+} [28], Eu^{3+} [23] doped Al_2O_3 ceramics have been reported. However, most $RE:Al_2O_3$ ceramics reported still suffer from unsatisfactory transparency at proposed lasing/emission wavelength caused by the birefringent scattering of polycrystalline Al_2O_3. The ions incorporated into alumina so far allow for light emission from the visible to the near-IR (~1.5 μm). Tm^{3+} doping would offer emission at a longer wavelength in the ~1.7 -2 μm region. In this work, we show fabrication of $Tm:Al_2O_3$ ceramics through current activated pressure assisted densification (CAPAD, also known as Spark Plasma Sintering, SPS, and Field Assisted Sintering, FAST) [29] with improved optical transparency and their spectroscopic properties. This is the first report of thulium incorporation into Al_2O_3 bulk ceramic to the best of our knowledge.

2.2 Experimental Procedure

2.2.1 Powder Preparation

Commercially available α-Al_2O_3 (TM-DAR, 99.99% purity, Taimei Chemicals, Japan) was doped with $Tm(NO_3)_3 \cdot 5H_2O$ (99.9% purity, Sigma Aldrich, USA). The powders were mixed at doping levels of 0.1, 0.25, and 0.35 at.% (cation ratio). The powders were hand mixed using a mortar and pestle in dry condition for 30 min, then planetary ball milled in dry condition using Si_3N_4 milling media at 450 RPM for 3 h with a powder: ball weight ratio of 1:10. After milling, the powders were sieved with 325 mesh stainless steel sieve and stored dry until further densification.

2.2.2 CAPAD Processing

The powders were densified by CAPAD using a graphite die (19 mm outer and 10 mm inner diameter). The graphite die and plunger set is placed inside a larger graphite die set (19 mm inner diameter). The die and plunger set with powder inside were placed into the CAPAD and a vacuum of 3×10^{-2} torr was achieved. The powders were heated to 400 °C under a uniaxial pressure of 10 MPa to remove adsorbed moisture. Then the powders were pre-pressed under a uniaxial pressure of 100 MPa for 5 min. The final densification involves a uniaxial pressure of 100 MPa with a pressure ramp rate of 33.3 MPa min^{-1}. Meanwhile, the sample was heated at a heating rate of ~300 °C/min and held at holding temperatures between 1200 °C to 1350 °C with a holding time of 10 min. Sample temperature was monitored using a dual wavelength optical pyrometer (Infrared thermometer IR-CZ, CHINO) focused on a hole at the midpoint of outer graphite die.

2.2.3 Microstructural Characterization

The powders and densified ceramics were characterized on a PANalytical X'Pert Diffractometer (PANalytical, Almelo, the Netherlands) using Cu Kα1 ($\lambda = 1.54058$ Å) radiation with a step size of $2\theta = 0.012°$. Published standards and literature were used for phase identification: α-Al_2O_3 (ICSD#:9770), $Tm_3Al_5O_{12}$ (JCPDS 17-0734). Microstructure of powders and densified ceramics were tested with a Zeiss Sigma 500 scanning electron microscope.

2.2.4 Transmission and photoluminescence Measurements

The densified ceramics were polished with diamond suspension down to 1 μm. Samples have thicknesses of 1 mm ± 0.07mm (1 mm ± 0.02mm for transparent samples). Transmission spectra were taken on a Cary 7000 UV-VIS-IR spectrometer (Agilent Technologies, USA) from 200 nm to 2500 nm with a scan rate of 10 nm/s.

Photoluminescence was measured on a Horiba Spectrophotometer using an 683nm pulsed laser from a Horizon Optical parametric oscillator (Continuum, USA) pumped by a Surelite nanosecond pulsed laser (Continuum, USA) as excitation light source. Samples were set in front face mode with incident angle of 45°. Emission scans were taken between 1550 nm and 2100 nm with an integration time of 1s/nm.

Photoluminescence lifetimes were measured using a Surelite pulsed laser (Continuum, USA) paired with a Horizon Optical parametric oscillator (Continuum, USA). The pulse width of the laser is 6 ns, with wavelength of 685 nm and incident energy of 5 mJ per pulse. The ceramics were set in a Spectrofluorometer (New PTI QuantaMaster 8075, Horiba Canada). A 900 nm long pass filter (Thorlabs) was used to remove pumping light. Emission from the samples were detected with an InGaAs detector. Measurements were measured in front face mode with an incident angle of 45°.

2.3 Results and Discussion

Commercial Al_2O_3 and $Tm(NO_3)_3{\cdot}5H_2O$ powders were mixed before densification in CAPAD. As porosity and birefringence related scattering are the main scattering sources in polycrystalline Al_2O_3 [24, 25], it is necessary to minimize grain growth while removing sample porosity to achieve high transparency. **Figure 2.1** shows effect of densification temperature on density for Al_2O_3 ceramics doped with different Tm^{3+} concentrations, with the inset showing the 1 mm thick samples placed ~1cm above back lit text. As expected, density generally increase as temperature increase. Densification behavior is dependent on dopant concentration. As Tm^{3+}

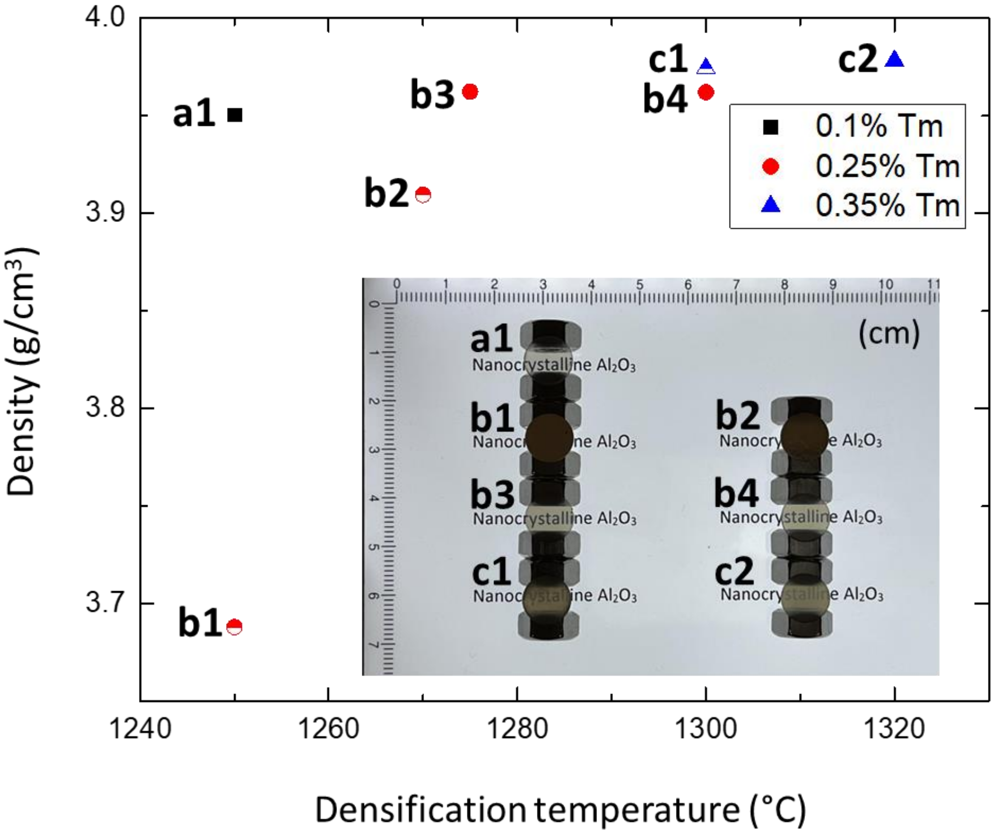

Figure 2.1 Densification temperature dependence of $Tm{:}Al_2O_3$ sample densities with varying Tm^{3+} concentrations. Photo inset shows 1mm thick samples 1cm above back lighted printed text. Sample conditions: **a1**: 0.1 at.% Tm, 1250°C, **b1**: 0.25 at.% Tm, 1250°C, **b2**: 0.25 at.% Tm, 1270°C, **b3**: 0.25 at.% Tm, 1275°C, **b4**: 0.25 at.% Tm, 1300°C, **c1**: 0.35 at.% Tm, 1300°C, **c2**: 0.35 at.% Tm, 1320°C.

concentration increases from 0.1 at.% to 0.35 at.%, the densification temperature necessary to achieve full density increases from 1250°C to 1320°C. We believe this is caused by Tm containing phases inhibiting temperature activated particle rearrangement and grain sliding/grain boundary diffusion. Full density also increases as Tm doping concentration increases from sample **a1** (0.1 at.%) to sample **b4** (0.25 at.%), then to sample **c2** (0.35 at.%).

Good optical transparency was achieved for the fully dense samples **a1**, **b3**, **b4**, and **c2**, as indicated by the clearly visible text under the sample. A comparison between sample **b2** and **b3** shows the density and transparency sensitivity to densification temperature. With the same 0.25 at.% Tm doping concentration, sample **b2** densified at 1270°C has 1.5% remaining porosity which

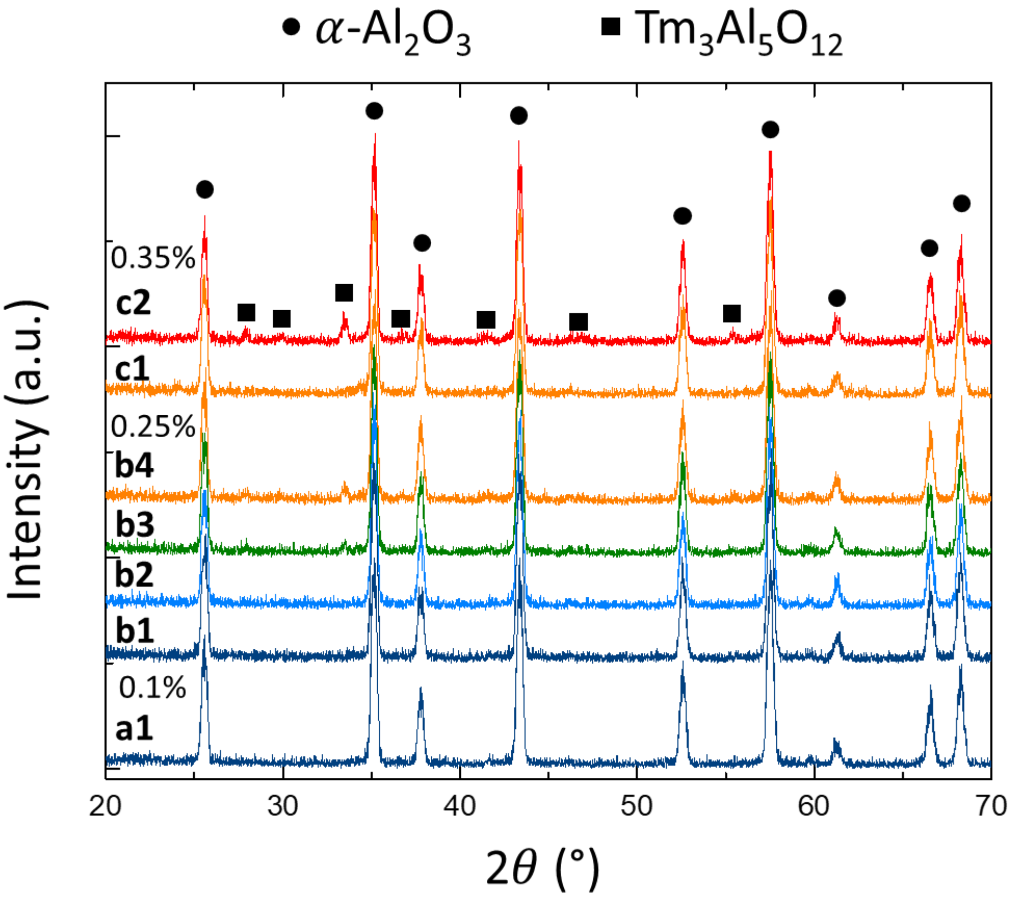

Figure 2.2 X-Ray diffraction profiles of Tm:Al_2O_3 bulk ceramics.

resulted in an opaque sample, while sample **b3** densified at only 5°C higher is fully dense and highly transparent.

Figure 2.2 shows the X-ray diffraction patterns of densified bulk ceramics. The ceramics are all primarily α- Al_2O_3 phase. Some samples (**b3**, **b4**, and **c2**) also show minor $Tm_3Al_5O_{12}$ Thulium Aluminum Garnet (TAG). For 0.1 at.% Tm doped sample (**Fig. 2.2 a1**), TAG phase was not observed. As Tm concentration increased to 0.25 at.% (**Fig. 2.2 b1**, **b2**, **b3**, **b4**), TAG phase formation showed clear temperature dependence. The opaque samples **b1** and **b2** densified at 1250°C and 1270°C respectively showed no TAG peaks, while the transparent samples **b3** and **b4** densified at 1275°C and 1300°C respectively showed clear TAG phase. Similar behavior was observed for 0.35 at.% Tm doped samples. The 1300°C sample **c1** only showed peaks corresponding to α- Al_2O_3 phase, while the 1320°C sample **c2** showed clear TAG peaks. As can be seen from **Figure 2.2**, the TAG phase formation depends both on Tm concentration and densification temperature. As Tm concentration increases from 0.25 at.% to 0.35 at.%, the onset of the TAG formation temperature increases from 1275°C to 1320°C.

Figure 2.3 shows SEM micrographs of polished surfaces of densified ceramics. The SEM micrographs showed sub-micron grain sizes with minimum residual porosity for samples **a1**, **b3**, **b4**, **c1**, and **c2**, which agree well with high densities measured using Archimedes method. The

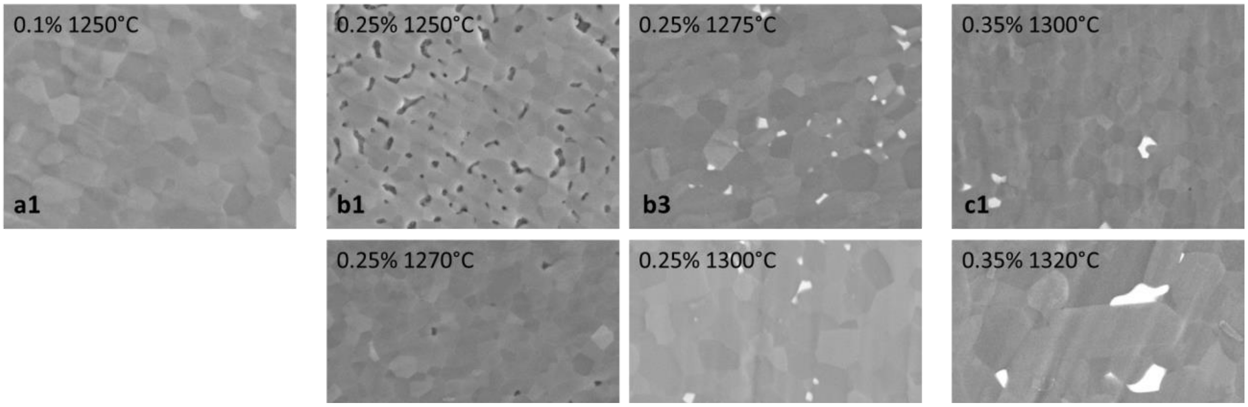

Figure 2.3 SEM micrographs of polished surfaces of $Tm:Al_2O_3$ samples. Bright spots in sample **b3**, **b4**, **c1**, and **c2** indicates thulium segregation.

microstructures of all samples showed sub-micrometer grains that are equiaxed (spatially isotropic). Sample **b3**, **b4**, **c1**, **c2** showed bright regions at triple points that indicate higher concentration of high Z-number elements, which we believe is a sign of rare earth segregation. The comparison between 0.1 at.%, 0.25 at.%, and 0.35 at.% Tm doped ceramics shows that Tm segregation becomes more significant with increasing doping concentration as expected. The comparison between 0.25 at.% Tm doped samples **b1**-**b4** shows that the degree of Tm segregation depends on densification temperature. When compared with phase composition shown in **Figure 2.2**, Tm segregation shows correlation with TAG phase formation, as sample **b3** shows first sign of both TAG formation and Tm segregation, while sample **b2** shows neither. However, when Tm doping concentration further increases to 0.35 at.%, sample **c1** shows clear Tm segregation although it shows no TAG formation based on XRD data.

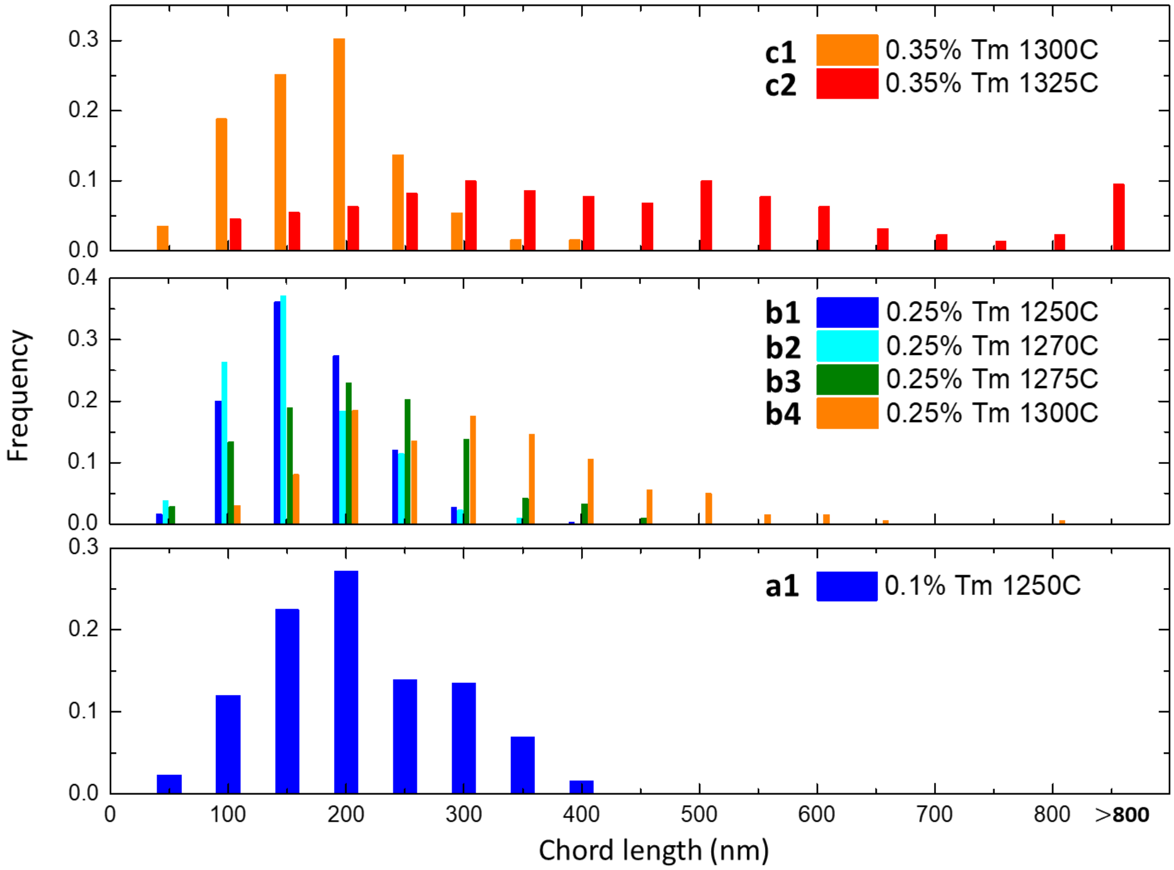

Figure 2.4 Chord length distributions of Tm:Al_2O_3 ceramics.

Chord length distributions were measured using straight line intersect method [30, 31] and are shown in **Figure 2.4**. The frequency is calculated by normalizing the number of chords that fall in a range by total number of chords counted. Chord length of highly transparent sample **a1** and **b3** have chord length well below 1 μm, while sample **c2** has significant grain growth compared to sample **c1** due to increased densification temperature. **Figure 2.5** shows the average chord lengths of the 7 samples with error bars representing standard deviations of the chord length distributions. All 7 samples have average chord lengths below 500 nm, which increases with higher densification temperature at a given Tm^{3+} concentration. For samples **a1**, **b1**, **b2**, **b3**, and **c1**, the average chord lengths are below 200 nm, indicating the fine grains of the ceramics. With the same densification temperature, ceramics with higher Tm^{3+} concentration have shorter chord lengths, which we believe is due to the pinning effect of dopant Tm^{3+} ions.

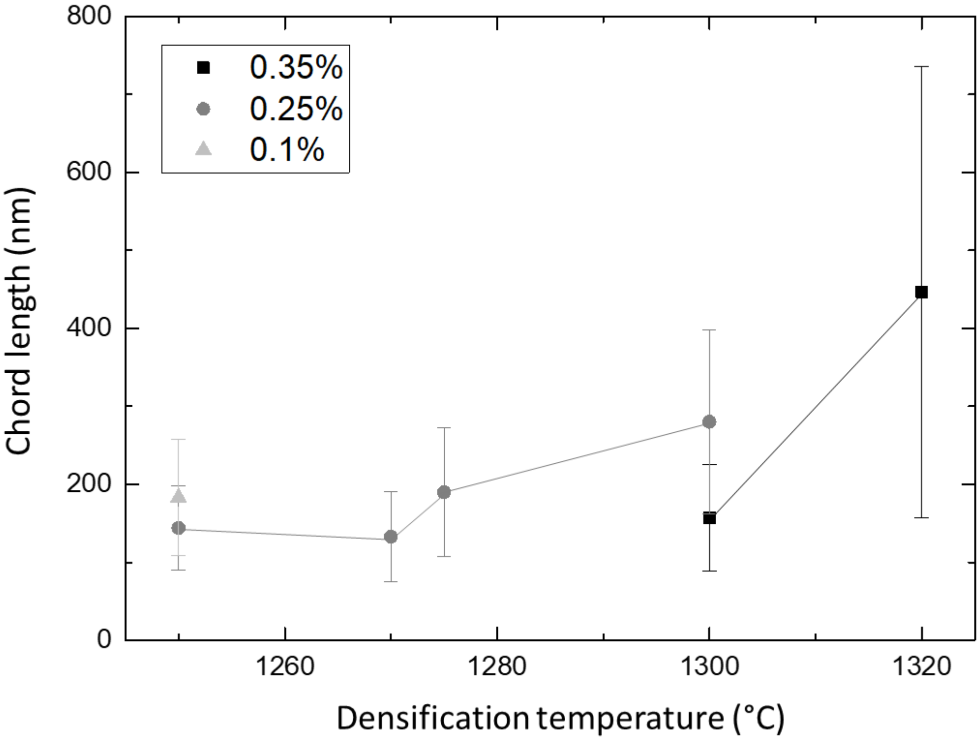

Figure 2.5 Densification temperature dependence of $Tm:Al_2O_3$ ceramic average chord length. Standard deviations of chord length are shown as error bars.

Wavelength dependent in-line transmission of densified ceramics from the UV, through the visible and into the near-IR (NIR) are shown in **Figure 2.6**. As shown in **Figure 2.6(A)**, the samples showed high in-line transparency approaching the theoretical transparency of sapphire ~86% in the NIR wavelength range. The total loss (scattering and absorption losses) of sample **a1** at 2.5 μm is within 5%. Apetz and van Bruggen [26] developed a light scattering model for dense fine grained polycrystalline Al_2O_3 showing that the in-line transmission can be described well by Rayleigh-Gans-Debye (RGD) scattering, having a wavelength dependence of λ^{-2}. As shown in

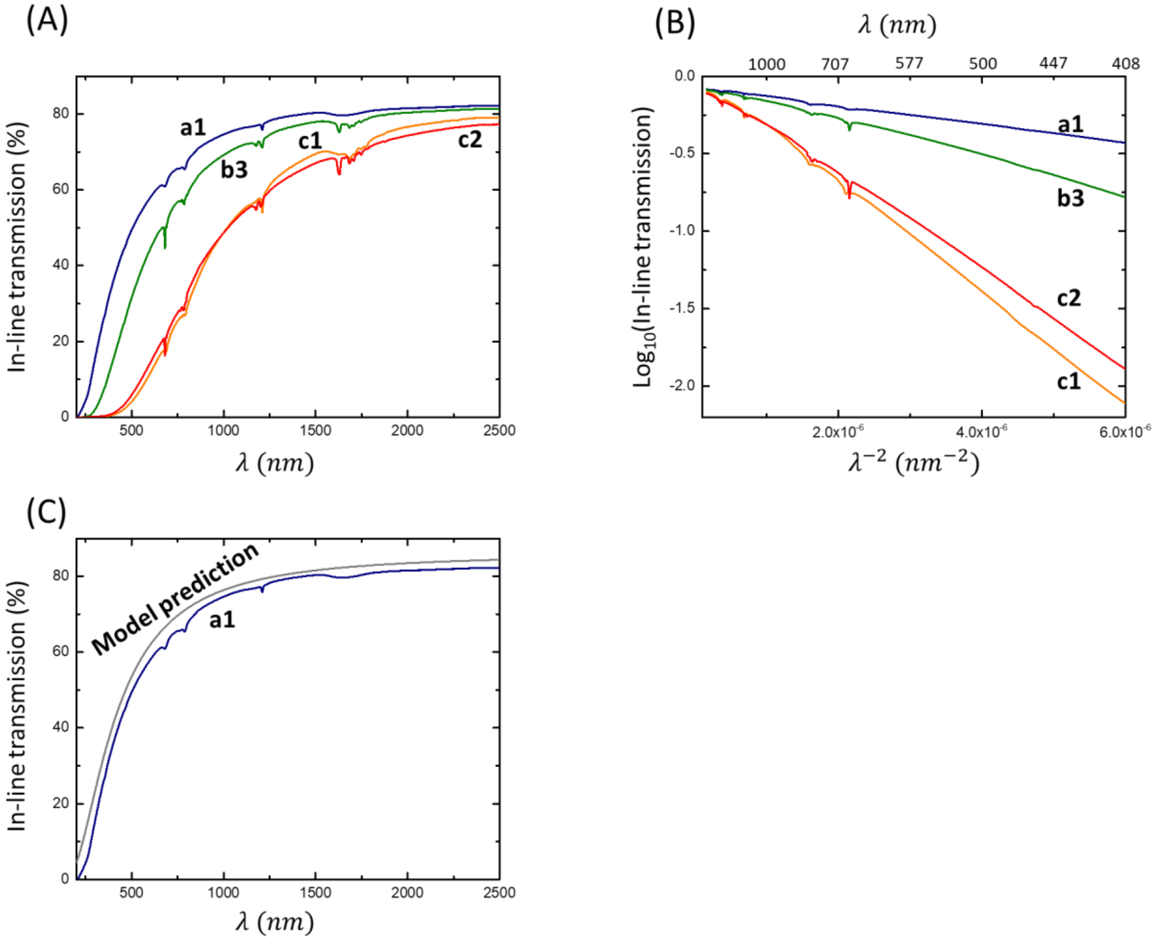

Figure 2.6 (A) In-line transmission of $Tm:Al_2O_3$ samples with 1 mm thickness, showing high transparency and characteristic absorption bands from Tm^{3+}. (B) In-line transmission plotted in log scale vs λ^{-2}. Sample conditions: **a1**: 0.1 at.% Tm, 1250°C, **b3**: 0.25 at.% Tm, 1275°C, **c1**: 0.35 at.% Tm, 1300°C, **c2**: 0.35 at.% Tm, 1320°C. (C) In-line transmission of $Tm:Al_2O_3$ sample **a1** compared with model prediction for 285 nm grain size.

Figure 2.6(B), logarithmic in-line transmission as a function of λ^{-2} showed good linearity, indicating a good agreement with the Apetz and van Bruggen model and dominant RGD type scattering. This suggests the birefringent nature of Al_2O_3 instead of porosity being the dominant scattering source for samples **a1**, **b3**, **c1**, and **c2**.

With RGD-type scattering that originate from the birefringence of Al_2O_3 being the dominant scattering mechanism, in-line transmission of the most transparent sample **a1** can be compared with model predictions using the light scattering model developed by Apetz and van Bruggen [26] in which real in line transmission (RIT) is described by:

$$RIT(\lambda) = (1 - R)e^{-\frac{3\pi^2 r \Delta n^2 l}{\lambda^2}}\ , \tag{5}$$

where R is reflection loss from two surface reflection loss $R = 2\left(\frac{n-1}{n+1}\right)^2 - \left(\frac{n-1}{n+1}\right)^4$ following Fresnel equations, and n is the refractive index of the sample. Correction terms for further reflections on reflected light is neglected because it is less than 0.5% correction for our analysis [24]. (n = 1.74 was used as an average refractive index), r is half the average grain size, l is thickness of the sample, Δn is the average birefringence over all grain orientations. A $\Delta n = (2/3)\Delta n_{max} = 0.0053$, ($\Delta n_{max} = |n_e - n_o|$ is the absolute birefringence of the material) was used as a first order approximation assuming random grain orientation distribution following the Apetz-Van Bruggen approach. As shown in **Figure 2.5**, sample **a1** has an average chord length (ACL) of 183 nm, which relate to an average grain size (AGS) of 285 nm based on the proportionality constant of 1.56 between AGS and ACL proposed for polycrystalline ceramics [30, 31]. As shown in **Figure 2.6(C)**, in-line transmission of sample **a1** agrees well with model prediction for polycrystalline Al_2O_3 with AGS of 285 nm.

The minor discrepancy between experimental data and model prediction is expected since the model prediction only takes surface reflection loss and RGD-type loss into consideration. More optical losses may originate from very small amount of remaining porosity or secondary phase (which may have a different scattering behavior e.g. Rayleigh scattering [24]) as well as absorption losses caused by Tm^{3+} dopant and potential impurities. Since these additional optical losses were not considered in the model prediction, it is not surprising that experimentally measured in-line transmission is slightly lower than model prediction.

The successful incorporation of Tm into the alumina ceramics is can also be deduced from the transmission measurements. Characteristic absorption bands from Tm^{3+} can be observed in **Figure 2.6(A)**. Based on the absorption peak depth, absorption cross section for 0.1 at.% $Tm:Al_2O_3$ (sample **a1**) is $\sigma_{Tm} = 6 \times 10^{-21}\ cm^2$ at 682 nm, and $\sigma_{Tm} = 8 \times 10^{-21}\ cm^2$ at 789 nm. This absorption cross section is comparable to that in silica glass host [32] and lower than that in YAG [33].

Table 2.1 shows a summary of recent transparent transition metal-doped and rare earth-doped Al_2O_3 works. The loss coefficients are calculated based on the reported transmission measurement, if not directly reported in the corresponding literature. The $Tm:Al_2O_3$ in this work exhibit the lowest loss coefficient among $RE:Al_2O_3$, with a value of 1.37 cm^{-1} at 1 μm, only second to the $Cr:Al_2O_3$ fabricated by B. Ratzker and coworkers using high pressure CAPAD technique [34]. Thanks to the long emission wavelength of Tm^{3+} near 1.8 μm, our $Tm:Al_2O_3$ takes advantage of the low scattering loss at longer wavelength in polycrystalline Al_2O_3, showing the lowest total loss coefficient of 0.6 cm^{-1} at the major emission wavelength.

Table 2.1 Recent transparent rare earth/transition metal doped Al_2O_3 ceramic reports.

Material system	Grain size	Loss coefficient at 1 μm (cm^{-1})	Loss coefficient at major emission λ (cm^{-1})	Reference
Transition metal doped				
$Cr:Al_2O_3$	~340 nm	-	-	E. Penilla et al. [35]
$Cr:Al_2O_3$	180 nm	1.06	2.15 @ 694 nm (absorption corrected)	B. Ratzker et al. [34]
Rare earth doped				
$Tb:Al_2O_3$	~240 nm	-	-	E. Penilla et al. [20]
$Er:Al_2O_3$	-	-	-	T. Sanamyan et al. [21]
$Nd:Al_2O_3$	>20 um	9.64	9.45 @ 1064 nm	Y. Gui et al. [27]
$Nd:Al_2O_3$	~250 nm	1.89	1.32 @ 1064 nm	E. Penilla et al. [22]
$Er/Yb:Al_2O_3$	10-30 um	-	-	Q. Yang et al. [28]
$Eu:Al_2O_3$	400 nm	2.75	7.16 @ 612 nm	R. Klement et al. [23]
$Tm:Al_2O_3$	200-300 nm* (ACL 183 nm)	1.37	0.60 @ 1780 nm	Present work

Figure 2.7 shows the photoluminescence of transparent Tm:Al_2O_3 samples **a1**, **b3**, **c1**, and **c2** when excited at 683 nm ($^3H_6 \rightarrow {}^3F_{2,3}$). Emission spectra of sample **a1** (0.1 at.% Tm), **b3** (0.25 at.% Tm), **c1** (0.35 at.% Tm) and **c2** (0.35 at.% Tm) have identical center wavelength around 1.78 μm ($^3F_4 \rightarrow {}^3H_6$) and similar width with FWHM around 200 nm. The emission line shape is much broader compared with the sharp emission peaks in Tm:YAG [33]. This is consistent with our previous work on RE doped alumina where the emission bandwidth in the Nd system was shown to be higher than Nd:YAG single crystals [22]. Emission spectrum of sample **a1** shows a broad hump across 1.6-2.0 μm, with peak structures around 1.78 μm, 1.84 μm, and 1.88 μm. As Tm^{3+} concentration increases from 0.1 at.% to 0.25 at.% and 0.35 at.%, sample **a1**, **b3**, and **c1** showed

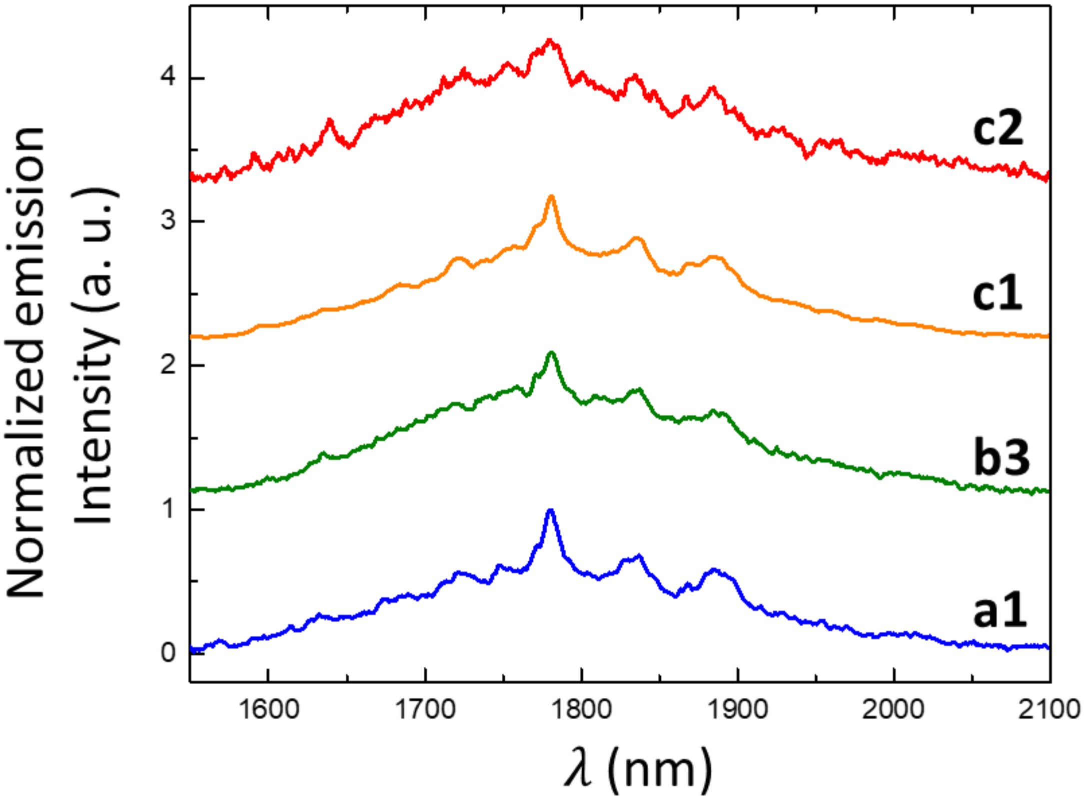

Figure 2.7 Emission spectra of Tm:Al_2O_3 samples with different Tm^{3+} concentrations. Sample conditions: **a1:** 0.1 at.%Tm 1250°C, **b3:** 0.25 at.%Tm 1275°C, **c1:** 0.35 at.%Tm 1300°C, **c2:** 0.35 at.%Tm 1320°C.

similar emission line shape, with the sharp peak structures slightly less significant for sample **b3**. This is possibly caused by the minor TAG phase formation in sample **b3** while no TAG phase formation was observed in sample **a1** and **c1** as shown in **Figure 2.2**.

Further evidence of the correlation between TAG phase formation and photoluminescence line shape was found as densification temperature increases from 1300°C to 1320°C for the 0.35 at.% Tm doped samples (**c1** & **c2**). At the same Tm^{3+} doping concentration of 0.35 at.%, sample **c1** has substantially finer peak structures compared with sample **c2**. We also noticed in our measurement that the emission intensity from sample **c1** is stronger than that from sample **c2**. As shown by the XRD spectra (**Figure 2.2)**, sample **c2** has clearly observable peaks from the garnet phase showing clear TAG phase formation while sample **c1** has no evidence of TAG formation because of the slightly lower densification temperature. The comparison between sample **c1** and **c2** shows that TAG formation, either caused by heavy doping and higher processing temperature, reduces emission intensity as well as peak structures. We believe this is caused by the concentration quenching effect due to the close Tm-Tm distance in the TAG phase.

2.4 Chapter 2 Summary and Conclusion

We produced highly transparent thulium doped nanocrystalline Al_2O_3 ceramics with various Tm concentrations through CAPAD. Full density was achieved with fine grain size and average chord length below 200 nm. This is the first report of thulium incorporation in Al_2O_3 ceramic and spectroscopic study on $Tm:Al_2O_3$. Formation of Thulium aluminum garnet (TAG) phase was found to reduce emission peak structures and emission intensity. The $Tm:Al_2O_3$ nanocrystalline ceramic produced has the lowest loss coefficient of 0.6 cm^{-1} at the major emission wavelength among all rare earth/transition metal doped Al_2O_3 ceramics reported. These results show progress towards thermally/mechanically superior Al_2O_3 based transparent ceramics that have great potential for lasing/lighting applications.

Chapter 2, in full, is co-authored with Dr. Y. Kodera and Dr. J. E. Garay, and is currently in preparation for submission to publish. The dissertation author was the primary investigator and author of this paper.

2.5 Chapter 2 References

1 R. L. Coble , Transparent Alumina and Method of Preparation 1962 ,US Patent 3026210.

2 Byung-Nam Kim, Keijiro Hiraga, Koji Morita, Hidehiro Yoshida, Scr. Mater, 57, 607-610 (2007)

3 A. Ikesue, T. Kinoshita, K. Kamata, K. Yoshida, J. Am. Ceram. Soc. 78, 1033–40 (1995).

4 A. T. Wieg, E. H. Penilla, C. L. Hardin, Y. Kodera, J. E. Garay, APL Mater, 4, 126105 (2016),

5 E. H. Penilla, P. Sellappan, M.A. Duarte, A. T. Wieg, P. Martinez-Torres, M. C. Wingert, J. E. Garay, J. Mater. Res. 35, 958–971 (2020).

6 A. D. Dupuy, Y. Kodera, J. E. Garay, Adv. Mater, 28, 7970–7977 (2016).

7 J. R. Morales, N. Amos, S. Khizroev, J. E. Garay, J. Appl. Phys. 109, 093110 (2011).

8 H. Furuse, R. Yasuhara, K. Hiraga, S. Zhou, Opt. Mater. Express 6, 191–196 (2016).

9 Z. Xiao, S. Yu, Y. Li, S. Ruan, L.B. Kong, Q. Huang, Z. Huang, K. Zhou, H. Su, Z. Yao, W. Que, Y. Liu, T. Zhang, J. Wang, P. Liu, D. Shen, M. Allix, J. Zhang, D. Tang, Mater. Sci. Eng. R Reports. 139, 100518 (2020).

10 R.W. Powell, C.Y. Ho, P.E. Liley, Thermal Conductivity of Selected Materials, Part 2, 1966.

11 W. Yao, J. Liu, T.B. Holland, L. Huang, Y. Xiong, J.M. Schoenung, A.K. Mukherjee, Scr. Mater. 65, 143–146 (2011).

12 T.H. Maiman, Nature. 187, 493 (1960).

13 P.W. Roth, D. Burns, A.J. Kemp, Opt. Express. 20, 20629 (2012).

14 M.D. Chambers, D.R. Clarke, , Annu. Rev. Mater. Res. 39, 325–359 (2009).

15 G.R. Williams, S.B. Bayram, S.C. Rand, T. Hinklin, R.M. Laine, Phys. Rev. A. 65, 6 (2001).

16 B. Li, G. Williams, S.C. Rand, T. Hinklin, R.M. Laine, Opt. Lett. 27, 394 (2002).

17 Q. Song, C.R. Li, J.Y. Li, W.Y. Ding, S.F. Li, J. Xu, X.L. Deng, C.L. Song, Opt. Mater. (Amst). 28, 1344–1349 (2006).

18 S.H. Waeselmann, S. Heinrich, C. Krankel, G. Huber, Adv. Solid State Lasers Conf. ©, 2015.

19 S.H. Waeselmann, S. Heinrich, C. Kränkel, G. Huber, Laser Photonics Rev. 10, 510–516 (2016).

20 E.H. Penilla, Y. Kodera, J.E. Garay, Adv. Funct. Mater. 23, 6036–6043 (2013).

21 T. Sanamyan, R. Pavlacka, G. Gilde, M. Dubinskii, Opt. Mater. (Amst). 35, 821–826 (2013).

22 E.H. Penilla, L.F. Devia-Cruz, M.A. Duarte, C.L. Hardin, Y. Kodera, J.E. Garay, Light Sci. Appl. 7 (2018).

23 R. Klement, K. Drdlíková, M. Kachlík, D. Drdlík, D. Galusek, K. Maca, J. Eur. Ceram. Soc. 41, 4896–4906 (2021).

24 M. H. Shachar, G. Uahengo, E. H. Penilla, Y. Kodera, J. E. Garay, J. Appl. Phys. 128, 083103 (2020).

25 X. Wu, L. Tang, C. L. Hardin, C. Dames, Y. Kodera, and J. E. Garay, J. Appl. Phys. 131, 020902 (2022).

26 R. Apetz, M.P.B. Van Bruggen, J. Am. Ceram. Soc. 86, 480–486 (2003).

27 Y. Gui, Q. Yang, Y. Shao, Y. Yuan, J. Lumin. 184, 232–234 (2017).

28 Q. Yang, B. Jiang, S. Chen, Y. Jiang, P. Zhang, J. Wang, S. Xu, L. Zhang, J. Lumin. 199, 45–52 (2018).

29 J. E. Garay, Annu. Rev. Mater. Res. 40, 445 (2010).

30 J. C. Wurst, J. A. Nelson, J. Am. Ceram. Soc. 55, 109 (1972).

31 Mel I. Mendelson, J. Am. Ceram. Soc. 52, 443 (1969).

32 B.M. Walsh, N.P. Barnes, Appl. Phys. B Lasers Opt. 78, 325–333 (2004).

33 J. Körner, T. Lühder, J. Reiter, I. Uschmann, H. Marschner, V. Jambunathan, A. Lucianetti, T. Mocek, J. Hein, M.C. Kaluza, J. Lumin. 202, 427–437 (2018).

34 B. Ratzker, A. Wagner, B. Favelukis, S. Goldring, S. Kalabukhov, N. Frage, J. Eur. Ceram. Soc. 41, 3520–3526 (2021).

35 E.H. Penilla, C.L. Hardin, Y. Kodera, S.A. Basun, D.R. Evans, J.E. Garay, J. Appl. Phys. 119 (2016).

3. IMPROVED LIGHT TRANSMISSION IN NANOCRYSTALLINE ALUMINUM NITRIDE

3.1 Introduction and Motivation

Polycrystalline ceramics for high temperature window and transparent armor applications have been widely studied and utilized.[1-6] Windows are crucial for protecting people and electronic/optoelectronic devices from harsh environments. In some high temperature optical-structural applications, the temperature changes are relatively slow and the important mechanical design parameter is the temperature dependent compression strength, which typically scales with melting point. The high melting point of ceramics makes them the clear choice for such applications. On the other hand, in environments where the dynamic temperature fluctuations are fast, the dominant failure mechanism becomes thermal shock. The figure of merit for thermal shock, R_s can be written:

$$R_s = \frac{k(1-\nu)}{\alpha E}\sigma_F \tag{6}$$

where k is thermal conductivity, ν is Poisson's ratio, α is the thermal expansion coefficient, E is Young's modulus and σ_F is the fracture stress which is proportional to the fracture toughness of the material.

Eq. (6) shows that R_s scales with thermal conductivity which makes sense because materials with high k can quickly dissipate thermal gradients which ultimately cause fracture. In turn, reducing the weight of structural/functional parts are crucial for increasing fuel efficiency, range and performance for mobile vehicles. Therefore, identifying and developing new *low density, mechanically robust, high thermally conductive* materials that can withstand harsh environments are of utmost importance for improved land, air, and space vehicles.

A variety of polycrystalline oxide ceramics have been developed with optical, mechanical, and thermal properties that are comparable or superior to their single crystal counterparts.[2-10] However, most oxide materials have limited intrinsic thermal conductivity and are thus susceptible to temperature gradient build up and thermal shock. An alternative material with the desired optical, thermal, and mechanical properties is aluminum nitride (AlN). While most metal oxide materials that are considered for mentioned applications have thermal conductivities between 5 to 40 $Wm^{-1}K^{-1}$at room temperature, AlN has a remarkable intrinsic thermal conductivity of 320 $Wm^{-1}K^{-1}$,[11] which is close to highly conductive metals such as gold and copper.

It has been shown that polycrystalline AlN ceramic has a high fracture toughness comparable to that of alumina and much higher than glass,[12] making it an excellent structural ceramic. Combined with its high thermal conductivity, AlN exhibits a superb thermal shock resistance R_s. The R_s of AlN ceramic is 2.5 times higher than that of alumina, 60 times higher than that of YAG, and 4 orders of magnitude higher that of glass.[12,13] Besides its exceptional thermal conductivity and thermal shock resistance, AlN possesses the optical properties required for a wide range of optical applications. AlN has a wide bandgap of 6.2 eV,[14] which gives it a wide optical transparency window across UV, visible and NIR wavelength ranges. Density normalized (specific) Young's modulus and optical transparency window of AlN and several commonly used window materials are shown in **Figure 3.1 (a).** The wide optical transparency range of AlN across UV-Vis-NIR is comparable to sapphire, YAG and $MgAl_2O_4$ spinel, while the lower density and high Young's modulus of AlN give it a higher specific modulus, indicating a perfect candidate for lightweight robust wide spectrum window material.

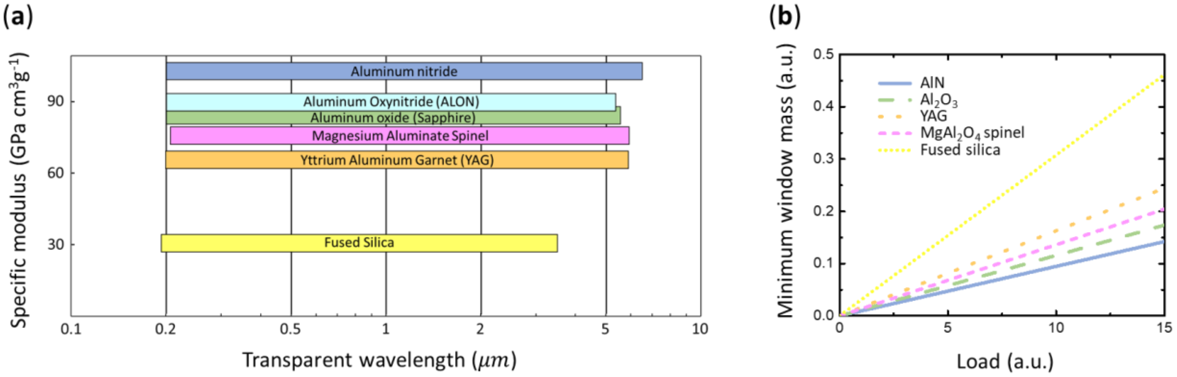

Figure 3.1 (a) transmission window and specific modulus of selected transparent materials (material properties adapted from [2, 15-24]). (b) Minimum mass of window material required for selected materials to support varying mechanical load with a given window size and deformation threshold.

The impact of a high density-normalized modulus on weight reduction can be emphasized by considering a design case study where a window supports a compressive or tensile load and there is a maximum acceptable deformation. The minimum window weight *vs*. external applied load is plotted in **Figure 3.1 (b)** for a load along the window plane, with a given window size and maximum acceptable deformation. Compared with utilized optical-structural materials, AlN is the most lightweight material as shown in **Figure 3.1 (b)**. The combination of its wide transparency wavelength range, light weight, high mechanical stiffness, and thermal stability makes AlN an appealing candidate for window materials, especially for mechanically and thermally challenging applications.

The major challenge for polycrystalline AlN optical ceramics has been their low transparency. For many optical applications high in-line transparency is required to ensure communication between source and sensor. Reduced in-line transmission in polycrystalline ceramics mainly involves 2 mechanisms: (1) *absorption loss*, and (2) *scattering loss*. Absorption loss can originate from impurities, vacancies and their complexes in addition to the fundamental cross-band gap absorption, while scattering loss mainly involves pores, secondary phases, and birefringent scattering from large grain sizes.[25] For polycrystalline AlN ceramics, transparency is hard to achieve because of all 3 scattering sources.

AlN powder suffers from oxygen contamination [26] both from synthesis residual and contamination during transportation and handling. Also, the high melting temperature and sintering temperature of AlN makes it very difficult to achieve full density using conventional sintering techniques. To achieve high density and minimize residual porosity, sintering additives, high densification temperature close to 2000°C, and long holding time of hours are often applied, increasing grain growth,[15,27-29] and leading to more birefringent scattering.[1] It is a major challenge to achieve low porosity while maintaining small grain sizes in polycrystalline AlN ceramic, but both are required for optical transparency.

Previous AlN bulk ceramics reported that achieved optical transparency/translucency mostly have grain sizes in the micrometers range [15,27-32] and sintering additives are often necessary to assist the sintering process.[15, 28, 29, 32] The in-line transmittance of AlN ceramics is generally below 25% at $2.5 \mu m$ [15,29] in samples ~ 0.5 mm thick. Since the optical scattering loss becomes even more detrimental as wavelength decreases, in-line transmission in the visible and NIR wavelength ranges below 2.5 μm are often too low and not reported.[15,29] Grain size reduction to around 200 nm has been achieved but optical transparency could not be achieved.[33,34] In our previous work, synthesis and densification of nanocrystalline AlN was demonstrated and the grain size was further reduced,[35] but improvements in powder purity and bulk ceramic density were also needed to achieve optical transparency.

In this work, we present the synthesis of nano-grain AlN powder through solid-gas reduction in a custom-made reaction apparatus, as well as the densification of the powder into bulk AlN nanocrystalline ceramics using current activated pressure assisted densification (CAPAD, also known as Spark Plasma Sintering, SPS, and Field Assisted Sintering, FAST)[36] without any sintering additive. Our powder synthesis method allows a reduced nitridation temperature as low as 1150°C while preserving the nanocrystallinity of the powder. With the combination of a low temperature powder synthesis route and a low temperature fast ceramic densification technique, fine grained AlN nanocrystalline ceramics were produced. The bulk AlN ceramic was fully dense with an average grain size of 230 nm, which is nearly one order of magnitude smaller than most transparent/translucent AlN ceramics reported. The AlN ceramic showed an in-line transmission of over 55% at 2.5 μm, which, to the best of our knowledge, is the highest NIR transmission for polycrystalline AlN ceramics ever reported. This work opens the door for AlN nanocrystalline ceramics being used in light transmitting window applications in the NIR wavelength range and possibly even visible range in the future.

3.2 Experimental Procedure

3.2.1 Powder Preparation

AlN nano-powder was synthesized by converting commercially available γ-Al_2O_3 (99.99% purity, Inframat, Advanced Materials) in NH_3 (Praxair Ammonia 5.0 Research Grade 99.999% purity) flow using a custom-made reactor. It should be noted that γ-Al_2O_3 and δ-Al_2O_3 have similar crystal structures, making phase identification between the two through X-ray diffraction difficult, especially with the peak broadening caused by fine grain sizes and defective nature of both phases. The precursor powder was labeled as γ phase transition Al_2O_3 by the manufacturer but it is possible that δ phase transition Al_2O_3 may be present in the powder, as we showed in our earlier work.[35] In this work, we have no clear evidence indicating the presence of δ phase, therefore refer to the starting powder as γ-Al_2O_3. The reactor consists of an open-ended inner tube (O.D. 12.7 mm, I.D. 10.5 mm) inside a closed-ended outer tube (O.D 25 mm, I.D. 22 mm), both made of fused quartz (Advalue Technology), with stainless steel and aluminum fittings. During nitridation reaction, NH_3 gas flows downward through the inner tube and then upward between the inner tube and outer tube towards the exhaust. 0.33 g of starting γ-Al_2O_3 precursor powder was placed at the bottom of the outer tube, covering the bottom opening of the inner tube. The reactor was then placed in a vertically positioned furnace (MELLEN model SC12-3X12). The reaction temperature was between 1150°C, with a heating rate of 5°C/min. The reaction was held at the holding temperature for 24 hours. 250 cm^3/min of N_2 gas was supplied to purge the reactor under 200°C, then 250 cm^3/min of NH_3 flow was supplied during heating and holding. After the reaction was complete, the reactor was sealed during cooling and then transferred into an Ar filled glove box for further processing and densification.

3.2.2 CAPAD Processing

The powders were densified by CAPAD (also referred to as SPS and FAST) using a graphite die (19 mm outer and 10 mm inner diameter). The graphite die and plunger set is placed inside a larger graphite die set (19 mm inner diameter). The die and plunger set with powder inside were placed into the CAPAD and a vacuum of 3×10^{-2} torr was achieved. The powders were pre-pressed under a pressure of 100 MPa for 5 min. The final densification involves a pressure of 100 MPa with a pressure ramp of 33.3 MPa/min. At the same time, the sample was heated at a heating rate of 200-300 °C/min and held at holding temperatures between 1400°C to 1600°C with a holding time of 10 min. Sample temperature was monitored using a dual wavelength optical pyrometer (Infrared thermometer IR-CZ, CHINO) focused on a hole at the midpoint of the outer graphite die.

3.2.3 Microstructural Characterization

The powders and densified ceramics were characterized on a PANalytical X'Pert Diffractometer (PANalytical, Almelo, The Netherlands) using Cu Kα ($\lambda = 1.541$ Å) radiation with a step size of $2\theta = 0.01°$. Published standards were used for comparison: α-Al_2O_3 (ICSD coll#:9770), AlN (ICSD coll#:34475), $Al_{2.85}O_{3.45}N_{0.55}$ (ICSD coll#:70032). The microstructure of powders and densified ceramics were tested with a Zeiss Sigma 500 scanning electron microscope.

3.2.4 Transmission Measurements

The densified ceramics have thicknesses of between 0.6 mm and 1 mm. Transmission spectra were taken on a UV-VIS-NIR spectrophotometer (Cary 5000 UV-Vis-NIR, Agilent Technologies) from 200 nm to 2500 nm with a scan rate of 10 nm/s. The detector collects light within ~10° from the incident beam direction. The small solid angle of detection allows transmission measurement close to the in-line transmission condition.

3.3 Results and Discussion

To achieve transparency in AlN ceramics with small grain sizes, fine-grained AlN powder with low concentrations of impurities is necessary as the starting material for ceramic fabrication. Due to the lack of commercially available AlN powder satisfying these qualities as well as powder degradation concerns (difficulty of avoiding oxidation in nanometric powder), we used a custom-made vertical reactor shown schematically in **Figure 3.2 (b)** to convert commercially available γ-Al_2O_3 powder to AlN nano-powder using NH_3 flow (see experimental procedure). Compared to many reported solid-gas reaction routes synthesizing AlN in horizontal tube furnaces similar to **Figure 3.2 (a)**,[37–40] our custom-made reactor shown in **Figure 3.2 (b)** is designed to promote improved solid-gas contact. In conventional horizontal tube furnaces, the supply of NH_3 gas to γ-Al_2O_3 powder pile is primarily diffusion driven, which may cause inefficient powder conversion under the powder pile.[41] In our custom reactor, NH_3 gas flows through the precursor oxide powder, therefore enhancing the supply of NH_3, the removal of gaseous product (water vapor) and the solid-gas contact, allowing us to effectively convert γ-Al_2O_3 to AlN nano-powder at a temperature as low as 1150°C.

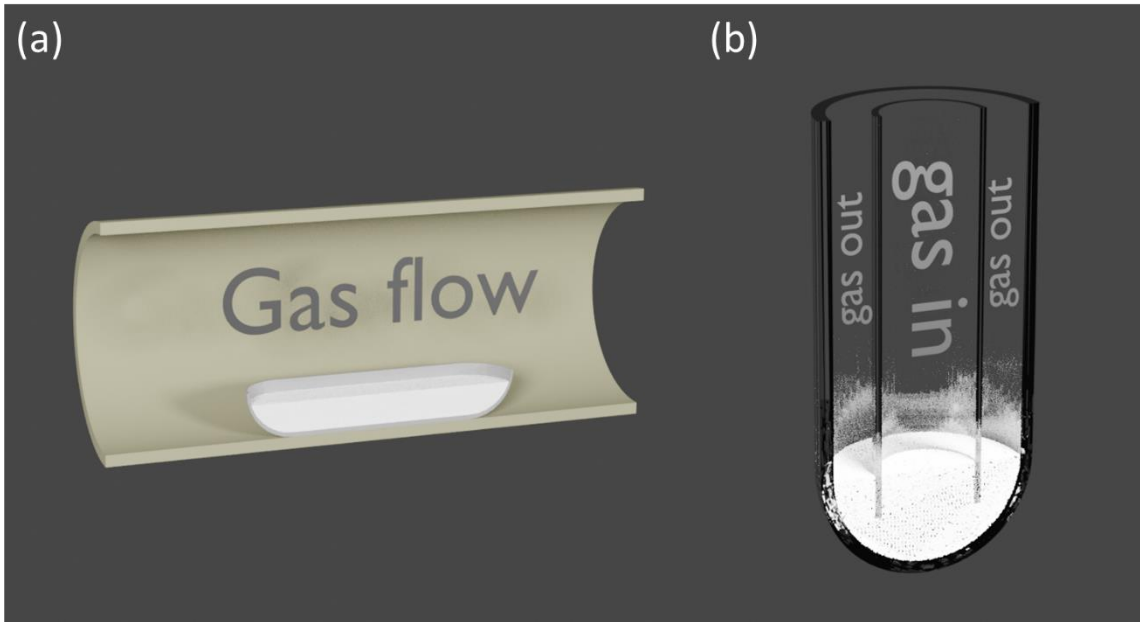

Figure 3.2 Powder-gas reactor schematics for (a) conventional horizontal tube furnace setup, and (b) custom made vertical reactor setup.

Furthermore, γ-Al_2O_3 and NH_3 were the only involved reagent in our reaction without any carbon source. Many reported AlN powder synthesis routes including the well-known carbothermal reduction nitridation (CRN) method involve the addition of carbon sources such as carbon powder or propane gas to thermodynamically enhance the AlN conversion.[37,38,40,42] This often requires further oxidation to remove carbon residue in AlN product powder.[42] However, the oxidation step can once again introduce oxygen impurity as AlN nanopowder is highly susceptible to oxidation and surface adsorption because of the high surface area. Since our goal is to improve ceramics' transparency, the reaction route without any carbon involvement is ideal to avoid carbon contamination which may cause deleterious light absorption, reducing optical transparency. An additional advantage is to provide a simpler route to synthesize AlN nanopowder with fewer processing steps.

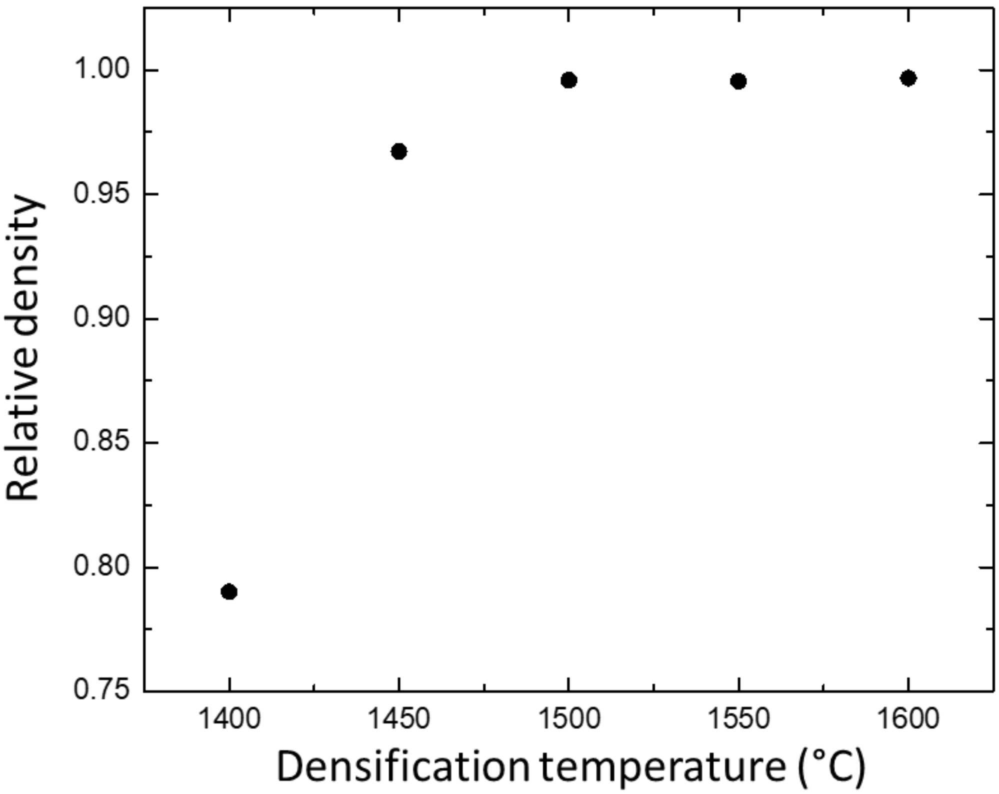

Figure 3.3 Densification temperature dependence of bulk AlN ceramic densities.

To achieve fully dense AlN ceramic while maintaining nanocrystallinity, AlN nanopowder was densified using CAPAD. **Figure 3.3** shows densities of the bulk ceramics densified at different temperatures with a holding time of 10 min. Below 1500°C, the bulk ceramic density increases as densification temperature increases, as expected. Above 1500°C, fully dense ceramics were achieved with densities >99.5%. This densification temperature is over 300°C lower than that of most polycrystalline AlN ceramic works,[15,28,29,43] allowing us to preserve the nanocrystallinity in the bulk AlN ceramic. This low densification temperature is especially impressive considering no sintering/densification additive was added.

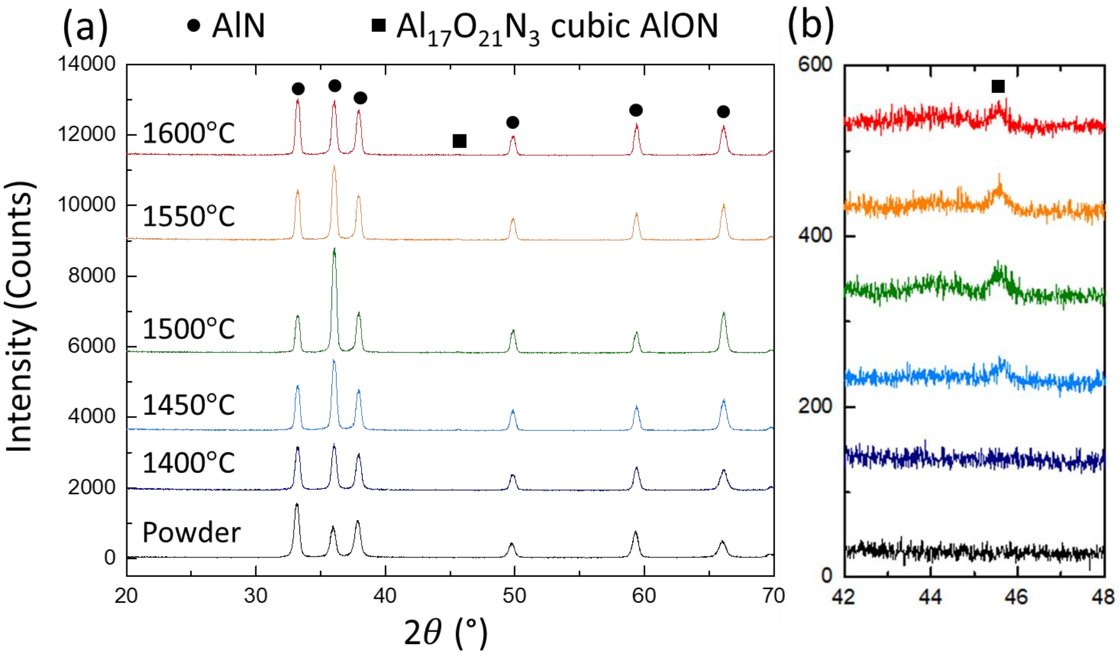

Figure 3.4 (a) X-Ray diffraction patterns of synthesized powder and bulk ceramics densified at 1400°C, 1450°C, 1500°C, 1550°C, and 1600°C. (b) zoomed-in view of 42-48° for more detailed view of AlON phase.

To confirm the phase composition of AlN ceramics, X-ray diffraction patterns of powders before densification and ceramics after densification are scanned and shown in **Figure 3.4**. Only peaks corresponding to the AlN phase can be identified in the converted powder. The majority of the peaks in the XRD patterns of the densified bulk ceramics can be attributed to the AlN phase, with a very minor peak for AlON secondary phase appearing above 1450°C, indicating the formation of AlON phase at higher densification temperatures. The AlON peak observed corresponds to the cubic AlON phase with Al, O, N ratio close to 17:21:3. $Al_{2.85}O_{3.45}N_{0.55}$ (ICSD collection code #70032) was used as a reference for this AlON phase (note that $Al_{2.81}O_{3.56}N_{0.44}$ ICSD #70033 and $Al_{2.78}O_{3.65}N_{0.35}$ ICSD #70034 both have very similar structures). First and second major peaks of AlON phase are overshadowed by AlN peaks, therefore the third highest peak around 45.7° was used to identify AlON secondary phase. The AlN peak intensity ratio changes as densification temperature changes, which we suspect might be related to bulk ceramic character. The peak intensity increase for ~36° peak (002) and ~66° peak (103) compared to other peaks suggests possible grain alignment where c axis of the grains are aligned with the CAPAD uniaxial pressure direction.

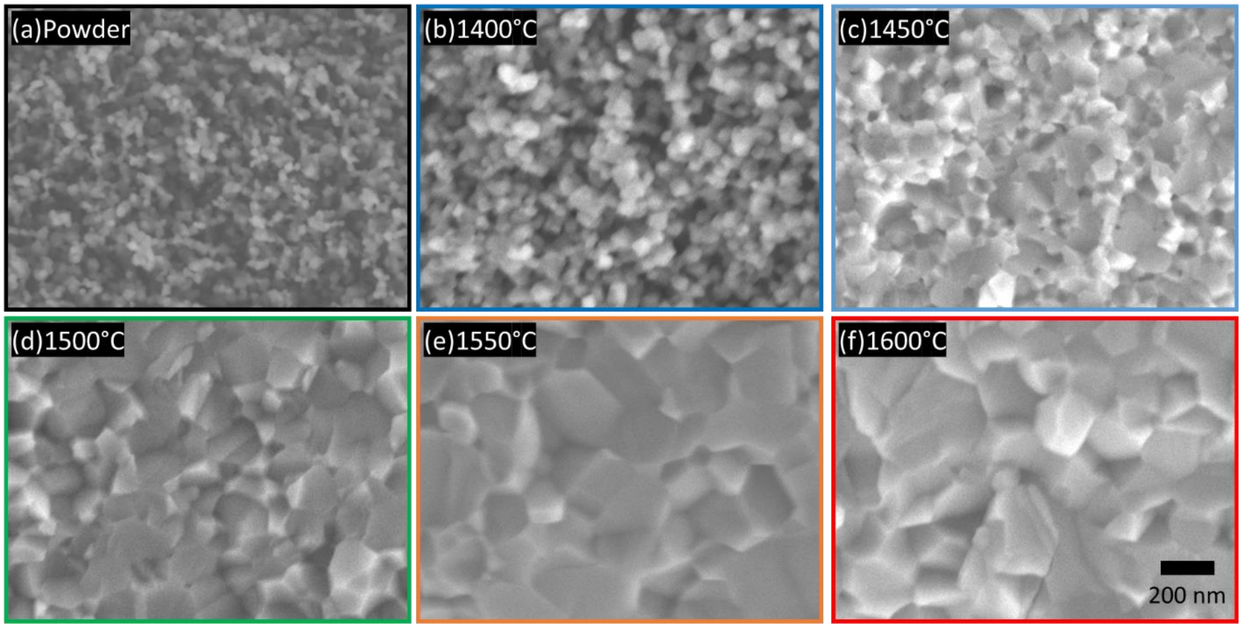

Figure 3.5 SEM micrographs of (a) as converted powder and fracture surfaces of bulk ceramics densified at (b)1400°C, (c)1450°C, (d)1500°C, (e)1550°C, and (f)1600°C.

Figure 3.5 are SEM micrographs showing the representative microstructure of synthesized AlN powder and fracture surfaces of AlN ceramics densified at different temperatures. The AlN powder synthesized showed spherical morphology with a uniform grain size below 50 nm. The ceramics showed clean polycrystalline microstructure with uniform equiaxed grains. Samples densified above 1450°C showed highly dense microstructures with minimal porosity, which agrees with the high densities of the samples. Grain size analysis was carried out over more than 200 grains by measuring the longest diagonal of fully exposed grains. A projected chord length distribution was obtained by measuring more than 600 chords using the straight line intersect method [44] on fracture surface micrographs.

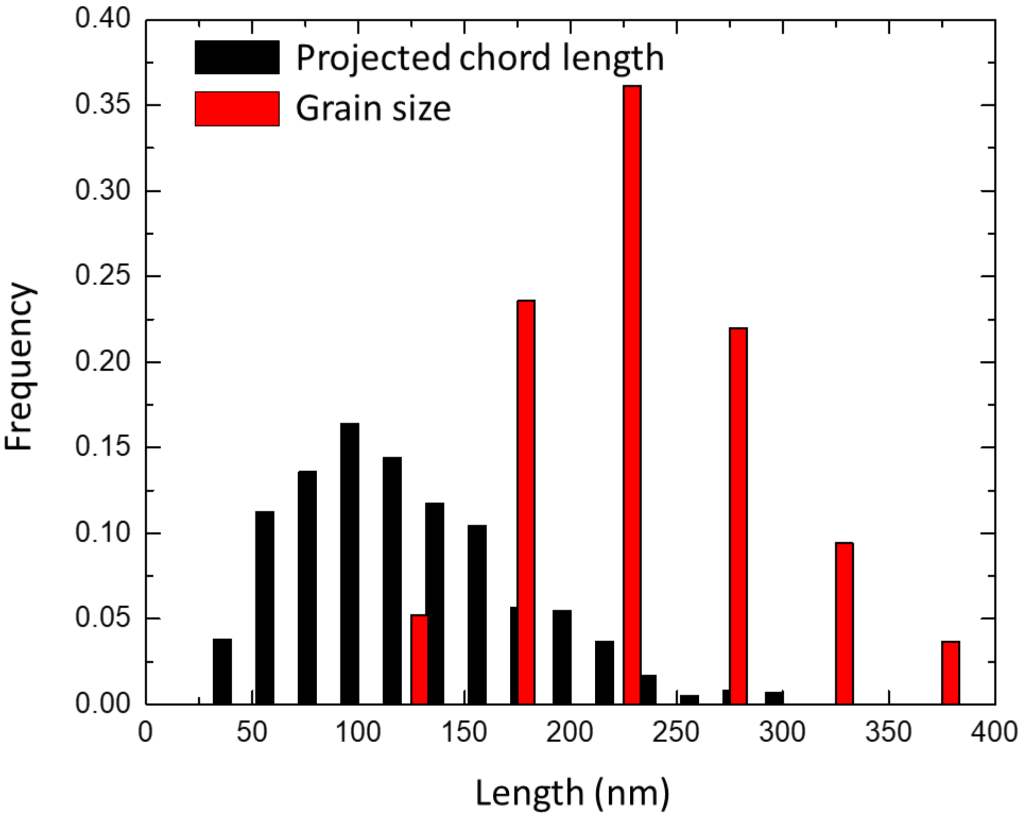

Figure 3.6 Projected chord length distribution and grain size distribution of fully dense 1500°C densified bulk ceramic.

Fracture surfaces were used instead of polished surface for the analysis because clear grain boundaries where exceedingly difficult to identify on finely polished surfaces due to the fine nano-grains of the AlN ceramics. Traditional thermal etching and chemical etching processes do not help in exposing grain boundaries without also changing the microstructure. The projected chord length and grain size distribution of the 1500°C densified sample is shown in **Figure 3.6**. The average grain size was measured to be 230 nm with a standard deviation of 60 nm. The average projected chord length was measured to be 125 nm with a standard deviation of 50 nm. To the best of our knowledge the average grain size of our fully dense 1500°C densified AlN ceramic is nearly one order of magnitude smaller than the finest grained transparent/translucent AlN polycrystalline ceramics [15, 29, 32] reported. As discussed above, small grain size and low porosity are the keys to achieving high in-line light transmission in AlN ceramics which we will discuss subsequently.

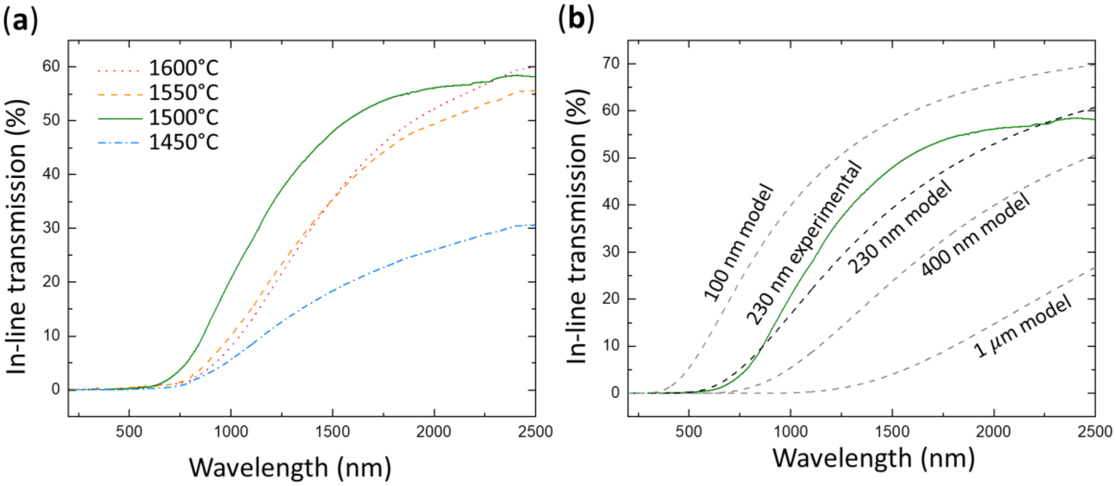

Figure 3.7 In-line transmission normalized to 0.5 mm thickness of (a) bulk ceramics densified at 1450°C, 1500°C, 1550°C, and 1600°C; (b) 1500°C bulk ceramic with 230 nm measured average grain size compared with predictions with various grain sizes using the Apetz and Van Bruggen model for light scattering.

Figure 3.7 (a) shows the in-line transmission of the AlN polycrystalline ceramics normalized to 0.5 mm thickness as a function of wavelength, λ (200 nm – 2500 nm wavelength range). Normalization was done by adjusting the thickness , l of the sample from actual thickness to 0.5 mm based on the Beer-Lambert law as follows:

$$RIT(\lambda) = (1 - R)e^{-\alpha l} \tag{7}$$

where RIT is the real in-line transmission, R is reflection loss from two surface reflection loss $R = 2\left(\frac{n-1}{n+1}\right)^2 - \left(\frac{n-1}{n+1}\right)^4$ following Fresnel equations, n is the refractive index of the sample, and α is loss coefficient. Correction terms considering further reflections on reflected light is ignored because it is less than 0.5% correction for our analysis.[45] The in-line transmission data show that the samples are more transparent in the NIR wavelength range, which agrees with the ceramic scattering models predicting that scattering becomes less effective as wavelength increases.[1,45] The in-line transmission of AlN ceramics densified over 1500 °C reach over 55% at 2.5 μm. This is the most transparent AlN ceramic in NIR wavelength range reported to the best of our knowledge.

The drastic effect of processing temperature on the wavelength dependent transmission (**Figure 3.7 (a)**) can be explained by differences in the resulting microstructure**.** As the densification temperature increases from 1450°C to 1500°C, transparency of the bulk AlN improves dramatically. As shown in **Figure 3.3**, the 1450°C sample contains about 3% porosity, which is a major scattering source that lowers the transparency of the sample. It is worth noting that the grain size and the pore size in the 1450°C sample is extremely fine for a polycrystalline AlN ceramic as shown in **Figure 3.5 (c)**, therefore it still showed decent transparency in the NIR wavelength range despite the relatively high (3%) residual porosity. Increasing the densification temperature from 1450°C to 1500°C greatly reduced the remaining porosity, therefore improving the sample transparency, even though the pore removal is accompanied by some grain growth. The sample produced at 1500°C has the highest overall transparency.

As the densification temperature is increased from 1500°C to 1550°C and 1600°C, the highest transparency (at λ = 2500 nm) remains relatively constant however the shape of the curves changes substantially. This change in wavelength dependence could be explained by changes in microstructure changing the relative importance of operative scattering mechanisms. When raising the densification temperature from 1500°C to 1600°C, the ceramics have clear grain growth while pore removal is not significant, since the samples already have very low porosity as shown in **Figure 3.3** and **Figure 3.5 (d), (e), (f)**. The larger grain sizes in 1550°C and 1600°C samples increase birefringent scattering loss,[25] therefore exhibiting lower transparency at low wavelengths compared to the 1500°C sample.

Since the main scattering loss in our high density, anisotropic samples can be attributed birefringent scattering, it is interesting to compare our results with a theoretical model that has been shown to capture birefringent scattering in fine grain polycrystalline ceramics. **Figure 3.7 (b)** shows in-line transmission of the highest transparency sample, (1500°C) nanocrystalline AlN ceramic compared with model predictions with different grain sizes using the scattering model developed for polycrystalline alumina by Apetz and Van Bruggen [1]

$$RIT(\lambda) = (1 - R)e^{-\frac{3\pi^2 r \Delta n^2 l}{\lambda^2}} \tag{8}$$

where r is half the average grain size, Δn is the average birefringence over all grain orientations. A $\Delta n = (2/3)\Delta n_{max} = 0.03$, ($\Delta n_{max} = |n_e - n_o|$ is the absolute birefringence of the material) was used as a first order approximation assuming random grain orientation distribution following the Apetz-Van Bruggen approach. An *r* =50 nm, 115 nm, 200 nm, and 500 nm was used to model grain sizes of 100 nm, 230 nm, 400 nm, and 1 μm in calculations in order to capture the effect of varying grain sizes and to analyze the effect of different size grains within our AlN. The calculations show that the overall transmission increases as grain size decreases as expected. Model prediction for 1 μm grain size ceramic shows <30% transmission at wavelength λ = 2500 nm and <5% for wavelength below 1500 nm. This reemphasizes the discussion earlier that fine grain size below 1 μm is crucial for achieving optical transparency in polycrystalline AlN ceramics. The in-line transmission of our AlN ceramic with an average grain size of 230 nm shown in **Figure 3.6** agreed relatively well with 230 nm model prediction and substantially outperformed model predictions for 1 μm and 400 nm. The largest grain sizes we measured were ~ 400 nm (see **Figure 3.6**) and although there are relatively few of these grains, these should be the most efficient scatterers. Thus, it is interesting that the transmission is nearly 100% higher than that of the 400 nm calculation around the wavelength, λ = 1500 nm. More noteworthy is that the transmission is ~20 % higher at λ = 1500 nm than the calculated for the correct average grain size, 230 nm. Since the model we used developed by Apetz and Van Bruggen only takes surface reflection and birefringent scattering loss into consideration, it is expected that in-line transmission measured on our sample should be no higher than model prediction since absorption loss from impurities and scattering loss from pores (not accounted for by the model) may contribute to more optical loss in our AlN samples.

We believe there are two possible reasons for the discrepancy in the model and measurement. As mentioned earlier, this model was developed and validated for dense fine-grained alumina. The model assumes a RGD scattering giving a λ^{-2} transmission dependence. Examination of the calculated and measured curves reveals a clear difference in wavelength dependence. It is probable that other scattering types such as Rayleigh-like scattering and light absorption [45] need to be considered as well. Another consideration is that the possible grain alignment in our AlN ceramic discussed earlier makes it more probable for grains to have similar orientations, thus effectively reducing Δn. A smaller effective Δn could cause less birefringent scattering, therefore allowing higher in-line transmittance than the model prediction. Despite the discrepancies we believe that comparison to the well-known and often used Apetz-Van Bruggen model is instrumental for discussion because it shows that high transmission is achievable at grain sizes larger than perhaps conventionally expected—even in nitride ceramics with relatively high birefringence.

The high transparency of our AlN nanocrystalline ceramics shows that transparency in ceramics of birefringent materials is not limited to small Δn materials such as Al_2O_3. With controlled microstructures, larger Δn materials like AlN or even composites with very close refractive indices can be considered for optically transparent applications.

3.4 Chapter 3 Summary and Conclusion

We produced optically and NIR transparent AlN nanocrystalline ceramics with CAPAD using AlN nanopowder converted from γ-Al_2O_3 in a custom-made reaction apparatus that allowed production powder at very low temperatures preserving the very fine grain size. Full density was achieved with CAPAD densification above 1500°C in 10 min. At optimized powder densification condition, fully dense ceramic with an average grain size of 230 nm was achieved, which showed an in-line transmission of over 55% at 2.5 μm. This grain size is significantly smaller than previous transparent AlN ceramic works reported, allowing a more than twofold improvement for NIR transparency. This shows the possibility of achieving transparent ceramics with AlN and potentially other highly birefringent materials by reducing the grain size.

Chapter 3, in full, is co-authored with Dr. Y. Kodera and Dr. J. E. Garay, and has been submitted for publication of the material as it may appear in Materials and Design. The dissertation author was the primary investigator and author of this paper.

3.5 Chapter 3 References

1 R. Apetz, M. P. B. Van Bruggen, J. Am. Ceram. Soc. 86, 480 (2003).

2 L. M. Goldman, R. Twedt, S. Balasubramanian, S. Sastri, Window and Dome Technologies and Materials XII, Proc SPIE 8016, 801608 (2011).

3 J. W. McCauley, P. Patel, M. Chen, G. Gilde, E. Strassburger, B. Paliwal, K. T. Ramesh, D. P. Dandekar, J. Euro. Ceram. Soc. 29, 223 (2009).

4 M. Grujicic, W. C. Bell, B. Pandurangan, Mater. Des, 34, 808 (2012).

5 A. Krell, J. Klimke, T. Hutzler, J. Euro. Ceram. Soc. 29, 275 (2009).

6 A. Ikesue, Y. L. Aung, J. Euro. Ceram. Soc. 40, 2432 (2020).

7 A. Ikesue, Y. L. Aung, Nat. Photonics 2, 721 (2008).

8 A. Ikesue, Y. L. Aung, T. Taira, T. Kamimura, K. Yoshida, G. L. Messing, Annu. Rev. Mater. Res. 36, 397 (2006).

9 A. T. Wieg, E. H. Penilla, C. L. Hardin, Y. Kodera, J. E. Garay, APL Mater. 4, 126105 (2016),

10 A. D. Dupuy, Y. Kodera, J. E. Garay, Adv. Mater. 28, 7970 (2016).

11 G. A. Slack, R. A. Tanzilli, R. O. Pohl, J. W. Vandersande, J. Phys. Chem. Solids 48, 641 (1987).

12 A. T. Wieg, Y. Kodera, Z. Wang, C. Dames, J. E. Garay, Acta Mater. 86, 148 (2015).

13 E. H. Penilla, L. F. Devia-Cruz, M. A. Duarte, C. L. Hardin, Y. Kodera, J. E. Garay, Light Sci. Appl. 7 (2018).

14 W. M. Yim, E. J. Stofko, P. J. Zanzucchi, J. I. Pankove, M. Ettenberg, S. L. Gilbert, J. Appl. Phys. 44, 292 (1973).

15 Y. Xiong, Z. Fu, Y. Wang, F. Quan, J. Mater. Sci. 41, 2537 (2006).

16 J. F. Shackelford, W. Alexander, CRC Material Science and Engineering Handbook 2001

17 D. C. Harris, L. F. Johnson, R. Seaver, T. Lewis, G. Turri, M. A. Bass, D. E. Zelmon, N. Haynes, Optical Engineering 52, 087113 (2013).

18 A. Ikesue, I. Furusato, K. Kamata, J. Am. Ceram. Soc. 78, 225 (1995).

19 L. Mezeix, D. J. Green Int. J. Appl. Ceram. Technol. 3, 166 (2006).

20 M. Ding, S. Robertson, T. Wang, L. Fan, Z. Sun, B. Maerz, R. Crookes, J. Xie, Y. Shi, H. Wu, J. Am. Ceram. Soc. 102, 6433 (2019).

21 F. Dahmani, J. C. Lambropoulos, A. W. Schmid, S. J. Burns, C. Pratt, J. Mater. Sci. 33, 4677 (1998).

22 Kh. S. Bagdasarov, N. B. Bolotina, V. I. Kalinin, V. F. Karyagin, B. V. Kuz'min, L. A. Muradyan, S. N. Ryadnov, E. M. Uyukin, T. S. Chernaya, E. A. Fedorov, V. S. Chudakov, V. I. Simonov, Kristallografiya 36, 715 (1991).

23 H. X. Willems, G. de With, R. Metselaar, R. B. Helmholdt, K. K. Petersen, J. Mater. Sci. Lett. 12, 1470 (1993).

24 Corning, High Purity Fused Silica Product information, 2015

25 X. Wu, L. Tang, C. L. Hardin, C. Dames, Y. Kodera, and J. E. Garay, J. Appl. Phys. 131, 020902 (2022).

26 J. Li, M. Nakamura, T. Shirai, K. Matsumaru, C. Ishizaki, K.Ishizaki, J. Am. Ceram. Soc. 89, 937-943 (2006)

27 L. D. Merkle, A. C. Sutorik, T. Sanamyan, L. K. Hussey, G. Gilde, C. Cooper, M. Dubinskii, Opt. Mater. Express 2, 78 (2012).

28 H. W. Son, B. N. Kim, T. S. Suzuki, Y. Suzuki, J. Am. Ceram. Soc. 101, 4430 (2018).

29 M. Xiang, Y. Zhou, W. Xu, X. Li, K. Wang, W. Pan, J. Ceram. Soc. Japan 126, 241 (2018).

30 A. T. Wieg, M. J. Grossnickle, Y. Kodera, N. M. Gabor, J. E. Garay, Appl. Phys. Lett. 109, 121901 (2016).

31 A. T. Wieg, Y. Kodera, Z. Wang, T. Imai, C. Dames, J. E. Garay, Appl. Phys. Lett. 101, 111903 (2012).

32 T. Wang, J. Xie, C. Chen, J. Fang, Y. Shi, Opt. Mater.: X 14, 100148 (2022).

33 X. Du, M. Qin, A. Rauf, Z. Yuan, B. Yang, X. Qu, Mater. Sci. Eng. A 496, 269 (2008).

34 Z. Han, M. Yang, H. Zhu, Mater. Res. Soc. Symp. Proc. 1040, Q09–Q21 (2008).

35 M. A. Duarte, V. Mishra, C. Dames, Y. Kodera, J.E. Garay, Materials 14, 5565 (2021).

36 J. E. Garay, Annu. Rev. Mater. Res. 40, 445 (2010).

37 T. Suehiro, N. Hirosaki, K. Komeya, Nanotechnology 14, 487 (2003).

38 T. Suehiro, N. Hirosaki, R. Terao, J. Tatami, T. Meguro, K. Komeya, J. Am. Ceram. Soc. 86, 1046 (2003).

39 Q. Zhang, L. Gao, J. Am. Ceram. Soc. 89, 415 (2006).

40 T. Yamakawa, J. Tatami, T. Wakihara, K. Komeya, T. Meguro, K. J. D. MacKenzie, S. Takagi, M. Yokouchi, J. Am. Ceram. Soc. 89, 171 (2006).

41 M. Duarte, UC Riverside Electronic Theses and Dissertations, 2016.

42 M. Xiang, Y. Zhou, W. Xu, D. Huang, K. Wang, W. Pan, J. Am. Ceram. Soc. 100, 2482 (2017).

43 Z. Y. Fu, J. F. Liu, H. Wang, D. H. He, Q. J. Zhang, Mater. Sci. Technol. 20, 1097 (2004).

44 J. C. Wurst, J. A. Nelson, J. Am. Ceram. Soc. 55, 109 (1972).

45 M. H. Shachar, G. Uahengo, E. H. Penilla, Y. Kodera, J. E. Garay, J. Appl. Phys. 128, 083103 (2020).

4. INCORPORATION OF THULIUM INTO NANOCRYSTALLINE ALUMINUM NITRIDE

4.1 Introduction

When choosing materials for many light emitting applications, single crystal oxide materials have been the material of choice for decades.[1] With recent development in ceramic densification and sintering technologies, researchers produced polycrystalline oxide ceramics with optical, thermal and mechanical properties that are comparable or even superior to their single crystal counterparts.[1-3] However, the fundamentally limited intrinsic thermal conductivities of commonly used oxide materials limit their high-power performance as temperature gradient build-up almost always negatively affect light transmitting/emitting performance and may eventually lead to thermal fracture.[4, 5]

To overcome this challenge, materials with higher intrinsic thermal conductivity is desired. One promising candidate is aluminum nitride (AlN) with its excellent intrinsic thermal conductivity of 320 $Wm^{-1}K^{-1}$,[6] which is one order of magnitude higher than yttrium aluminum garnet (YAG), alumina, spinel, and two orders of magnitude higher than glass.[1] The wide bandgap (6.2 eV)[7] of AlN combined with its infrared cutoff gives it a wide transparency range, making it suitable for light emitting applications across visible and NIR wavelength ranges if doped with rare earth ions.

However, incorporation of rare earth ions into AlN lattice is challenging because of the low equilibrium solubility of RE ions in AlN.[8] When doping AlN, RE dopants substitute Al^{3+} and stay on Al sites. However, RE ions have much bigger ionic radii than Al^{3+}, therefore making it energetically unfavorable for RE to stay in AlN lattice. To address this challenge, it has been proposed and demonstrated in Al_2O_3 that polycrystalline ceramics with nanometric grain sizes have much higher grain boundary volume compared to single crystals, therefore effectively disperse dopant ions at the grain boundary in addition to dopant ions that stays in the lattice.

Recently, incorporation of Tb^{3+}, Nd^{3+}, Ce^{3+}, Er^{3+} and Eu^{3+} into AlN ceramics were reported [8-12] and non-equilibrium doping approach of RE ions into AlN was proposed [8] to minimize RE segregation during the ceramic densification process. The reported RE doped AlN works have grain sizes in the micrometer range. As discussed above, fine, nanometric grain size is desired for RE doping as well as transparency (see **Sec. 1.2.2**), bringing interest to further reducing the grain size of RE doped AlN.

Here we present incorporation of thulium into lab synthesized, nanocrystalline AlN powder using the synthesis route described in **Sec. 3.2.1**, as well as densification of Tm incorporated AlN ceramics using current activated pressure assisted densification (CAPAD, also known as Spark Plasma Sintering, SPS, and Field Assisted Sintering, FAST).[13] The fine grain size of lab synthesized AlN powder combined with the fast densification process enables the fine grain size in Tm incorporated AlN produced. To the best of our knowledge, this is the first time thulium incorporation into AlN bulk ceramics has been reported. This is also the first time RE incorporation into nanocrystalline AlN ceramics has been reported.

4.2 Experimental procedure

4.2.1 Powder Preparation

AlN nano-powder was synthesized using the same approach described in Chapter 3 by converting commercially available γ-Al_2O_3 (99.99% purity, Inframat, Advanced Materials) in NH_3 (Praxair Ammonia 5.0 Research Grade 99.999% purity) flow using a custom-made reactor. The reactor consists of an open-ended inner tube (O.D. 12.7 mm, I.D. 10.5 mm) made of alumina

(Advalue Technology) inside a closed-ended outer tube (O.D 25 mm, I.D. 22 mm) made of fused quartz (Advalue Technology), with stainless steel and aluminum fittings. During nitridation reaction, NH_3 gas flows downward through the inner tube and then upward between the inner tube and outer tube towards the exhaust. 0.33 g of starting γ-Al_2O_3 precursor powder was placed at the bottom of the outer tube, covering the bottom opening of the inner tube. The reactor was then placed in a vertically positioned furnace (MELLEN model SC12-3X12). The reaction temperature was between 1150°C, with a heating rate of 5°C/min. The reaction was held at the holding temperature for 24 hours. 250 cm^3/min of N_2 gas was supplied to purge the reactor under 200°C, then 250 cm^3/min of NH_3 flow was supplied during heating and holding. After the reaction was complete, the reactor was sealed during cooling and then transferred into an Ar filled glove box for further processing.

Lab converted AlN was first doped with Tm_2O_3 (99.9% purity, Sigma Aldrich, USA) at a doping level of 5 at.% (cation ratio Tm^{3+}/Al^{3+}) to form an intermediate dopant. The intermediate dopant was mixed through different processes involving hand mixing using a mortar and pestle in dry condition for 20 min, and the mentioned processed combined with planetary ball milling in dry condition using Si_3N_4 milling media at 450 RPM for 3 hour with a powder: ball weight ratio of 1:10. Prepared 5 at.% intermediate dopant was further mixed with lab converted undoped AlN powder at a doping level of 0.25 at.% (cation ratio Tm^{3+}/Al^{3+}). The same mixing processes mentioned above were used for this secondary mixing step. After 0.25 at% (cation ratio Tm^{3+}/Al^{3+}) powder was mixed, it was collected in an Ar filled glove box and stored dry until further densification.

4.2.2 CAPAD Processing

The powders were densified by CAPAD (also referred to as SPS and FAST) in a graphite die (19 mm outer and 10 mm inner diameter). The graphite die and plunger set is placed inside a larger graphite die set (19 mm inner diameter). The large die and plunger set (19 mm inner diameter) were then placed into the CAPAD and a vacuum of 3×10^{-2} torr was achieved. The powders were pre-pressed under a pressure of 100 MPa for 5 min. The final densification involves a pressure of 100 MPa with a pressure ramp of 33.3 MPa/min. At the same time, the sample was heated at a heating rate of 200-300 °C/min and held at a holding temperature of 1500°C with a holding time of 10 min. Sample temperature was monitored using a dual wavelength optical pyrometer (Infrared thermometer IR-CZ, CHINO) focused on a hole at the midpoint of the outer larger graphite die.

4.2.3 Microstructural Characterization

The powders and densified ceramics were characterized on a PANalytical X'Pert Diffractometer (PANalytical, Almelo, The Netherlands) using Cu Kα (λ = 1.541 Å) radiation with a step size of $2\theta = 0.01°$. Published standards were used for comparison: AlN (ICSD coll#:34475), $Al_{2.85}O_{3.45}N_{0.55}$ (ICSD coll#:70032). The microstructure of powders and densified ceramics were tested with a Zeiss Sigma 500 scanning electron microscope.

4.2.4 Photoluminescence Measurements

Photoluminescence was measured on a Horiba Spectrophotometer using a pulsed laser from a Horizon Optical parametric oscillator (Continuum, USA) pumped by a Surelite nanosecond pulsed laser (Continuum, USA) as excitation light source. Samples were set in front face mode with incident angle of 45°. Emission scans were taken between 1550 nm and 2100 nm with an integration time of 1s/nm.

4.3 Results and discussions

Lab converted AlN powder and commercial Tm_2O_3 powder were mixed before densification in CAPAD (see **Sec. 4.2**). To better disperse Tm_2O_3 dopant in AlN powder, different mixing approaches were tested to investigate their effect on powder mixing. **Figure 4.1** shows SEM micrographs of lab converted AlN and commercial Tm_2O_3 starting powders and mixed powders after different mixing approaches. As shown in **Figure 4.1 (a)**, lab converted AlN powder showed uniaxial morphology with grain size below 50 nm. **Figure 4.1 (b)** shows the commercial

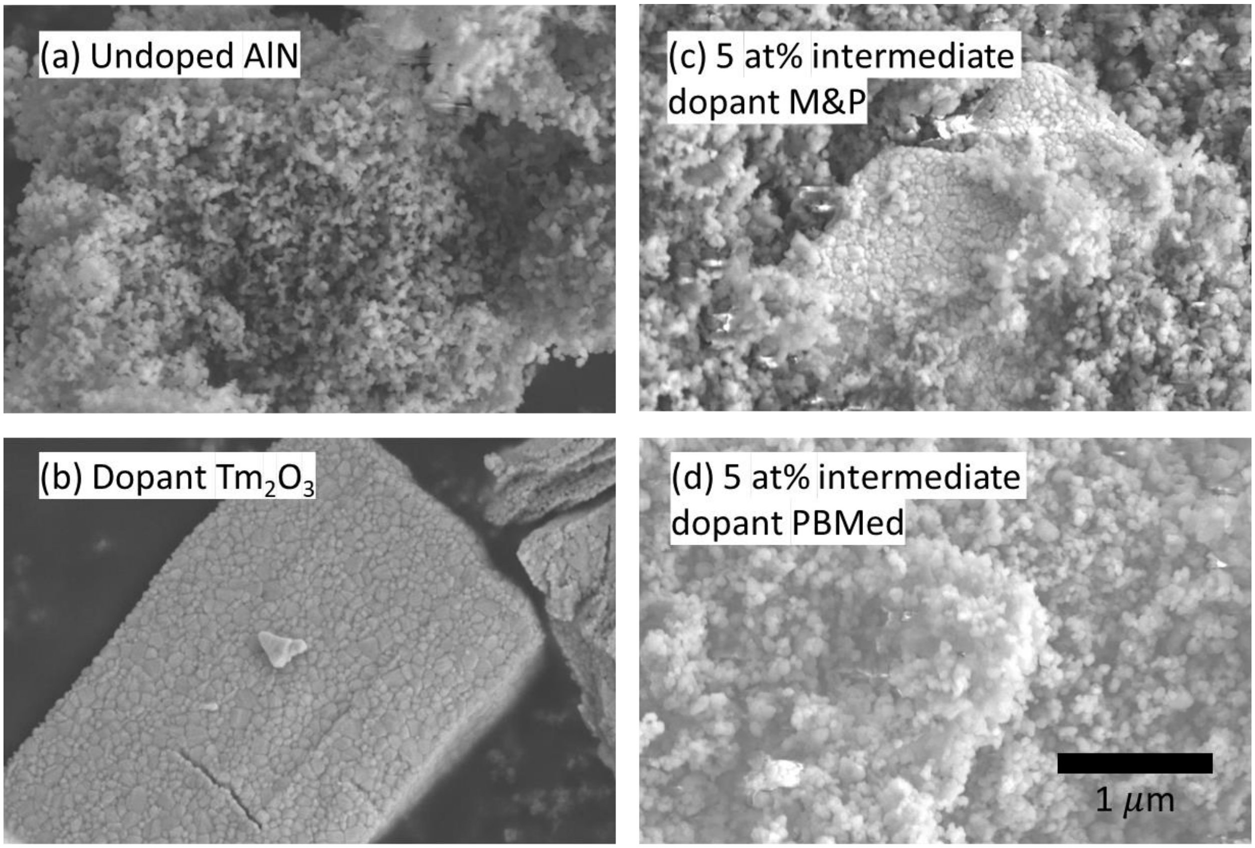

Figure 4.1 SEM micrographs of (a) as converted AlN powder, (b) as received commercial Tm_2O_3 powder, (c) 5 at.% (Tm/Al ratio) Tm_2O_3 mixed with AlN powder using mortar and pestle only, and (d) 5 at.% (Tm/Al ratio) Tm_2O_3 mixed with AlN powder using mortar and pestle followed by planetary ball milling.

Tm_2O_3 powder has grain size around 100 nm and are agglomerated. The Tm_2O_3 grains are closely packed together, suggesting good bonding between the grains. The morphology of Tm_2O_3 starting powder posed a challenge for uniform mixing since the agglomerated Tm_2O_3 crystallites may hinder the dispersion of Tm_2O_3 dopant into AlN.

Figure 4.1 (c) shows characteristic morphology of 5 at.% (Tm/Al ratio) Tm_2O_3 mixed with AlN powder using mortar and pestle. An agglomerated particle showing similar morphology to that of Tm_2O_3 starting powder is mixed into more loosely packed AlN powder (with which the majority of the 5 at.% intermediate dopant consists of). As shown in **Figure 4.1 (d)**, 5 at.% (Tm/Al ratio) Tm_2O_3 mixed with AlN powder using mortar and pestle followed by planetary ball milling (PBM) showed much more uniform mixing between the two powders. Agglomerated particles of Tm_2O_3 were not found in the planetary ball milled powder.

We believe that mortar and pestle resulted in limited particle breaking and mixing between Tm_2O_3 and AlN powder. The agglomerated Tm_2O_3 particles were broken into smaller particles that have micrometer particle size and mixed into AlN powder. With further PBM mixing steps, however, the agglomerated Tm_2O_3 particles were broken into much smaller particles and the mixing between the two starting powders is significantly improved.

Effect of different mixing approach is further studied on bulk ceramics. The processed powders were densified in CAPAD under the same condition. **Figure 4.2** shows polished surface and fracture surface microstructure of bulk ceramics densified from powders using three different mixing approaches. All three ceramics have fine grain sizes well below 1 μm as shown in the fracture surfaces **Figure 4.2 (c)**, **(f)**, and **(i)**.

Figure 4.2 (a), **(b)** shows the microstructure of a bulk ceramic sample densified from 0.25 at.% Tm_2O_3 doped AlN powder using only mortar and pestle mixing approach. **Figure 4.2 (d)**, **(e)**

shows the microstructure of a bulk ceramic sample densified from 0.25 at.% Tm_2O_3 doped AlN powder for which a 5 at.% Tm_2O_3 doped AlN intermediate dopant was first mixed using mortar and pestle followed by planetary ball milling, before mixed with AlN powder via mortar and pestle to form the 0.25 at.% Tm_2O_3 doped AlN powder. **Figure 4.2 (g)**, **(h)** shows the microstructure of a bulk ceramic sample densified from 0.25 at.% Tm_2O_3 doped AlN powder which was formed using the same mixing approach for **Figure 4.2 (d)**, **(e)**, followed by planetary ball milling.

As shown in **Figure 4.2 (a)**, **(b)**, majority of the polished surface showed as dark regions while certain brighter regions can be observed. We believe the bright regions contain higher concentration of Tm atoms because their higher Z number compared with other expected elements

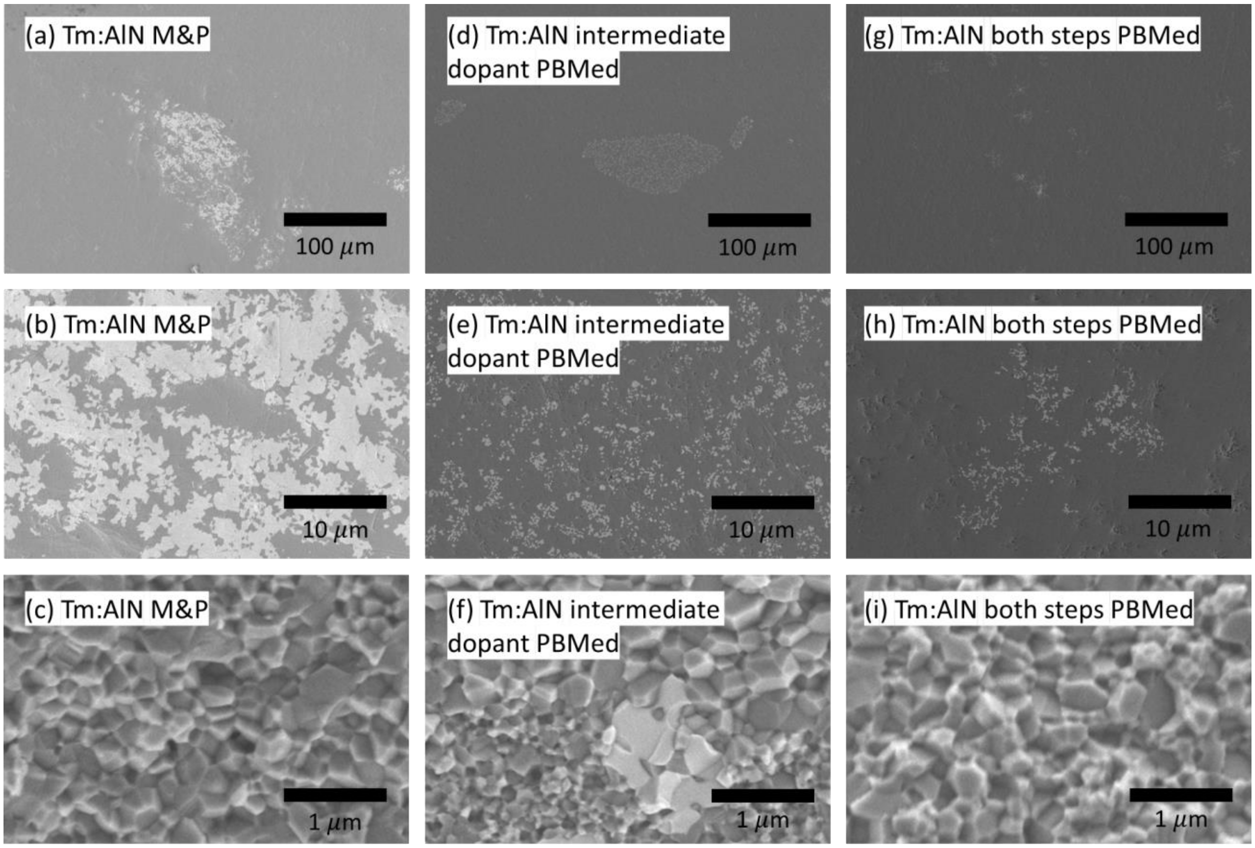

Figure 4.2 SEM micrographs of bulk ceramic samples densified from 0.25 at.% Tm_2O_3 doped AlN powders using different mixing approaches (a, b, d, e, g, h: polished surfaces; c, f, i: fracture surfaces). (a), (b), (c) Mortar and pestle mixing between Tm_2O_3 and AlN. (d), (e), (f) A 5 at.% Tm_2O_3 doped AlN intermediate dopant was first mixed using mortar and pestle followed by planetary ball milling, before mixed with AlN powder via mortar and pestle. (g), (h), (i) The same approach using the 5 at.% intermediate dopant followed by planetary ball milling.

should cause higher intensity under SEM. The bright regions in **Figure 4.2 (a)**, **(b)** show a high degree of segregation which can be explained by the insufficient mixing through mortar and pestle.

Figure 4.2 (d), **(e)** shows that when an additional planetary ball milling step is applied to the 5 at.% intermediate dopant, the mixing between Tm-concentrated regions and the dark regions are significantly improved. The segregated Tm-concentrated bright regions are well below 10 μm as shown in **Figure 4.2 (e)** compared to tens of micrometers in **Figure 4.2 (b)**. However, **Figure 4.2 (d)** shows that the well mixed regions are limited, and the bulk sample is not uniform at lower magnification. This indicates the insufficient mixing between the 5 at.% intermediate dopant and undoped AlN. We believe the brighter regions in **Figure 4.2 (d)** originated from the planetary ball milled 5 at.% intermediate dopant, which is better mixed, while the darker majority in **Figure 4.2 (d)** originated from undoped AlN, which was not sufficiently mixed with the 5 at.% intermediate dopant.

To further improve the mixing between the 5 at.% intermediate dopant and undoped AlN, an additional PBM step was applied. As shown in **Figure 4.2 (g)**, **(h)**, the brighter Tm-concentrated regions are much better dispersed throughout the sample, with small segregated grains shown in **Figure 4.2 (h)** that are similar to those shown in **Figure 4.2 (e)**, but better dispersed across the sample.

Bulk ceramic densities were measured for the three samples and compared with an undoped AlN sample produced under identical densification condition. As shown in **Figure 4.3**, the Tm_2O_3 doped AlN ceramics have higher densities than the undoped AlN sample produced under the same condition. This is expected since both addition of Tm containing phases and substitution of Tm into AlN lattice should increase the density of the ceramics. Comparison between Tm_2O_3 doped AlN ceramics and theoretical densities of undoped AlN and 0.25 at.% Tm_2O_3/AlN composite

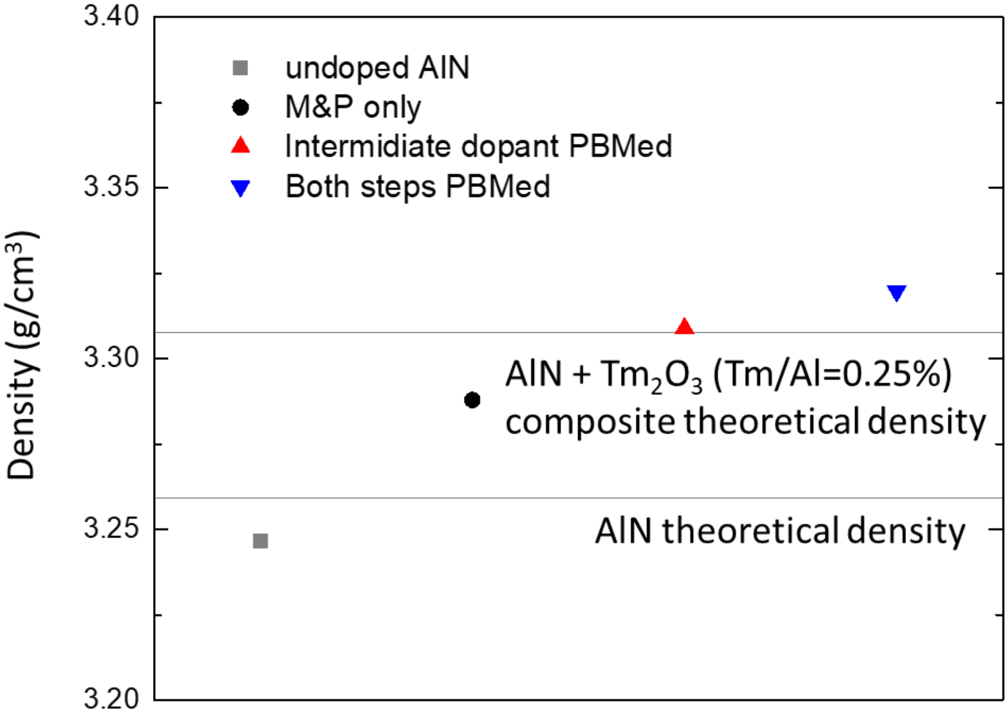

Figure 4.3 Densities of Tm_2O_3 doped AlN ceramics and undoped AlN ceramic compared with theoretical densities of undoped AlN and 0.25 at.% Tm_2O_3/AlN composite.

shows that all three Tm_2O_3 doped AlN ceramics have densities above the theoretical density of undoped AlN, close to theoretical densities of 0.25 at.% Tm_2O_3/AlN composite. This indicates the low residual porosity in the Tm_2O_3 doped AlN ceramics, which agrees with the microstructure observed in **Figure 4.2**.

Figure 4.3 also shows that the densities of ceramics increased as additional PBM steps were applied. The densities of the latter two samples are higher than theoretical density for 0.25 at.% Tm_2O_3/AlN composite. It is possible that additional PBM steps introduced oxygen contamination that increased the sample densities.

Figure 4.4 shows X-ray diffraction measurements for the three Tm_2O_3 doped AlN samples and an undoped AlN sample produced under the same densification condition. All samples consist of mainly AlN phase with a minor AlON secondary phase. **Figure 4.4 (b)** shows the low-intensity peaks of the four samples compared with $Al_{17}O_{21}N_3$ cubic AlON reference. While the major peaks of AlON phase near 37.5° and 66° are overshadowed by AlN peaks, the peaks around 45.5° and 60.5° are clearly detected in all four samples. The AlON peak intensity of the three Tm_2O_3 doped AlN samples are higher than the undoped AlN sample, which can be explained by addition of Tm_2O_3 dopant. The three Tm_2O_3 doped AlN samples showed similar AlON peak intensities with no additional phases detected, showing that different mixing approaches did not affect the phase composition of Tm_2O_3 doped AlN ceramics.

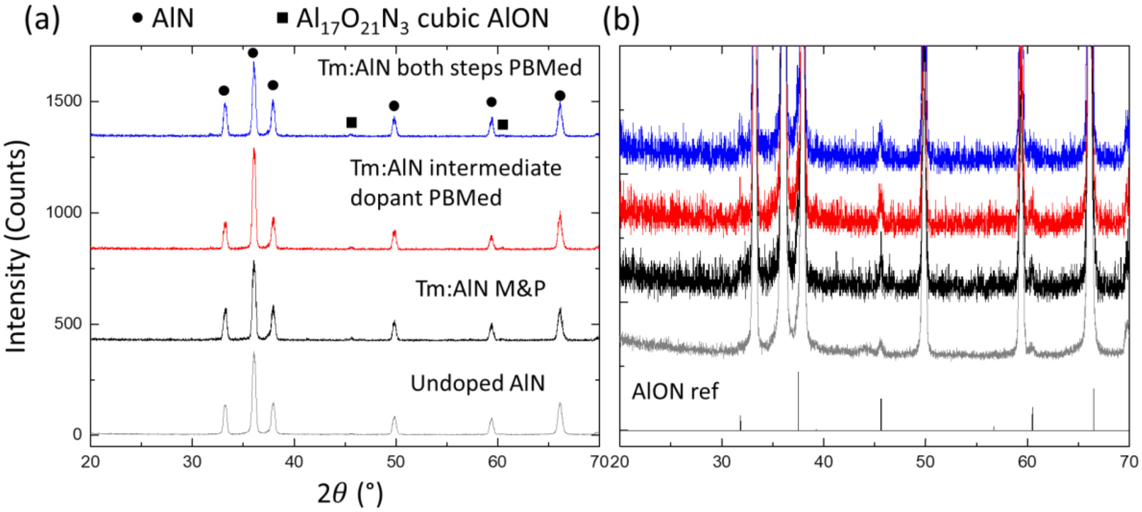

Figure 4.4 (a) X-Ray diffraction patterns of three Tm_2O_3 doped AlN samples using different mixing approaches and an undoped AlN sample, and (b) magnified view for details of low-intensity peaks compared with AlON reference.

Photoluminescence measurements of the three Tm_2O_3 doped AlN samples compared with the undoped AlN sample is shown in **Figure 4.5**. Characteristic emission around 1.75 μm from Tm^{3+} was detected in all three Tm_2O_3 doped AlN samples when excited at 683 nm. The emission around 1.5 μm is likely not Tm dopant related since similar emission was also detected in the undoped AlN ceramic produced under the same condition. The Tm_2O_3 doped AlN ceramics showed wide emission bandwidth similar to that observed in $Tm:Al_2O_3$ ceramics we produced (see

Sec. 2.3). We noticed the Tm_2O_3 doped AlN ceramics with additional PBM mixing steps showed weaker emission as well as darker appearance. We suspect that the oxygen impurities introduced during the additional PBM steps is related to stronger absorption in the samples, therefore reducing the emission intensity of the ceramics.

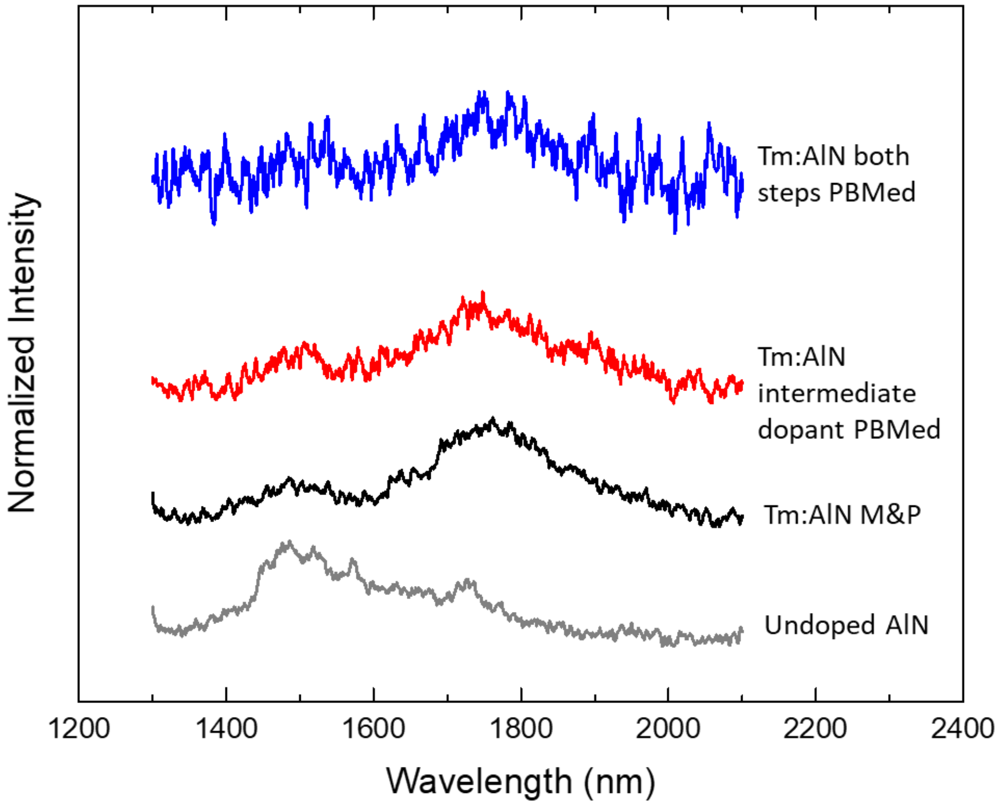

Figure 4.5 Normalized emission spectra of three Tm_2O_3 doped AlN ceramics and the undoped AlN ceramic.

Preliminary transmission measurements on the three Tm_2O_3 doped AlN ceramics showed less than 5% in-line transmission in the visible and NIR wavelength range below 2.5 μm. This transparency is significantly lower than the undoped AlN ceramics produced under similar conditions shown in **Sec. 3.3**. We believe the reduction in transparency is caused by segregated Tm-concentrated grains shown in **Figure 4.3**. As discussed in **Sec. 1.2.1**, the Tm-concentrated grains act as secondary phase, causing optical scattering loss in polycrystalline AlN ceramics because of their different refractive index than the primary AlN phase. The possible absorption loss related to the additional PBM steps discussed above may also contributed to the reduction in transparency.

4.4 Chapter 4 Summary and Conclusion

Incorporation of Tm_2O_3 dopant into lab-synthesized nanocrystalline AlN powder was studied. We produced and characterized the first Tm incorporated AlN polycrystalline ceramic, which is also the first attempt to incorporate rare earth into nanocrystalline AlN. Further improvement in the dopant incorporation approaches is needed to achieve better transparency and photoluminescence performance. This study may serve as a starting point for future attempts to fabricate rare earth incorporated AlN nanocrystalline ceramics for thermal shock resistant photonic applications.

4.5 Chapter 4 References

1 X. Wu, L. Tang, C. L. Hardin, C. Dames, Y. Kodera, and J. E. Garay, J. Appl. Phys. 131, 020902 (2022).

2 A. Ikesue, T. Kinoshita, K. Kamata, and K. Yoshida, J. Am. Ceram. Soc. 78, 1033–1040 (1995).

3 A. Ikesue and Y. L. Aung, J. Eur. Ceram. Soc. 40, 2432–2438 (2020).

4 W. Koechner, Appl. Opt. 9, 2548 (1970).

5 Yu Shen, Wen-bin Liu, Nan Zong, Jiang Li, Yong Bo, Xi-qi Feng, Fang-qin Li, Yu-bai Pan, Ya-ding Guo, Peng-yuan Wang, Wei Tu, Qin-jun Peng, Jing-yuan Zhang, Wenqiang Lei, Da-fu Cui, and Zu-yan Xu, Opt. Lett. 39, 1965 (2014).

6 G. A. Slack, R. A. Tanzilli, R. O. Pohl, J. W. Vandersande, J. Phys. Chem. Solids 48, 641 (1987).

7 W. M. Yim, E. J. Stofko, P. J. Zanzucchi, J. I. Pankove, M. Ettenberg, S. L. Gilbert, J. Appl. Phys. 44, 292 (1973).

8 A. T. Wieg, Y. Kodera, Z. Wang, T. Imai, C. Dames, and J. E. Garay, Appl. Phys. Lett. 101, 111903 (2012).

9 A. T. Wieg, M. J. Grossnickle, Y. Kodera, N. M. Gabor, and J. E. Garay, Appl. Phys. Lett. 109, 121901 (2016).

10 A. T. Wieg, E. H. Penilla, C. L. Hardin, Y. Kodera, and J. E. Garay, APL Mater. 4, 126105 (2016).

11 K. Inoue, N. Hirosaki, R. J. Xie, and T. Takeda, J. Phys. Chem. C 113, 9392–9397 (2009).

12 L. D. Merkle, A. C. Sutorik, T. Sanamyan, L. K. Hussey, G. Gilde, C. Cooper, and M. Dubinskii, Opt. Mater. Express 2, 78 (2012).

13 J. E. Garay, Annu. Rev. Mater. Res. 40, 445–468 (2010).